Myocardial motion estimation from 2D analytical phases and preliminary study on the hypercomplex signal

Liang Wang

Numéro d'ordre :2014ISAL0140 Année 2014

THÈSE

Délivrée par

L'INSTITUT NATIONAL DE SCIENCES APPLIQUÉES DE LYON

DIPLÔME DE DOCTORAT

(arrêté du 7 aout 2006)

ÉCOLE DOCTORALE : ÉLECTRONIQUE, ÉLECTROTECHNIQUE, AUTOMATIQUE

Spécialité : Traitement du Signal et de l'Image

Soutenue publiquement le 19 Décembre 2014 par

Liang WANG

Myocardial motion estimation from 2D analytical phases and preliminary study on the hypercomplex signal

Jury

Philippe DELACHARTRE	Professeur des Universités, INSA Lyon	Directeur de thèse
Patrick R. GIRARD	Professeur agrégé, INSA Lyon	Co-encadrant de thèse
Patrick CLARYSSE	Directeur de Recherche, CNRS	Co-encadrant de thèse
Stephen J. SANGWINE	Senior Lecturer, Université d'Essex	Rapporteur
Laurent SARRY	Professeur des Universités, Université d'Auvergne	Rapporteur
Philippe CARRÉ	Professeur des Universités, Université de Poitiers	Examinateur
Mireille GARREAU	Professeur des Universités, Université de Rennes 1	Examinateur

SIGLE	ECOLE DOCTORALE	NOM ET COORDONNEES DU RESPONSABLE
CHIMIE	**CHIMIE DE LYON** **http://www.edchimie-lyon.fr** Sec : Renée EL MELHEM Bat Blaise Pascal 3e etage 04 72 43 80 46 Insa : R. GOURDON secretariat@edchimie-lyon.fr	M. Jean Marc LANCELIN Université de Lyon – Collège Doctoral Bât ESCPE 43 bd du 11 novembre 1918 69622 VILLEURBANNE Cedex Tél : 04.72.43 13 95 directeur@edchimie-lyon.fr
E.E.A.	**ELECTRONIQUE, ELECTROTECHNIQUE, AUTOMATIQUE** **http://edeea.ec-lyon.fr** Sec : M.C. HAVGOUDOUKIAN eea@ec-lyon.fr	M. Gérard SCORLETTI Ecole Centrale de Lyon 36 avenue Guy de Collongue 69134 ECULLY Tél : 04.72.18 60.97 Fax : 04 78 43 37 17 Gerard.scorletti@ec-lyon.fr
E2M2	**EVOLUTION, ECOSYSTEME, MICROBIOLOGIE, MODELISATION** **http://e2m2.universite-lyon.fr** Sec : Safia AIT CHALAL Bat Atrium- UCB Lyon 1 04.72.44.83.62 Insa : S. REVERCHON Safia.ait-chalal@univ-lyon1.fr	Mme Gudrun BORNETTE CNRS UMR 5023 LEHNA Université Claude Bernard Lyon 1 Bât Forel 43 bd du 11 novembre 1918 69622 VILLEURBANNE Cédex Tél : 06.07.53.89.13 e2m2@ univ-lyon1.fr
EDISS	**INTERDISCIPLINAIRE SCIENCES-SANTE** **http://www.ediss-lyon.fr** Sec : Safia AIT CHALAL Bat Atrium – UCB Lyon 1 04 72 44 83 62 Insa : Safia.ait-chalal@univ-lyon1.fr	Mme Emmanuelle CANET-SOULAS INSERM U1060, CarMeN lab, Univ. Lyon 1 Bâtiment IMBL 11 avenue Jean Capelle INSA de Lyon 696621 Villeurbanne Tél : 04.72.68.49.09 Fax :04 72 68 49 16 Emmanuelle.canet@univ-lyon1.fr
INFOMATHS	**INFORMATIQUE ET MATHEMATIQUES** **http://infomaths.univ-lyon1.fr** Sec :Renée EL MELHEM Bat Blaise Pascal 3e etage infomaths@univ-lyon1.fr	Mme Sylvie CALABRETTO LIRIS – INSA de Lyon Bat Blaise Pascal 7 avenue Jean Capelle 69622 VILLEURBANNE Cedex Tél : 04.72. 43. 80. 46 Fax 04 72 43 16 87 Sylvie.calabretto@insa-lyon.fr
Matériaux	**MATERIAUX DE LYON** **http://ed34.universite-lyon.fr** Sec : M. LABOUNE PM : 71.70 –Fax : 87.12 Bat. Saint Exupéry Ed.materiaux@insa-lyon.fr	M. Jean-Yves BUFFIERE INSA de Lyon MATEIS Bâtiment Saint Exupéry 7 avenue Jean Capelle 69621 VILLEURBANNE Cedex Tél : 04.72.43 71.70 Fax 04 72 43 85 28 Ed.materiaux@insa-lyon.fr
MEGA	**MECANIQUE, ENERGETIQUE, GENIE CIVIL, ACOUSTIQUE** http://edmega.universite-lyon.fr/ Sec : M. LABOUNE PM : 71.70 –Fax : 87.12 Bat. Saint Exupéry mega@insa-lyon.fr	M. Philippe BOISSE INSA de Lyon Laboratoire LAMCOS Bâtiment Jacquard 25 bis avenue Jean Capelle 69621 VILLEURBANNE Cedex Tél : 04.72 .43.71.70 Fax : 04 72 43 72 37 Philippe.boisse@insa-lyon.fr
ScSo	**ScSo*** **http://recherche.univ-lyon2.fr/scso/** Sec : Viviane POLSINELLI Brigitte DUBOIS Insa : J.Y. TOUSSAINT viviane.polsinelli@univ-lyon2.fr	Mme Isabelle VON BUELTZINGLOEWEN Université Lyon 2 86 rue Pasteur 69365 LYON Cedex 07 Tél : 04.78.77.23.86 Fax : 04.37.28.04.48 isavonb@gmail.com

*ScSo : Histoire, Géographie, Aménagement, Urbanisme, Archéologie, Science politique, Sociologie, Anthropologie

Acknowledgements

Firstly, I would like to sincerely gratitude to my supervisor Prof. Philippe Delachartre and my co-supervisors Prof. Patrick R. Girard and Prof. Patrick Clarysse for the support in all the stages throughout this three-year journey. Yours' broad scientific view and yours' seriousness to research always inspire me. Yours' patience and kindness help me pass through the three years. It is really a wonderful experience working with yours.

I would like to acknowledge Prof. Stephen J. Sangwine and Prof. Laurent Sarry for their effort to review this thesis manuscript. I am also grateful to Prof. Philippe Carré, Prof Mireille Garreau for their willingness to discuss the work during the thesis defence as the members of the jury.

Thank all my colleges in CREATIS, especially the colleges share the same office with me since three years Matthew Ozon and Zhengjun Liu, who help me a lot and encourage me from time to time. I cherish also the friendship with some students during the past three years: Fanglue, Xinxin, ZhaoYue, Hongying, Pei, Changyu, Shengfu, Peng, Yan, ZhangYue, Bin, Xinqin, Younes, Mohammad, Matthieu, Alfredo, Razmig, Claire, Maeva, Meriem.

Specially, I would like to thank my parents, Liucun Wang, Yuhua Zeng and my uncle Xin Zeng, for their inseparable support and unrequited love for all these years.

Abstract

There are requirements for the processing of 2D/3D medical data for several applications such as motion estimation on 2D cardiac image sequence and 2D/3D envelope detection for ultrasound radio-frequency signal. Meanwhile, different mathematical tools, such as multidimensional analytic signals, provide possibilities to calculate multidimensional phases and moduli. However, little work can be found on multidimensional analytic signals that perform appropriate extensibility for the applications on both of the 2D and 3D medical data processing. In this thesis, based on the Hahn 1D complex analytic, we aim to proposed a multidimensional extension approach from the 2D to a new 3D hypercomplex analytic signal in the framework of Clifford algebra. With the complex/hypercomplex analytic signals, we propose new 2D/3D medical image processing methods for the application of ultrasound envelope detection and cardiac motion estimation.

Firstly, a general representation of 2D quaternion signal is proposed in the framework of Clifford algebra and this idea is extended to generate 3D hypercomplex analytic signal. This 3D hypercomplex analytic signal is called 3D Clifford analytic signal. The proposed method describes that the complex/hypercomplex 2D analytic signals, together with 3D hypercomplex analytic signal, are equal to different combinations of the original signal and its partial and total Hilbert transforms, which means that the hypercomplex Clifford analytic signal can be calculated by the classical Fourier transform. Therefore, this method offers the numerical implementation with a low computational complexity. Based on the proposed 3D Clifford analytic signal, an application of 3D ultrasound envelope detection is presented. The results show a contrast optimization of about 7% comparing with 1D and 2D envelope detection methods.

Secondly, this thesis proposes an approach based on two spatial phases of the 2D analytic signal applied to cardiac sequences. By combining the information of these phases issued from analytic signals of two successive frames, we propose an analytical estimator for 2D local displacements. To improve the accuracy of the motion estimation, a local bilinear deformation model is used within an iterative estimation scheme. This phase-based method allows the displacement to be estimated with subpixel accuracy and is robust to image intensity variation in time. Results from seven realistic simulated tagged magnetic resonance imaging (MRI) sequences show that our method is more accurate compared with the state-of-the-art method using the phase of monogenic signal or the classical method using the optical flow equation. The motion estimation errors (end point error) of the proposed method are reduced by about 33% compared with that of the tested methods. In addition, the frame-to-frame displacements are further accumulated in time, to allow for the calculation of myocardial point trajectories. Indeed, from the estimated trajectories in time on two patients with infarcts, the shape of the trajectories of myocardial points belonging to pathological regions are clearly reduced in magnitude compared with the ones from normal regions. Myocardial point trajectories, estimated from our phase-based analytic signal approach, are therefore a good indicator of the local cardiac dynamics. Moreover, they are shown to be coherent with the estimated deformation of the myocardium.

Résumé

Il y a des demandes de traitement des données médicales 2D/3D pour plusieurs applications, comme l'estimation du mouvement sur des séquences d'images cardiaques 2D/3D ou la détection d'enveloppe 2D/3D du signal échographique radio fréquence. Les signaux analytiques multidimensionnels nous permettent d'avoir des possibilités de calculer les phases et modules. Cependant, peu de travaux se trouvent sur les signaux analytiques multidimensionnels qui effectuent une extensibilité appropriée pour les applications à la fois sur du traitement des données médicales 2D et 3D. Cette thèse a pour objectif de proposer des nouvelles méthodes pour le traitement des images médicales 2D/3D pour les applications de détection d'enveloppe et d'estimation du mouvement.

Premièrement, une représentation générale du signal quaternionique 2D est proposée dans le cadre de l'algèbre de Clifford et cette idée est étendue pour modéliser un signal analytique hypercomplexe 3D. La méthode proposée décrit que le signal analytique complexe 2D, est égal aux combinaisons du signal original et de ses transformées de Hilbert partielles et totale. Cette écriture est étendue au cas du signal analytique hypercomplexe 3D. Le résultat obtenu est que le signal analytique hypercomplexe de Clifford peut être calculé par la transformée de Fourier complexe classique. Basé sur ce signal analytique de Clifford 3D, une application de détection d'enveloppe en imagerie ultrasonore 3D est présentée. Les résultats montrent une amélioration du contraste de 7% par rapport aux méthodes de détection d'enveloppe 1D et 2D.

Deuxièmement, cette thèse propose une approche basée sur deux phases spatiales du signal analytique 2D appliqué aux séquences cardiaques. En combinant l'information de ces phases des signaux analytiques de deux images successives, nous proposons un estimateur analytique pour les déplacements locaux 2D. Pour améliorer la précision de l'estimation du mouvement, un modèle bilinéaire local de déformation est utilisé dans un algorithme itératif. Cette méthode basée sur la phase permet au déplacement d'être estimé avec une précision inférieure au pixel et est robuste à la variation d'intensité des images dans le temps. Les résultats de sept séquences simulées d'imagerie par résonance magnétique (IRM) marquées montrent que notre méthode est plus précise comparée à des méthodes récentes utilisant la phase du signal monogène ou des méthodes classiques basées sur l'équation du flot optique. Les erreurs d'estimation de mouvement de la méthode proposée sont réduites d'environ 33% par rapport aux méthodes testées. En outre, les déplacements entre deux images sont cumulés en temps, pour obtenir la trajectoire d'un point du myocarde. En effet, des trajectoires ont été calculées sur deux patients présentant des infarctus. Les amplitudes des trajectoires des points du myocarde appartenant aux régions pathologiques sont clairement réduites par rapport à celles des régions normales. Les trajectoires des points du myocarde, estimées par notre approche basée sur la phase de signal analytique, sont donc un bon indicateur de la dynamique cardiaque locale. D'ailleurs, elles s'avèrent cohérentes à la déformation estimée du myocarde.

Contents

List of symbols and abbreviations

Latin letter

x	Horizontal direction
y	Vertical direction
z	Depth direction
t	Time
u	Horizontal frequency
v	Vertical frequency
w	Time frequency
a_1, a_3, a_5, a_7	Amplitudes of Hahn single-quadrant/orthant analytical signal
i'	Imaginary unit of complex signal
i, j, k	Imaginary units of biquaternion or Clifford analytical signal
e_1, e_2, e_3	Generators of geometric algebra

Greek letter

$\psi_1, \psi_3, \psi_5, \psi_7$	Hahn single-quadrant/orthant analytical signals
$\phi_1, \phi_3, \phi_5, \phi_7$	Phases of Hahn single-quadrant/orthant analytical signal
ψ_q	Quaternion signal
$\phi_i, \phi_j, \phi_k,$	Phases of quaternion signal
ψ_{bq}	Biquaternion Clifford analytical signal
ψ_m	Monogenic signal
Φ	Orientation angle of monogenic signal
Θ	Phase of monogenic signal

Abbreviations

$1D$	One dimensional
nD	N dimensional
AS	Hahn single-quadrant/orthant analytical signal
MS	Monogenic signal
QS	Quaternion signal
CAS	Clifford analytical signal
QFT	Quaternion Fourier transform
$IQFT$	Inverse quaternion Fourier transform
MRI	Magnetic resonance imaging

I Résumé en français

I.1 Introduction

Motivation

Les maladies cardiovasculaires (MCV) représentent 30% de la mortalité mondiale totale. Elles sont les causes principales de décès dans de nombreux pays en développement. Chaque année depuis 1900, sauf 1918, les MCV ont représenté plus de décès que toutes les autres causes majeures de décès aux États-Unis. Sur la base de données des taux de décès de 2010, il y a un décès en moyenne toutes les 40 secondes par MCV. On estime que 83,6 millions des adultes américains ont plus d'un type de MCV. Parmi eux, 42,2 millions ont plus de 60 ans [Go *et al.* (2014)]. En général, les MCV sont la cause principale de décès chez les adultes.

Comme indiqué dans la référence [Go *et al.* (2014)], la maladie coronarienne (MC) a provoqué 1 décès sur 6 aux États-Unis en 2010. Cette année-là, 379559 Américains sont morts de MC. Chaque année, environ 620000 Américains ont une nouvelle attaque coronarienne et environ 295000 ont une crise récurrente. Il est estimé que 150000 infarctus du myocarde supplémentaires se produisent chaque année. Environ toutes les 34 secondes, un Américain a un événement coronarien, et environ toutes les 1 minute et 23 secondes, un Américain en meurt.

Une clé pour prévenir les MCV est de connaître les signes avant-coureurs d'une crise cardiaque. Les chercheurs ont trouvé certains indicateurs sur des études impliquant des milliers de patients. Ces indicateurs jouent un rôle important dans le risque de développement d'une maladie cardiaque. Le dépistage et le résultat de diagnostic d'anomalie du mouvement du myocarde, sont généralement considérés comme un élément important dans le diagnostic de la maladie coronarienne. Les anomalies de la dynamique cardiaque peuvent être identifiées en imagerie par résonance magnétique (IRM) et en échocardiographie. Quand il y a des variations sur l'intensité de séquence IRM au cours du temps, il est éventuellement difficile de traiter les images IRM.

L'objectif de la thèse

Il y a deux objectifs principaux dans cette thèse. Le premier consiste à proposer des signaux complexes/hypercomplexes et à définir l'amplitude et la phase locale. Il nous permet des possibilités d'extraire les caractéristiques et les paramètres physiques d'un

signal multidimensionnel. Par exemple, une phase représentée la structure d'une image 2D, et il donc n'influence pas par la variation sur l'intensité de l'image. Les signaux hypercomplexes sont modélisés dans le cadre mathématique des algèbres de Clifford pour permettre une extension aux dimensions supérieures 2D et 3D.

Le deuxième objectif est de proposer une méthode d'estimation du mouvement basée sur les phases locales des séquences dynamiques d'images cardiaques. La définition de la phase des signaux complexes/hypercomplexes doit être adaptée à l'estimation du mouvement du myocarde dans les séquences IRM marquées . Comme il existe plusieurs méthodes d'estimation du mouvement dans la littérature, la méthode proposée devrait permettre d'atteindre une précision sur le mouvement cardiaque estimé au moins égale à celle des méthodes existantes dans l'état de l'art.

Organisation de la thèse

Cette thèse est divisée en deux parties: l'analyse de l'état de l'art dans le chapitre 2 et les contributions dans les chapitres 3, 4, et 5.

Le chapitre 2 est l'étude de l'état de l'art. Une revue des signaux analytiques complexe/hypercomplexe est présentée en 2D et nD. Ensuite, des applications dans le domaine de l'estimation du mouvement utilisant l'information de phase du signal analytique sont présentées. Enfin, plusieurs travaux sur l'estimation du mouvement du myocarde sont présentés.

Le chapitre 3 traite de l'extension du signal 2D à 3D et de l'extension du signal complexe classique au signal hypercomplexe défini dans les algèbres de Clifford. Ainsi, le signal hypercomplexe 3D appelé signal analytique de Clifford 3D est défini dans ce chapitre. Plusieurs exemples introductifs sont présentés et une application du signal analytique de Clifford 3D à la détection d'aiguille de biopsie est donnée en fin de chapitre. Le chapitre 4 présente la méthode proposée pour l'estimation de mouvement du myocarde. Cette méthode est basée sur deux phases spatiales du signal analytique 2D qui sont appliquées à des séquences IRM cardiaques marquées. En combinant les informations de phase des signaux analytiques de deux images successives, nous proposons un estimateur analytique pour les déplacements 2D locaux. Pour augmenter la précision de l'estimation de mouvement, un modèle bilinéaire de déformation locale est utilisé dans une procédure d'estimation itérative. Les avantages principaux sont: (1) la méthode basée sur la phase nous permet d'estimer le déplacement avec une précision de inférieure au pixel et (2) cette méthode est robuste à la variation de l'intensité de l'image dans le temps, et le filtrage préliminaire (par exemple, lissage de l'image) n'est pas nécessaire grâce au modèle bilinéaire.

Le chapitre 5 donne les résultats de la méthode proposée dans le chapitre 4. Les résultats de l'estimation de mouvement à partir de sept séquences IRM marquées, montrent que cette méthode est plus précise en la comparant avec la méthode basée sur la phase de signal monogénique et la méthode classique basée sur le flot optique. Les déformations cardiaques sont calculées à partir des champs de déplacement estimés. Les déplacements

entre deux images successives sont cumulés dans le temps, afin de fournir la trajectoire de points matériels du myocarde. En effet, à partir des trajectoires estimées sur deux patients atteints d'un infarctus, les formes des trajectoires appartenant aux régions pathologiques sont réduites en amplitude par rapport aux trajectoires des points appartenant aux régions saines du myocarde. Les résultats obtenus sont cohérents avec les cartes de déformations estimées du myocarde. Par conséquent, les trajectoires du myocarde, estimées par notre approche, constituent un indicateur prometteur pour l'évaluation de la dynamique du myocarde.

I.2 État de l'art

Depuis deux décennies, plusieurs types de signaux complexes 2D ont été proposés par extension du signal analytique de Gabor. Notre objectif étant d'étudier les signaux hypercomplexes, ce chapitre réalise l'état de l'art dans ce domaine. Dans le cadre de notre travail sur l'estimation du mouvement cardiaque par le signal complexe, nous examinons tout d'abord différents algorithmes basés sur de la phase du signal complexe et hypercomplexe proposés pour estimer le mouvement dans des séquences d'images, puis nous étudions des travaux plus spécifiques portant sur l'estimation du mouvement du myocarde.

Signaux complexes et hypercomplexes 2D et nD

Les principaux signaux complexes 2D sont: le signal analytique complexe (AS), le signal quaternionique (QS), et le signal monogénique (MS). Cependant, l'un des outils de base pour calculer le signal complexe est la transformée de Hilbert. Les signaux complexes en 2D avec des spectres quadrants uniques ont été proposés par Hahn [Hahn (1992)]. On peut obtenir aussi le signal analytique complexe par transformation de Fourier 2D complexe en prenant l'information d'un seul quadrant de son spectre de fréquence. La transformation de Fourier quaternionique (QFT) a d'abord été introduite par Ernst [Ernst *et al.* (1987)] et Delsuc [Delsuc (1988)], puis par Ell [Ell (1993)], Bülow et Sommer [Bülow and Sommer (1997)]. Le signal quaternionique est calculé à partir du premier quadrant du spectre de la QFT. Les AS et QS peuvent être calculés à partir de la transformation de Hilbert. De plus, différents signaux quaternioniques seront obtenus à partir de différentes définitions de la QFT. Le signal monogénique est une autre formulation de l'extension en 2D du signal analytique 1D. Il a été développé par Felsberg [Felsberg and Sommer (2001), Felsberg (2002)] en fonction de la transformation de Riesz.

En 2011, Hahn and Snopek ont introduit que, selon le choix de l'algèbre des vecteurs de base $\{e_1, e_2, e_3, ..., e_n\}$, différentes définitions de la fonction d'analytique hypercomplexe peuvent être obtenue [Hahn and Snopek (2011)]. Ils ont proposé une théorie des signaux analytiques complexes et hypercomplexes nD. Pour la signal hypercomplexe, un signal analytique octonionique 3D est obtenu en appliquant l'algèbre de Cayley-Dickson. Dans le domaine fréquentiel, les signaux complexes/hypercomplexes sont définis par la transformation de Fourier inverse complexe/hypercomplexe sur un spectre d'orthant unique.

A partir des études de Grassmann, Hamilton et Clifford, l'algèbre de Clifford multi-

quaternionique est introduite dans [Girard *et al.* (2013)]. Le signal analytique nD est proposé dans le cadre de ces algèbres de multiquaternion. Girard et al. ont défini la transformée de Fourier Clifford nD. Dans cette définition, le signal d'entrée se repartant le côté gauche de tous les N fonctions exponentielles. Pour la dimension $2D + t$, une algèbre de Clifford 3D peut être utilisée, qui est constituée par un biquaternion de Clifford.

Méthodes d'estimation du mouvement basées sur la phase spatiale locale

Au cours des vingt dernières années, l'application des algèbres hypercomplexes aux signaux et aux images 2D a été bien développée. Trois principales raisons sont discutées par Alfsmann et al. pour l'application des signaux hypercomplexes [Alfsmann *et al.* (2007)]: (1) Les signaux exprimés par une fonction d'un ou plusieurs paramètres indépendants tels que le temps et la position. La dimension de l'algèbre a besoin d'être choisie pour correspondre à la dimension du signal. (2) On a besoin des signaux hypercomplexes dans plusieurs applications de traitement des signaux réels ou complexes, par exemple, le filtrage numérique. (3) On a besoin des signaux hypercomplexes pour le traitement parallèle des signaux indépendants.

Les travaux de Felsberg, Bülow et Sommer ont été largement appliqué au traitement du signal et de l'image, comme l'estimation du mouvement et le suivi [Krause and Sommer (2005), Lee and Park (2009)], la détection de mouvement [Traversoni (2006)] et la disparité entre les images [Bülow (1999)]. De plus, les méthodes concernant les quaternions ont également été appliqués pour la détection de bord dans des image couleur [Sangwine and Ell (2000)]. La plupart de ces travaux sont relatifs aux ondelettes et à l'estimation du mouvement.

Comme une technique alternative à la corrélation par intensité, des technique d'estimation de déplacement par la corrélation de phase spatiale ont été étudiés [Wang *et al.* (2004), Argyriou and Vlachos (2006), Chien and Aoki (2004), Bruni *et al.* (2007), Bruni *et al.* (2009), Kumar *et al.* (2011)]. En 2004, Wang et al. [Wang *et al.* (2004)] ont extrait une pseudo-phase à partir du signal analytique du motif de "speckle". Argyriou et Vlachos [Argyriou and Vlachos (2006)] ont proposé une méthode d'estimation de mouvement de haute précision sous-pixéllique en utilisant la corrélation de phase. Leur méthode repose sur la détection du maximum de la fonction de corrélation croisée entre deux trames consécutives f_t and f_{t+1} dans une vidéo animée. En 2004, Chien et Aoki [Chien and Aoki (2004)] ont présenté une méthode d'estimation de mouvement robuste par la corrélation de phase (POC), pour les séquences vidéo. Le vecteur de mouvement d'un point sur une image vidéo est changé de façon adaptative entre les résultats de mouvement obtenus par les deux méthodes d'estimation de mouvement: une méthode POC de balayage hiérarchique complètement et une méthode POC de balayage hiérarchique. En comparant les techniques de corrélation de phase classique qui ne peuvent être appliquées aux images à

niveaux de gris, Reddy et Talari [Reddy and Talari (2011)] ont proposé une extension de la technique de corrélation de phase pour le champ de quaternions en utilisant la transformée de Fourier quaternionique. Ils ont utilisé une corrélation croisée quaternionique de deux images $f(x, y)$ et $g(x, y)$ proposé premièrement par Sangwine et al. [Sangwine *et al.* (2001)].

En 2007, Zang et al. ont adapté la méthode du flux optique pour une estimation locale et globale combiné (CLG). Le principe est d'estimer le flux optique dense à partir du tenseur de courbure monogénique [Zang *et al.* (2007)]. En 2009, Demarcq et al. ont estimé le flux à partir d'une notion de phase de couleur locale, à partir du signal monogénique associé à une image couleur [Demarcq *et al.* (2009)]. Ces travaux sont basés sur l'approche CLG et le signal 2D. Demarcq et al. ont ensuite étendu leur travail à un signal 3D en utilisant l'approche CLG pour l'estimation du flux optique couleur [Demarcq *et al.* (2011)].

Méthodes d'estimation du mouvement du coeur

En 1999, Osman et al. [Osman *et al.* (1999)] introduit une méthode basée sur l'image de phase résultant du filtrage passe-bande d'une image en ne conservant qu'un quadrant de l'espace de Fourier. La méthode associée qui réalise l'estimation du champ de déplacement dans des séquences d'images par résonance magnétique marquées à partir de ce principe est connue sous le nom de HARP (Harmonic Phase imaging). Cette approche a été utilisée pour l'analyse rapide des séquences en imagerie par résonance magnétique de marquage tissulaire.

Un autre travail sur l'image de résonance magnétique (RM) cardiaque marquée a été réalisé par Arts et al. en 2010 pour l'estimation du déplacement avec une précision subpixellique [Arts *et al.* (2010)]. Dans cette méthode appelée SinMod, l'idée principale est que l'intensité de chaque pixel est modélisée par un front d'onde sinusoïdale. A partir de filtrages passe-bande biaisés dans les fréquences basses et hautes de deux images consécutives, il y a une relation locale avec le mouvement du tissu myocardique. Pour une séquence avec un bruit faible, les méthodes SinMod et HARP ont des performances similaires. Cependant, le procédé SinMod fournit un meilleur résultat dans le cas d'images bruitées, de présence de repliement de spectre et d'artefact dans le motif de grille. Xavier et al. en 2012 ont utilisé une méthode du flux optique basé sur la phase pour estimer le mouvement du myocarde dans des séquences ciné IRM [Xavier *et al.* (2012)]. Il s'agit d'une version modifiée de l'algorithme du flux optique basé sur l'information de phase (MPOF) en utilisant le filtrage spatial introduit par Bruno et Pellerin [Bruno and Pellerin (2002)]. Le MPOF consiste en un filtrage spatial complexe de Gabor 2D suivi par une dérivée temporelle d'ordre deux pour estimer le flux optique, au lieu d'utiliser des filtres complexe de Gabor 3D. Sur des images cardiaques en mode B échocardiographiques, une autre méthode basée sur le flux optique a été proposée par Sühling et al. [Sühling *et al.* (2005)]. Cette méthode analyse les images localement à l'aide d'un modèle de raffinement spatial

locale pour la vitesse et un modèle linéaire dans le temps, qui permettent de d'estimer le mouvement du coeur dans toute sa complexité (rotation, contraction/expansion et de cisaillement). Une même approche est adoptée par Alessandrini et al. [Alessandrini *et al.* (2013)], qui fonctionne bien à la fois sur des images échocardiographiques et des images de résonance magnétique cardiaque marquée. Dans cette méthode, la phase monogénique de Felsberg est utilisée, ce qui est une différence par rapport à la méthode de Sühling. Partant d'une hypothèse de conservation de la phase monogénique au cours du temps, le déplacement est calculé localement. Le modèle de translation pure de Felsberg est remplacé par un modèle de raffinement local du déplacement afin d'adapter ainsi le mouvement du myocarde. Une stratégie de sélection automatique de la taille des fenêtres dans l'image est également proposé, ce qui évite le problème du choix de la taille de la fenêtre d'image lors du calcul des paramètres régionaux de mouvement à l'intérieur de la fenêtre spatio-temporelle B-spline. L'évaluation a été réalisée sur les séquences IRM marquées de synthèse, générées par le logiciel ASSESS [Clarysse *et al.* (2011)], et a montré des résultats encore améliorés par rapport aux méthodes SinMod et de Zang (la méthode du tenseur de courbure monogénique) [Zang *et al.* (2007)].

Conclusion

Dans ce chapitre, deux parties ont été étudiées: (1) les signaux complexes et hypercomplexes en 1D et nD; (2) les méthodes d'estimation de mouvement dans des séquences d'images basées sur l'information de phase et plus spécifiquement celles dédiées à la quantification du mouvement du coeur. Par ailleurs, la plupart des applications sont basées sur le signal complexe/hypercomplexe 2D; peu de travaux qui montrent une extension possible sur le traitement des données 3D ou nD.

En conséquence, nous nous concentrons sur les problèmes suivants: (1) Quel type de signal analytique complexe/hypercomplexe présente une information de phase appropriée pour notre application et, plus important, quelle algèbre pourrait être choisie afin d'étendre le signal analytique complexe/hypercomplexe en dimension plus élevée et en même temps, l'algèbre choisie contient le potentiel d'application de traitement de données nD? (2) Est-il possible d'obtenir une estimation d'estimation de mouvement du myocarde plus précis avec une nouvelle méthode de phase que la méthode SinMod et la méthode de phase monogénique de Alessandrini et al.?

Pour le premier problème, nous partons de l'idée Hahn, qui utilise la AS 2D de quadrant-unique pour construire le signal hypercomplexe QS 2D. A partir de cette idée, on pourrait utiliser le signal complexe 3D (Hahn AS 3D) pour construire un signal analytique hypercomplexe 3D dans le cadre de l'algèbre de Clifford. Ce travail est présenté dans le chapitre 3. A partir de Hahn AS 3D, une nouvelle définition du signal analytique hypercomplexe est donnée dans le cadre de l'algèbre de Clifford 3D. Pour le deuxième problème, nous avons proposé une nouvelle méthode d'analyse du mouvement du myocarde basée sur la phase du Hahn AS 2D. Nous montrons que la phase de Hahn AS 2D

est bien adaptée pour une quantification précise de mouvement précis pour des séquences d'IRM cardiaques marquées. Les détails de la méthode et les résultats d'expérience sont présentés, respectivement, au chapitre 4 et au chapitre 5.

I.3 Signaux analytiques de Clifford 2D et 3D

De nouvelles structures algébriques ont été développées au cours des dernières décennies [Vince (2008)]. Un grand nombre de nouveaux signaux analytiques complexes a également été défini [Sangwine and Le Bihan (2007), Hahn and Snopek (2011), Unser *et al.* (2009), Said *et al.* (2008)] en se basant sur les algèbres de Clifford et les algèbres de Hamilton. L'une des applications les plus importantes du signal analytique (AS) est l'extraction des caractéristiques locales dans les images. Une des propriétés marquantes du signal analytique est la séparation de différents types d'informations, c'est-à-dire qu'un signal donné peut être séparé en phase locale et amplitude locale. De plus, les informations relatives aux angles partiels et aux modules partiels du signal hypercomplexe sont introduites dans [Bayro-Corrochano (2006)]. Dans le domaine médical, les données issues de l'échographie sont souvent sous la forme de volumes spatiales 3D ou volumes spatio-temporelles 4D (3D volumes variant dans le temps). Dans le cas tridimensionnel, la plupart des études antérieures opte pour une séparation des données volumiques en signaux 1D où 2D [Wachinger *et al.* (2011)]. Ces méthodes souffrent d'une perte d'information en raison du traitement séparé sur les dimensions. Par conséquent, un traitement de donnée multidimensionnelle sur la totalité du volume est nécessaire afin d'obtenir des résultats plus précis.

Dans ce chapitre, nous proposons une définition du signal analytique hypercomplexe 3D dans le cadre d'algèbre de Clifford comme une extension du signal de quaternion 2D (QS). Nous présentons un résultat de détection d'enveloppe sur des signaux Radio Fréquence (RF) issus de volumes échographiques, en utilisant le nouveau signal analytique 3D. Compte tenu de la conception de la transformation de Hilbert, nous présentons tout d'abord l'AS 1D classique. Ensuite, nous illustrons le fait que les éléments de QS 2D sont également construits à partir de transformation de Hilbert 2D. Ensuite, nous proposons le signal analytique 3D Clifford (CAS) sous sa forme biquaternionique, ainsi que le calcul du CAS 3D par des transformées de Hilbert. Enfin, une application de la CAS 3D pour la détection d'enveloppe en échographie est introduite.

Signaux analytiques 1D et 2D

En se basant sur la transformée de Hilbert, Gabor a défini en premier le signal analytique d'un signal réel 1D [Gabor (1946)]. Un AS $\psi(t)$ d'un signal réel $f(t)$ contient deux parties: une partie réelle (le signal réel lui-même) et une partie imaginaire (transformée de Hilbert de $f(t)$). Pour le cas 2D, nous appelons signaux de Hahn (Hahn AS 2D), les signaux complexes avec des spectres à quadrant-unique. D'une part, on peut obtenir le 2D AS Hahn par la transformation de Fourier 2D complexe en laissant un seul quadrant de son spectre en fréquence. Un autre procédé pour obtenir directement le Hahn AS 2D consiste à utiliser la transformée de Hilbert du signal d'origine. D'autre part, il est important que la transformée de Hilbert 2D partielle et totale du signal d'origine puisse être utilisé pour présenter la relation entre l'AS Hahn 2D et 2D QS. Pour un signal réel 2D $f(x,y)$, la Hahn AS 2D est:

$$\begin{aligned} \psi_1(x,y) &= (f - H\{f\}) + i'\left(H_x\{f\} + H_y\{f\}\right) \\ &= a_1 e^{i'\varphi_1} = a_1\cos\varphi_1 + i' a_1 \sin\varphi_1, \qquad (1) \\ \psi_3(x,y) &= (f + H\{f\}) + i'\left(H_x\{f\} - H_y\{f\}\right) \\ &= a_3 e^{i'\varphi_3} = a_3\cos\varphi_3 + i' a_3 \sin\varphi_3, \qquad (2) \end{aligned}$$

i' est l'imaginaire complexe habituel, $H\{f\}$ est la transformée de Hilbert totale. $H_x\{f\}$ et $H_y\{f\}$ sont, respectivement, les transformées de Hilbert partielles calculées en x et en y. a_1 et φ_1 sont, respectivement, le module et la phase de $\psi_1(x,y)$. a_3 et φ_3 sont, respectivement, le module et la phase de $\psi_3(x,y)$. Ces Hahn AS 2D sont calculées à partir de deux quadrants différents du spectre de Fourier de $f(x,y)$. A partir du Hahn AS 2D, nous voulons trouver la relation entre le module/phase et la transformée de Hilbert du signal pour une étude plus approfondie. A partir des équations ci-dessus, on obtient les solutions suivantes:

$$f(x,y) = \frac{1}{2}\left(a_1\cos\varphi_1 + a_3\cos\varphi_3\right), \qquad (3)$$

$$H\{f(x,y)\} = \frac{1}{2}\left(-a_1\cos\varphi_1 + a_3\cos\varphi_3\right), \qquad (4)$$

$$H_x\{f(x,y)\} = \frac{1}{2}\left(a_1\sin\varphi_1 + a_3\sin\varphi_3\right), \qquad (5)$$

$$H_y\{f(x,y)\} = \frac{1}{2}\left(a_1\sin\varphi_1 - a_3\sin\varphi_3\right). \qquad (6)$$

Ces solutions signifient que lorsque nous avons deux Hahn AS 2D d'un signal réel 2D, nous sommes en mesure de récupérer le signal original 2D et aussi sa transformée de Hilbert totale et partielle en utilisant la phase et le module de Hahn AS 2D.

Pour le 2D QS, plusieurs travaux ont été présentés précédemment. Ici nous passons en revue le calcul 2D QS en fonction de la transformée de Hilbert partielle et totale en 2D. Le but de cette revue est d'étendre cette approche au cas 3D qui sera présenté dans

la section suivante. Pour un signal réel 2D $f(x,y)$, le 2D QS $\psi_q(x,y)$ peut s'écrire [Bülow and Sommer (1997)]:

$$\psi_q(x,y) = f + iH_x\{f\} + jH_y\{f\} + kH\{f\}. \tag{7}$$

Puis, en écrivant $\psi_q(x,y)$ en fonction de la phase et l'amplitude de Hahn AS 2D, on obtient:

$$\begin{aligned}\psi_q &= \frac{1}{2}(a_1\cos\varphi_1 + a_3\cos\varphi_3) + i\left(\frac{1}{2}(a_1\sin\varphi_1 + a_3\sin\varphi_3)\right) \\ &\quad + j\left(\frac{1}{2}(a_1\sin\varphi_1 - a_3\sin\varphi_3)\right) + k\left(\frac{1}{2}(-a_1\cos\varphi_1 + a_3\cos\varphi_3)\right) \\ &= \frac{1}{2}[a_1\cos\varphi_1 + a_3\cos\varphi_3, a_1\sin\varphi_1 + a_3\sin\varphi_3, a_1\sin\varphi_1 - a_3\sin\varphi_3, -a_1\cos\varphi_1 + a_3\cos\varphi_3].\end{aligned} \tag{8}$$

Ce résultat montre que l'on peut obtenir QS à partir de Hahn AS. En outre, on a la propriété:

$$\psi_q(\psi_q)_c = \left[\frac{1}{2}\left(a_1^2 + a_3^2\right), 0, 0, 0\right], \tag{9}$$

avec $(\psi_q)_c$ la conjugaison de ψ_q:

$$(\psi_q)_c = f - iH_x\{f\} - jH_y\{f\} - kH\{f\} = [f, -H_x\{f\}, -H_y\{f\}, -H\{f\}]. \tag{10}$$

Signal analytique orthant-unique 3D

En 2011, la théorie des signaux complexes 2D a été étendue à n dimensions par Hahn et Snopek [Hahn and Snopek (2011)]. Pour le cas 3D, nous avons les signaux analytiques complexes en 3D avec des spectres orthant-uniques qui pourraient être obtenus par le transformée de Fourier complexe nD. Ici, nous donnons à ce signal l'abréviation Hahn AS 3D. Il semble donc naturel, de commencer par une présentation de la transformée de Fourier complexe 3D. On présente que toutes les Hahn AS 3D peuvent être représentés en fonction des transformées de Hilbert 3D total et partielle. Ensuite, les signaux correspondants aux huit orthants issus du spectre sont calculés et représentés par les transformées de Hilbert du signal d'origine. Les résultats de cette section nous seront utiles pour la définition de notre signal analytique de Clifford 3D.

La transformée de Fourier complexe 3D d'un signal réel $f(x,y,z)$ est donnée par:

$$F(u,v,w) = \int f(x,y,z)e^{-i'2\pi(ux+vy+wz)}dxdydz, \tag{11}$$

i' est l'imaginaire complexe d'habitude et les facteurs d'echelles sont omis. La transformée

de Fourier inverse est:

$$f(x,y,z) = \int F(u,v,w) e^{i' 2\pi (ux+vy+wz)} du dv dw. \tag{12}$$

La symétrie Hermitienne, qui est une propriété de la transformée de Fourier est appliquée pour calculer le AS 3D orthant-unique. Comme le montre la Fig. 3.10, l'espace des fréquences 3D dispose de huit (2^3) orthants. La symétrie hermitienne de la transformée de Fourier assure que le signal d'entrée peut être récupéré à partir de l'un des demi-plans du spectre, le signal réel 3D peut être représenté par quatre ($2^3/2$) des signaux analytiques. Dans ce qui suit, pour calculer les quatre signaux analytiques orthant-uniques sans perte de généralité, nous travaillons sur les spectres de l'espace engendré dans $u > 0$, qui sont les orthants avec les étiquettes I, III, V et VII dans la Fig. 3.10. Les signaux Hahn AS 3D sont calculés comme suit:

$$\begin{aligned}
\psi_1(x,y,z) =& (f - H_{xy}\{f\} - H_{xz}\{f\} - H_{yz}\{f\}) \\
&+ i' \left(H_x\{f\} + H_y\{f\} + H_z\{f\} - H\{f\}\right) \\
=& a_1 e^{i'\varphi_1} = a_1 \cos\varphi_1 + i' a_1 \sin\varphi_1, \qquad (13) \\
\psi_3(x,y,z) =& (f + H_{xy}\{f\} - H_{xz}\{f\} + H_{yz}\{f\}) \\
&+ i' \left(H_x\{f\} - H_y\{f\} + H_z\{f\} + H\{f\}\right) \\
=& a_3 e^{i'\varphi_3} = a_3 \cos\varphi_3 + i' a_3 \sin\varphi_3, \qquad (14) \\
\psi_5(x,y,z) =& (f - H_{xy}\{f\} + H_{xz}\{f\} + H_{yz}\{f\}) \\
&+ i' \left(H_x\{f\} + H_y\{f\} - H_z\{f\} + H\{f\}\right) \\
=& a_5 e^{i'\varphi_5} = a_5 \cos\varphi_5 + i' a_5 \sin\varphi_5, \qquad (15) \\
\psi_7(x,y,z) =& (f + H_{xy}\{f\} + H_{xz}\{f\} - H_{yz}\{f\}) \\
&+ i' \left(H_x\{f\} - H_y\{f\} - H_z\{f\} - H\{f\}\right) \\
=& a_7 e^{i'\varphi_7} = a_7 \cos\varphi_7 + i' a_7 \sin\varphi_7, \qquad (16)
\end{aligned}$$

où a_n et φ_n sont, respectivement, le module et la phase de la forme polaire de ψ_n, $n = 1, 3, 5, 7$. Les solutions de ces équations sont données par:

$$\begin{aligned}
f &= \tfrac{1}{4}\left(a_1\cos\varphi_1 + a_3\cos\varphi_3 + a_5\cos\varphi_5 + a_7\cos\varphi_7\right), && (17)\\
H_{yz}\{f\} &= \tfrac{1}{4}\left(-a_1\cos\varphi_1 + a_3\cos\varphi_3 + a_5\cos\varphi_5 - a_7\cos\varphi_7\right), && (18)\\
-H_{xz}\{f\} &= \tfrac{1}{4}\left(a_1\cos\varphi_1 + a_3\cos\varphi_3 - a_5\cos\varphi_5 - a_7\cos\varphi_7\right), && (19)\\
H_{xy}\{f\} &= \tfrac{1}{4}\left(-a_1\cos\varphi_1 + a_3\cos\varphi_3 - a_5\cos\varphi_5 + a_7\cos\varphi_7\right), && (20)\\
-H\{f\} &= \tfrac{1}{4}\left(a_1\sin\varphi_1 - a_3\sin\varphi_3 - a_5\sin\varphi_5 + a_7\sin\varphi_7\right), && (21)\\
H_x\{f\} &= \tfrac{1}{4}\left(a_1\sin\varphi_1 + a_3\sin\varphi_3 + a_5\sin\varphi_5 + a_7\sin\varphi_7\right), && (22)\\
H_y\{f\} &= \tfrac{1}{4}\left(a_1\sin\varphi_1 - a_3\sin\varphi_3 + a_5\sin\varphi_5 - a_7\sin\varphi_7\right), && (23)\\
H_z\{f\} &= \tfrac{1}{4}\left(a_1\sin\varphi_1 + a_3\sin\varphi_3 - a_5\sin\varphi_5 - a_7\sin\varphi_7\right). && (24)
\end{aligned}$$

A partir de ces huit équations, on obtient une conclusion similaire à celle obtenue dans le cas 2D: On peut récupérer un signal 3D ainsi que ses transformations de Hilbert 3D totales et partielles à partir des phases et des modules de son Hahn AS 3D. De plus, pour le cas 3D, quatre Hahn AS 3D sont nécessaires, ce qui devrait correspondre à la moitié du spectre du signal. Ce résultat servira pour la définition du signal analytique Clifford 3D dans ce qui suit.

Signal analytique de Clifford 3D

Afin d'étendre la notion de 2D QS au cas 3D dans l'algèbre de Clifford, nous considérons les biquaternions de Clifford, qui ont trois générateurs: e_1, e_2, e_3. L'algèbre complète contient huit éléments:

$$\begin{bmatrix} 1 & i = e_2e_3 & j = e_3e_1 & k = e_1e_2 \\ \epsilon = i'I = -e_1e_2e_3 & \epsilon i = e_1 & \epsilon j = e_2 & \epsilon k = e_3 \end{bmatrix}. \tag{25}$$

avec $\epsilon^2 = -1, e_1^2 = e_2^2 = e_3^2 = -1$, i' représentant l'imaginaire complexe d'habitude ($i'^2 = -1$) et où le produit de tenseur $I = 1 \otimes i$ ($I^2 = -1$) commute avec $i = i \otimes 1, j = j \otimes 1, k = k \otimes 1$. Pour une signal réel 3D $f(x, y, z)$, le signal analytique 3D Clifford (CAS) peut être définie comme:

$$\psi_{bq}(x, y, z) = f(x, y, z) \star\star\star \left\{ \left[\delta(x) + \frac{e_1}{\pi x} \right] \left[\delta(y) + \frac{e_2}{\pi y} \right] \left[\delta(z) + \frac{e_3}{\pi z} \right] \right\}. \tag{26}$$

où e_1, e_2, e_3 sont les unités imaginaires, $\star\star\star$ sont la convolution 3D. Le développement mathématique de $\psi_{bq}(x, y, z)$ est présenté par la somme du signal original, la transformée de Hilbert (partie pseudo scalaire), et sept transformées de Hilbert partielle (parties imaginaires). Tous les huit éléments constituent un biquaternion:

$$\psi_{bq}(x, y, z) = \begin{bmatrix} f & iH_{yz}\{f\} & j(-H_{xz}\{f\}) & kH_{xy}\{f\} \\ \epsilon(-H\{f\}) & \epsilon iH_x\{f\} & \epsilon jH_y\{f\} & \epsilon kH_z\{f\} \end{bmatrix}, \tag{27}$$

où $H\{f\}$ est le transformée de Hilbert total 3D de $f(x, y, z)$ et $H_x\{f\}$, $H_y\{f\}$, $H_z\{f\}$, $H_{xy}\{f\}$, $H_{xz}\{f\}$, $H_{yz}\{f\}$ sont les transformées de Hilbert partielles de $f(x, y, z)$. Nous avons constaté que tous les éléments à la fois de l'AS 3D et 3D Hahn CAS peuvent être représentés par la transformée de Hilbert totale et partielle du signal réel initial. Par conséquent, lorsque le remplaçant CAS 3D de ψ_{bq} par le Hahn AS 3D, on obtient le CAS

3D qui est représenté comme suit:

$$\psi_{bq} = \frac{1}{4}\begin{bmatrix} (a_1\cos\varphi_1 + a_3\cos\varphi_3 + a_5\cos\varphi_5 + a_7\cos\varphi_7), \\ i\,(-a_1\cos\varphi_1 + a_3\cos\varphi_3 + a_5\cos\varphi_5 - a_7\cos\varphi_7), \\ j\,(a_1\cos\varphi_1 + a_3\cos\varphi_3 - a_5\cos\varphi_5 - a_7\cos\varphi_7), \\ k\,(a_1\sin\varphi_1 - a_3\sin\varphi_3 - a_5\sin\varphi_5 + a_7\sin\varphi_7), \\ \epsilon\,(-a_1\cos\varphi_1 + a_3\cos\varphi_3 - a_5\cos\varphi_5 + a_7\cos\varphi_7), \\ \epsilon i\,(a_1\sin\varphi_1 + a_3\sin\varphi_3 + a_5\sin\varphi_5 + a_7\sin\varphi_7), \\ \epsilon j\,(a_1\sin\varphi_1 - a_3\sin\varphi_3 + a_5\sin\varphi_5 - a_7\sin\varphi_7), \\ \epsilon k\,(a_1\sin\varphi_1 + a_3\sin\varphi_3 - a_5\sin\varphi_5 - a_7\sin\varphi_7) \end{bmatrix}. \tag{28}$$

En utilisant le produit des biquaternion dans Eq. (2.51) et le conjugué des biquaternion dans Eq. (2.52), on obtient la propriété:

$$\psi_{bq}(\psi_{bq})_c = \begin{bmatrix} \frac{1}{4}\left(a_1^2 + a_3^2 + a_5^2 + a_7^2\right), \\ i(0), \\ j(0), \\ k(0), \\ \epsilon\left(\frac{1}{2}\left[a_1a_3\sin\left(\varphi_1 - \varphi_3\right) - a_5a_7\sin\left(\varphi_5 - \varphi_7\right)\right]\right), \\ \epsilon i(0), \\ \epsilon j(0), \\ \epsilon k(0), \end{bmatrix}. \tag{29}$$

Ensuite, le module de ψ_{bq} pourrait être défini comme $|\psi_{bq}|$ comme ci-dessous:

$$|\psi_{bq}| = \left\{\left[\frac{1}{4}\left(a_1^2 + a_3^2 + a_5^2 + a_7^2\right)\right]^2 + \left[\frac{1}{2}\left[a_1a_3\sin\left(\varphi_1 - \varphi_3\right) - a_5a_7\sin\left(\varphi_5 - \varphi_7\right)\right]\right]^2\right\}^{1/4}, \tag{30}$$

qui peuvent être utilisés pour calculer le module d'un signal 3D pour des applications.

Application à la détection d'enveloppe 3D par signal analytique de Clifford 3D

Les images ultrasonores radio fréquence (RF) et mode B constituent deux sortes d'images différentes. Il y a plusieurs étapes pour convertir le RF en mode B [Hedrick *et al.* (2004)], comme la démodulation, l'amplification d'intensité non-linéaire et le filtrage, etc. L'une de ces étapes importantes est la démodulation, et elle peut être réalisée par la détection d'enveloppe dans le traitement par ultrasons. Par conséquent, à partir du

signal d'analyse de l'échographie RF, l'amplitude du signal analytique peut être calculée et elle est utilisée en tant que l'enveloppe du signal RF. Habituellement, on calcule le signal analytique de lignes de balayage 1D séparément du signal RF [Schlaikjer *et al.* (2003)] par le module de Hahn AS 1D, puis l'amplitude de ce signal analytique 1D est obtenu à partir de son amplitude locale. En comparant avec le traitement 1D des lignes de balayage séparée, nous calculons le volume de l'échographie RF. Le CAS 3D RF échographie volumique est construit, puis le module $|\psi_{bq}(x, y, z)|$ du CAS 3D est utilisé comme une enveloppe du volume de l'échographie. L'expérience est réalisée à partir de la plate-forme d'imagerie par ultrasons du laboratoire CREATIS.

Une aiguille de biopsie est insérée dans un fantôme d'agar pour l'échographie. La profondeur d'acquisition sur ce fantôme est de 50 millimètres, la largeur est de 88 millimètres et le champ de vision est de 45,6 degrés pour 33 tranches. Nous comparons les résultats de la détection de l'enveloppe de CAS 3D avec celui de Hahn AS 1D et de QS 2D comme indiqué dans la Fig. 3.20. Le profil de l'aiguille de biopsie sur l'image de l'enveloppe de CAS 3D montre que la structure de l'aiguille de biopsie est plus visible. Les résultats de l'enveloppe présentent une optimisation du contraste de 8% et 6% en comparant, respectivement, avec des méthodes de détection d'enveloppe 1D et 2D.

Conclusion

Dans ce chapitre, nous avons présenté que les Hahn AS 2D et QS 2D peut être représenté par la transformée de Hilbert totale et partielle du signal réel. Par conséquent, nous avons constaté que la transformée de Fourier classique seulement est nécessaire pour obtenir le QS 2D sans transformation quaternionique de Fourier. Nous avons ensuite proposé le CAS 3D, qui est une extension du QS 2D dans le cadre des algèbres de Clifford. Nous avons introduit la relation entre le CAS 3D et quatre Hahn AS 3D orthant-uniques, et établi une relation directe entre eux. Enfin, une application est réalisée sur le module de CAS 3D, qui est appliquée à la détection d'enveloppe 3D d'un volume à ultrasons RF. Les résultats montrent que l'application du CAS 3D présente des avantages pour traiter le volume échographie RF.

I.4 Estimation du mouvement cardiaque dans des séquences d'IRM marquée utilisant la phase du signal analytique, un modèle bilinéaire et la compensation du mouvement

Introduction

Les propriétés mécaniques du coeur pathologique peuvent être évaluées par le mouvement et la déformation à partir des images cardiaques. Parmi les modalités d'images médicales, l'échographie et l'imagerie par résonance magnétique (IRM) sont les plus couramment utilisées pour l'estimation du mouvement cardiaque. Dans la technique de Résonance Magnétique (RM) par marquage tissulaire, l'image du tissu cardiaque est tatouée avec une grille magnétiquement saturée. La déformation de cette grille suit la déformation du myocarde pendant le cycle cardiaque. Jusqu'à présent, plusieurs méthodes ont été proposées pour estimer le mouvement à partir de séquences d'IRM marquées [Axel and Dougherty (1989)]. Ces méthodes sont basées sur l'extraction semi-automatique des motifs du marquage [Guttman *et al.* (1994), O'Dell *et al.* (1995)] ou sur les méthodes de flux optique [Prince and McVeigh (1992)]. La phase spatiale a été proposée comme une mesure moins sensible aux variations d'intensité de l'image dues par exemple à la perte de magnétisation du marquage au cours du cycle cardiaque. Osman et al. ont présenté une approche basée sur la phase harmonique (HARP), qui repose sur un filtrage passe-bande des images IRM de marquage dans le domaine de Fourier [Osman *et al.* (1999), Dallal *et al.* (2012)]. Dans l'approche SinMod présentée dans [Arts *et al.* (2010)], la distribution d'intensité au voisinage de chaque pixel est modélisée comme la somme de fronts d'onde harmoniques, obtenus par un filtre passe-bande 2D. La méthode est rapide et a montré une meilleure robustesse au bruit que la méthode HARP [Arts *et al.* (2010)]. Plus récem-

ment, une nouvelle méthode a été développée basée sur la conservation temporelle de la phase monogénique [Alessandrini *et al.* (2013)]. Dans ce travail, un schéma de B-spline "coarse-to-fine" est utilisé pour un calcul efficace et aussi un schéma de raffinement pyramidal aide à traiter de grands mouvements. A partir du champ de mouvement extrait des images du myocarde, de nouvelles études ont été réalisées pour obtenir des informations complémentaires comme, les contours du myocarde par segmentation [Dietenbeck *et al.* (2014)], la déformation locale [Kar *et al.* (2014), Oubel *et al.* (2012)] et le suivi local de la région myocardique [Arif *et al.* (2014), Luo *et al.* (2014), Sun *et al.* (2011)]. Pour toutes ces méthodes d'extraction de l'information, le point clé est d'évaluer précisément le champ de mouvement du myocarde.

Dans ce chapitre, nous nous concentrons sur une méthode précise d'estimation du mouvement à partir de séquences d'IRM de marquage du myocarde. La contribution principale de ce travail est de proposer une méthode d'estimation de mouvement 2D basée sur la phase locale des images. Les spécificités de l'approche proposée sont les suivantes: les vecteurs de mouvement estimés sont contrôlés localement par une transformation bilinéaire; le champ de mouvement entre deux images successives est raffiné itérativement; le modèle non-rigide de mouvement local et le modèle de compensation du mouvement global fournissent une estimation de champ de mouvement plus précise que les méthodes mentionnées précédemment (HARP, SinMod, Phase monogène).

La méthode proposée estime le déplacement entre deux images. Les images de phases locales sont calculées à partir des signaux analytiques des images IRM marquées. Pour décrire cette méthode, nous introduisons tout d'abord, la procédure d'extraction de l'espace des phases. Ensuite, nous décrivons le développement mathématique de l'estimateur analytique du déplacement appliqué aux images de phase. Puis, nous montrons que la complexité du mouvement local cardiaque peut être prise en compte par un modèle bilinéaire du déplacement. Finalement, une méthode itérative de raffinement est présentée pour atteindre un déplacement de précision inférieure au pixel.

Algorithme d'estimation du mouvement

L'extension multidimensionnelle du signal analytique 1D peut être trouvée dans le travail sur: le signal analytique 2D de Hahn [Hahn (1992)], le signal analytique quaternionique de Bülow et Sommer [Bülow and Sommer (2001)], ainsi que le signal monogénique de Felsberg et Sommer [Felsberg and Sommer (2001)]. Les signaux analytiques multidimensionnels ont des formes différentes mais sont tous basés sur des extensions directes de la transformée de Hilbert 1D, 2D ou nD. La méthode basée sur la phase a été proposée par Basarab et al. [Basarab *et al.* (2009)] pour l'application à l'estimation des déplacements sous-pixélliques dans les images échographiques. Les signaux analytiques 1D et 2D ont été introduits dans les chapitres 2 et 3.

Pour un signal réel 2D $f(x, y)$ de coordonnées cartésiennes (x, y), les transformées de Hilbert totale et partielles peuvent être calculées et combinées pour former le signal

quaternionique 2D et le signal analytique 2D. Le signal analytique 2D est donné en fonction de la transformée de Hilbert totale et partielle de $f(x, y)$ par [Hahn (1992)]. Pour notre problème d'estimation du mouvement 2D, nous avons deux variables locales inconnues à estimer, qui sont les déplacement et vitesse dans les directions horizontale et verticale. Puisque l'on sait que la phase est moins sensible aux changements de l'intensité globale de l'image et afin de résoudre le problème d'estimation du mouvement en 2D, les informations portées par deux phases appropriées devrait être choisie à partir des phases du signal quaternionique de l'équation Eq. (4.6) ou des phases du signal analytique de les équations Eqs. (4.7)–(4.10). En raison de la symétrie du spectre 2D de la transformée de Fourier 2D, ψ_1 et ψ_2 (ou ψ_3 et ψ_4) contiennent toutes les informations de l'image originale. De plus, ces deux phases spatiales contiennent des informations complémentaires sur la structure de l'image. Par exemple, sur l'image RM marquée de la Fig. 4.1, les lignes de marquage selon deux directions constituent deux informations structurelles complémentaires.

Bien qu'il existe une relation linéaire entre les phases du signal quaternionique ϕ_i, ϕ_j et les phases du signal analytique $\phi_1, \phi_2, \phi_3, \phi_4$, [Hahn and Snopek (2004), Hahn and Snopek (2011)], les phases de QS ne divisent pas les informations dans les deux directions de ligne de marquage (la phase du signal quaternionique ϕ_k est présenté par le module d'AS). Cela rend le signal quaternionique moins adapté au calcul du gradient spatial de la phase nécessaire à l'étape suivante de notre méthode. Par conséquent, nous utilisons ϕ_1, ϕ_2 de ψ_1, ψ_2 dans Eq. (4.7) et Eq. (4.8) comme images de base pour l'estimation du déplacement du myocarde dans notre méthode.

L'équation du flux optique est largement utilisée pour l'estimation du mouvement dans différents domaines d'application. Elle est basée sur les hypothèses de conservation de l'intensité des pixels dans le temps, et de petits déplacements entre des images consécutives (typiquement inférieure au pixel). Dans cette section, nous proposons de remplacer l'hypothèse d'invariance d'intensité dans le temps par celle de la phase. Ainsi, l'équation Eq. (4.11) est remplacée ci-après par deux équations prenant en compte les deux phases ϕ_1, ϕ_2 de AS ψ_1 et ψ_2:

$$d_x \frac{\partial \phi_1}{\partial x} + d_y \frac{\partial \phi_1}{\partial y} + \frac{\partial \phi_1}{\partial t} = 0,$$

$$d_x \frac{\partial \phi_2}{\partial x} + d_y \frac{\partial \phi_2}{\partial y} + \frac{\partial \phi_2}{\partial t} = 0.$$

Par conséquent, d_x, d_y peuvent être obtenus en résolvant le système de deux équations à deux inconnues. Afin d'éviter les problèmes de sauts de phase et les erreurs possibles de déroulement de phase, nous proposons de calculer les dérivées temporelles des phases directement à partir de chaque signal analytique et de son conjugué :

$$\frac{\partial \phi_1}{\partial t} = Arg[\psi_1^*(x, y, t) \cdot \psi_1(x, y, t + 1)],$$

$$\frac{\partial \phi_2}{\partial t} = Arg[\psi_2^*(x,y,t) \cdot \psi_2(x,y,t+1)],$$

avec ψ_1^* le conjugué de ψ_1 et ψ_2^* le conjugué de ψ_2. Dans ce qui suit, les phases sont calculées localement par les équations Eqs. (4.7) et (4.8) pour chaque bloc extrait des images RM de marquage.

Étant donné que le myocarde a un mouvement relativement complexe, le déplacement local du myocarde ne peut pas être estimé avec précision par un modèle simple de translation rigide. Par conséquent, un modèle de mouvement plus complexe est nécessaire pour approcher au mieux le déplacement local. Dans notre méthode, nous avons utilisé un modèle bilinéaire exprimant la translation, la dilatation, la rotation, et le cisaillement. Un tel modèle a déjà été utilisé pour l'estimation du déplacement des tissus en imagerie échographique. L'algorithme est détaillé dans [Basarab *et al.* (2008)]. Pour chaque bloc extrait des images de phase et réparti sur une grille de calcul, le déplacement est estimé à l'aide du modèle bilinéaire. Enfin, le champ dense de mouvement est calculé par interpolation linéaire à partir du déplacement des points de la grille.

Afin d'améliorer la précision de l'estimation, une méthode de raffinage global est proposée dans ce qui suit. Pour deux images successives i_t et i_{t+1}, une première estimation du champ de déplacement (d_x^0, d_y^0) est obtenue comme décrit dans la section précédente:

$$\left[d_x^0(x,y), d_y^0(x,y)\right] = \Delta\left[i_t(x,y), i_{t+1}(x,y)\right],$$

où Δ est l'estimateur de mouvement décrit précédemment. Basé sur de ce champ de mouvement et la première image $i_t(x,y)$, une image intermédiaire $\hat{i}_{t+1}^1(x,y)$ est générée.

La valeur de chaque pixel de $\hat{i}_{t+1}^1(x,y)$ est obtenue par interpolation spline. Idéalement, l'image générée par $\hat{i}_{t+1}^1(x,y)$ et l'image $i_{t+1}(x,y)$ devraient contenir les mêmes informations de phase. Cependant, en pratique, ce n'est pas vrai à cause des erreurs d'estimation sur le mouvement. Par conséquent, un champ de déplacement compensé $[d_{xc}^1(x,y), d_{yc}^1(x,y)]$ est estimé entre les images $\hat{i}_{t+1}^1(x,y)$ et $i_{t+1}(x,y)$ par la même méthode bilinéaire proposée basée sur la phase. Ensuite, le champ de mouvement estimé $[d_x(x,y), d_y(x,y)]$ est obtenu avec une amélioration de précision entre les deux images successives i_t et i_{t+1} . Ce processus peut être réitéré plusieurs fois. Cette méthode itérative contribue à améliorer le résultat de l'estimation du déplacement $[d_x(x,y), d_y(x,y)]$.

Estimation du mouvement Lagrangien

Le champ de mouvement Lagrangien représente le déplacement spatial des points matériels dans l'état de référence (première image) au cours du temps. Ce champ de déplacement spatio-temporel $[u_L(x,y), v_L(x,y)]$ est calculé par intégration du champ de mouvement Eulérien $[d_x(x,y), d_y(x,y)]$. Pour un champ de mouvement entre les temps t et $t+1$, nous calculons le champ de mouvement Lagrangien $[u_L(x,y,t+1), v_L(x,y,t+1)]$ à partir du champ de mouvement Lagrangien $[u_L(x,y,t), v_L(x,y,t)]$ au temps t et du champ

de mouvement de Eulerien $[d_x(x,y,t+1), d_y(x,y,t+1))]$ $[d_x(x,y,t+1), d_y(x,y,t+1))]$ au temps $t+1$:

$$u_L(x,y,t+1) = u_L(x + d_x(x,y,t+1), y + d_y(x,y,t+1), t),$$
$$v_L(x,y,t+1) = v_L(x + d_x(x,y,t+1), y + d_y(x,y,t+1), t),$$

avec les conditions initiales $u_L(x,y,1) = d_x(x,y,1)$, $v_L(x,y,1) = d_y(x,y,1)$. Une interpolation bilinéaire est appliquée pour calculer le champ de mouvement $u_L(x + d_x(x,y,t+1), y + d_y(x,y,t+1), t)$ et $v_L(x + d_x(x,y,t+1), y + d_y(x,y,t+1), t)$.

Le champ de mouvement Lagrangien nous permet de calculer le tenseur des déformations et de suivre une région en déplacement au cours du temps. La déformation du myocarde est un indicateur majeur pour le diagnostic de la fonction cardiaque [Qian *et al.* (2011)]. Elle peut être calculée à partir des dérivées spatiales par rapport au temps du champ de mouvement Lagrangien $\mathbf{u} = [u_L(x,y,t), v_L(x,y,t)]$. Le tenseur des déformations de Green-Lagrange est défini comme:

$$\mathbf{E} = \frac{1}{2}\left(\nabla\mathbf{u} + \nabla\mathbf{u}^T + \nabla\mathbf{u}^T\nabla\mathbf{u}\right),$$

où ∇ est l'opérateur dérivée spatiale et $\mathbf{u}^T$ est la transposition de $\mathbf{u}$. En outre, la déformation radiale E_{rr} dans la direction $\mathbf{r}$ et la déformation circonférentielle E_{cc} dans la direction $\mathbf{c}$ sont obtenues par:

$$E_{rr} = \mathbf{r}^T\mathbf{E}\mathbf{r}, \quad E_{cc} = \mathbf{c}^T\mathbf{E}\mathbf{c}.$$

En plus, étant donné un point x_0, y_0, la trajectoire lagrangienne au temps t d'un point matériel de coordonnées $T(x_0, y_0, t)$ est :

$$T(x_0, y_0, t) = [x_0 + u_L(x_0, y_0, t), y_0 + v_L(x_0, y_0, t)].$$

La déformation et le suivi d'une région en déplacement fournissent une information quantitative du comportement du myocarde. Plusieurs simulations et des résultats cliniques sont présentés dans le chapitre suivant.

Conclusion

Nous avons proposé dans ce chapitre une méthode d'estimation du mouvement appliquée aux séquences d'IRM marquées. Cette méthode est basée sur les phases du signal analytique défini sur un quadrant-unique du plan de Fourier. Ces phases permettent de résoudre le problème d'ouverture de l'équation du flux optique. Dans la méthode proposée, le modèle bilinéaire locale et une méthode de raffinage globale sont utilisés pour améliorer la précision de l'estimation du déplacement dans les séquences du myocarde d'IRM marquée. Ainsi, le déplacement entre deux images successives est obtenu. En appliquant la

méthode proposée à une séquence, nous avons présenté le résultat du déplacement Lagrangien. Afin d'évaluer les performances de cette méthode, plusieurs tests sont réalisés sur des données synthétiques et des données cliniques.

I.5 Les résultats de simulations et les résultats cliniques de la méthode d'estimation de mouvement myocarde basée sur la phase

L'algorithme d'estimation proposé dans le chapitre précédent est évalué sur des données synthétiques et cliniques. Les déplacements Eulérien et Lagrangien [Ricco and Tomasi (2012)] sont examinées dans l'évaluation, et correspondent, respectivement, aux déplacements entre deux images successives et aux déplacements cumulés (des points de trajectoire dans le temps). L'erreur d'amplitude entre les 2 vecteurs [Fleet and Jepson (1990)] est utilisée pour l'évaluation du déplacement Eulérien. De plus, à partir du champ de mouvement de Lagrange, nous présentons la déformation du myocarde et les résultats du suivi de région locale. Le tenseur de Green-Lagrange [Belytschko *et al.* (2013)] est utilisée pour calculer la déformation radiale et circonférentielle [Petitjean *et al.* (2005)]. Ensuite, la déformation du myocarde et les résultats du suivi de région locale sont présentés et discutés, pour deux cas cliniques présentant des pathologies cardiaques. Le pseudo-code de la méthode d'estimation de mouvement proposé entre deux images consécutives est donné dans l'algorithme 1.

Données de simulations

La méthode proposée a été testée sur des séquences réelles d'imagerie par résonance magnétique (IRM) marquées correspondant à un cycle cardiaque, simulée avec le logiciel ASSESS [Clarysse *et al.* (2011)]. Avec ce simulateur, il est possible de simuler une séquence IRM du myocarde en petit axe en combinant une rotation, un épaississement et une contraction au cours d'un cycle cardiaque. Il est également possible d'introduire une anomalie du mouvement local en diminuant l'amplitude de la contraction du myocarde dans un secteur [Clarysse *et al.* (2000)]. Le mouvement simulé sera utilisé comme référence

pour évaluer la méthode proposée. Plusieurs simulations ont été générées en agissant sur les paramètres. Les noms des séquences simulées sont données dans le tableau 5.1. “256” ou “160” pour la résolution de chaque carré de pixels, “D20” pour la contraction/expansion de 20%, “R20” pour une rotation de 20 degrés, “F20” ou “F34” pour le nombre d'images de 20 ou 34, et “P0” pour le cas sain et “P3” pour un état pathologique avec une forte anomalie du mouvement du myocarde.

Afin d'évaluer la robustesse de notre méthode, nous avons également généré une séquence permettant d'imposer un non-respect de la conservation de l'intensité du pixel au fil du temps, nommée “160D30R20P3F34Lum” dans le tableau 5.1. Dans chaque image de la séquence, on a changé son intensité par une valeur de pourcentage aléatoire de 40% et 100% de l'intensité initiale. Pour modifier l'intensité de chaque image de la séquence, nous avons multiplié l'image d'origine par une image de pondération 2D $(a + (1 - a)G(x, y))$, $G(x, y)$, avec une fonction Gaussienne. La gamme de l'image de pondération 2D est $(a, 1]$, où a est une valeur réelle aléatoire limitée à $[0.4, 1]$. En conséquence, on obtient une séquence avec l'intensité de pixel de 40% et 100% de l'intensité de l'image originale. Ici nous avons choisi la valeur minimale $a = 0, 4$ dans le but de conserver au moins 40% de l'intensité des images originales. La Fig. 5.1 montre un exemple. Nous notons que les deux images de phase détiennent l'information structurelle et sont moins influencées par les images d'intensité.

Méthodes de comparaisons

Étant donné que la méthode proposée se fonde sur les équations de signal analytique et du flux optique (plus précisément sur le flux de phase), les résultats de l'évaluation d'un estimateur du signal analytique et estimateur de flux optique sont présentés dans un objectif de comparaison. La première est la méthode du signal monogénique d'Alessandrini pour l'analyse du mouvement cardiaque à partir d'images médicales [Alessandrini *et al.* (2013)]. Elle est plus performante que la méthode SinMod [Arts *et al.* (2010)] et est plus précise avec un temps de calcul plus faible que l'autre algorithme basé sur le signal monogénique [Zang *et al.* (2007)]. La deuxième méthode utilisée pour la comparaison est appelée Sun classique NL [Sun *et al.* (2010)]. Elle a été déclaré le meilleur algorithme de flux optique en 2010 dans le classement de l'évaluation Middlebury [Baker *et al.* (2007), Baker *et al.* (2011)] (utilisé pour l'évaluation d'algorithmes de flux optique). Cette méthode a également été remarquée pour donner de bons résultats avec les nouveaux données d'évaluation en 2012 comme Kitti [Geiger *et al.* (2012)] (plate-forme de conduite autonome pour développer de nouveaux points de repère pour les tâches de stéréo, le flux optique, et la détection d'objet 3D) et MPI Sintel [Butler *et al.* (2012)] (nouvelles données de flux optique dérivé du film d'animation 3D Sintel). Ainsi, ces deux algorithmes pourraient être considérés comme des références appropriées.

Critère d'évaluation

L'erreur angulaire (AE) et l'erreur d'amplitude entre les 2 vecteurs (EE) sont des critères communs pour évaluer la différence entre les déplacements théoriques et estimés. Cependant, AE est moins adapté pour les petits déplacements [Alessandrini *et al.* (2013)] et l'EE est une mesure plus appropriée de la précision de vecteur de déplacement [Baker *et al.* (2011)]. Par conséquent, nous avons utilisé EE pour évaluer la précision de l'estimation. Les moyennes et les écarts-types de l'EE à la fois pour les déplacements Eulériens et Lagrangiens sont calculés pour quantifier la performance de la méthode. Les valeurs d'EE obtenus pour plusieurs séquences de résultats de simulation sont présentées et discutés dans ce chapitre.

Résultats d'estimation du mouvement Eulérien

Le tableau 5.1 montre les résultats de l'EE pour les sept séquences simulées. Pour chaque séquence, nous calculons une valeur moyenne d'EE μ et l'écart type σ. Toutes les méthodes ont été mises en oeuvre dans MATLAB, sur un ordinateur portable (CPU: Intel i7-4750HQ 2.0GHz, RAM: 16384MB). Les tableaux 5.1 et 5.2 montrent nos résultats par rapport aux méthodes Alessandrini et Sun classicNL. A partir de la somme des résultats de l'EE des sept séquences, les erreurs de la méthode proposée sont réduits, respectivement, de 33% et 35%, comparées avec celle d'Alessandrini et celle de Sun. Sur la séquence d'intensité variable "160D30R20P3F34Lum" et la séquence d'intensité constante "160D30R20P3F34," le procédé proposé fournit une estimation robuste. Par ailleurs, en offrant un meilleur résultat d'estimation de mouvement, la méthode proposée est d'environ 28% plus rapide que la méthode de Sun, bien que le procédé Alessandrini soit dépassé par la méthode proposée, il est moins long que les deux autres approches.

La Fig. 5.2 présente une comparaison image-par-image du critère EE pour trois séquences. Ces séquences présentent différents types de mouvements: rotation pur pour la séquence "256R20F20", contraction/extension pure pour la séquence "256D30F20", et la rotation + contraction/extension + déformation de la séquence "160D30R20P3F34". Les séquences "256R20F20" et "256D30F20" contiennent 7 images dans la phase systolique et 13 images dans la phase diastolique d'un cycle cardiaque. La séquence "160D30R20P3F34" contient de 14 et 20 images dans les phases systolique et diastolique, respectivement.

Les performances des trois méthodes ont été étudiées en détails sur la séquence " 160D30R20P3F34". La Fig. 5.3 compare les résultats de l'EE entre les trois méthodes sur une image systolique et un image diastolique. Dans le résultat d'image systolique (première ligne), la méthode proposée génère des valeurs d'erreurs plus petites. Dans le résultat d'image diastolique (deuxième ligne), il n'y a pas de différence observable très nette entre les trois méthodes. Afin de mieux comprendre la performance des procédés, il est important d'analyser le déplacement vertical et horizontal séparément. En conséquence, la Fig. 5.4 présente ces résultats pour l'image 10, qui possède l'un des plus grands déplacements entre

deux images successives au cours du cycle cardiaque.

Résultats d'estimation du mouvement Lagrangien

Le champ de mouvement de Lagrange $[u_L(x,y,t), v_L(x,y,t)]$ au temps t est obtenu à partir de l'intégration du champ de mouvement d'Euler $[d_x, d_y]$. La déformation radiale E_{rr} dans la direction $\mathbf{r}$ et la déformation circonférentielle E_{cc} dans la direction $\mathbf{c}$ sont définies dans Eq. (4.34). Elles sont calculées à partir des dérivées spatiales du champ de mouvement de Lagrange $\mathbf{u} = [u_L(x,y,t), v_L(x,y,t)]$.

Dans les séquences "160D30R20P0F34" et "160D30R20P3F34," les déformations systolique radiale et circonférentielle ont été calculées. La Fig. 5.6 montre la déformation du myocarde à la image 14 de la séquence "160D30R20P0F34". L'uniformité de la déformation est observable dans ce cas sain à la fois sur la référence et sur les résultats de la méthode proposée.

La Fig. 5.7 montre la déformation radiale et circonférentielle pour le cas pathologique (séquence "160D30R20P0F34"). Les quatre colonnes sont dans l'ordre: la vérité terrain, le résultat par le procédé proposé, le résultat d'Alessandrini, et le résultat Sun classicNL. Une région de pathologie simulée est située dans la partie supérieure gauche du myocarde (indiqué par une flèche sur la figure). D'après les résultats de déformation radiale E_{rr}, les trois méthodes peuvent récupérer la pathologie, tandis que dans les résultats de déformation circonférentielle, notre méthode proposée obtient un emplacement de pathologie plus précis que les deux autres méthodes.

Résultats cliniques

Dans cette section, nous avons appliqué notre méthode à des séquences cliniques in vivo de cas pathologiques d'une patiente de 43 ans et d'un patient de 65 ans. La patiente de 43 ans a un infarctus du myocarde. Elle a été hospitalisée pour une occlusion de l'artère descendante antérieure gauche (LAD), avec une réperfusion effectuée à H+2. La Fig. 5.8(a) représente la première image (fin de diastole) d'une coupe petit axe- située entre le niveau médian et apicale du ventricule gauche. Le myocarde est divisé par le modèle de segmentation du ventricule gauche de l'American Heart Association (AHA) segmentation [Cerqueira *et al.* (2002)]. La Fig. 5.8(b) montre l'image Late gadolinium (LGE) au même niveau de la tranche, avec les indications des segments: A, Antérieur; AS, Antéro-septal; IS, Inféro-septal; I, Inférieur; IL, Inféro-latéral; AL, Antéro-latéral. L'infarctus du myocarde apparaît dans les régions en hyper-signal (segments AS, A, et IS) avec des régions sombres dans les couches sous-endocardiques correspondant à des régions ayant le phénomène de no-reflow. L'application de la méthode proposée pour cette séquence d'IRM clinique marquée, le champ de mouvement de Lagrange est obtenue en cumulant le champ de mouvement d'Euler. La Fig. 5.9 représente le champ de mouvement de Lagrange et la déformation radiale (E_{rr}) à l'image 13 (fin de la systole, correspondant

à la contraction maximale). Dans la Fig. 5.9(a), l'amplitude du mouvement dans les segments A, AS et IS et sont visiblement plus faibles que dans les segments AL, IL, et I, ce qui est évidemment en accord avec l'emplacement de la pathologie. En raison de l'épaississement du myocarde pendant la systole, la déformation radiale est généralement positive dans le myocarde normal. La Fig. 5.9(b) montre les valeurs du E_{rr} réduit, voire négative, dans la région antérieure pathologique.

Les trajectoires de points matériels sont affichés dans la Fig. 5.10. Elles fournissent une expérience visuelle de la trace de mouvement local du myocarde. Plusieurs points sont choisis sur la première image de la séquence telle que les points de suivi souhaités. De l'image en petit axe sur la Fig. 5.10(a), nous mettons en évidence clairement que, pendant le cycle cardiaque, le segment AS a un mouvement diminué par rapport aux autres segments dans le myocarde adjacent ou à distance. En outre, en vue long-axe montrée sur la Fig. 5.10(b), nous illustrons également une diminution des mouvements dans les segments antéro-septal, apical et apical inférieur (dans le cercle pointillé blanc). La ligne blanche montre la croix-emplacement de la vue en petit axe de la Fig. 5.10(a). Par conséquent, ces résultats de suivi sont en mesure de donner une alternative pour la visualisation des pathologies.

Le deuxième cas clinique illustre un infarctus du myocarde inférieur chez un homme de 65 ans. L'imagerie a été réalisée avant la sortie du patient au jour 5. La Fig. 5.11(a) montre l'image en petit axe en fin de diastole d'une séquence MR marquée au niveau médian du ventricule gauche. La Fig. 5.11(b) montre l'image de LGE au même niveau de la tranche que l'image dans la Fig. 5.11(a). Les segments anormaux correspondant à la nécrose myocardique sont notamment les segments SI, I, et IL, avec la présence de non-reperfusion (hyposignal sous-endocardique) dans les segments I et IL. Le champ de mouvement estimé en fin de systole dans la Fig. 5.12(a) montre que le myocarde est pratiquement divisé en deux parties: l'une supérieure (antérieure) avec un mouvement centripète de l'amplitude normale, et la paroi inférieure avec une diminution importante de l'amplitude. La carte de déformation radiale dans la Fig. 5.12(b) illustre également le contraste entre les parties antérieure et inférieure de la circonférence du myocarde. Dans les segments SI, I, et IL, on peut trouver que la plupart des valeurs de déformation négatives et les petites valeurs positives sont dans la partie inférieure du myocarde.

Les trajectoires de Lagrange de point matériel dans la Fig. 5.13(a) donnent une vue globale de l'ensemble de la séquence en long axe. Dans les régions antérieures à distance des segments A et AL (principalement), les traces sont lisses et de grande amplitude. Dans les segments anormaux dessinés par le cercle en pointillés, les traces sont tordues et écourtées, ce qui démontre le manque de capacités contractiles dans ces régions infarctus. Afin de mieux mettre en évidence la différence entre les résultats de suivi de la région de myocarde sains et pathologiques, la Fig. 5.13(b) présente les résultats du suivi d'un myocarde sain d'un volontaire. Nous pouvons voir dans ce cas sain que tous les points suivis ont un mouvement de contraction et dilatation uniformes, qui sont différents du comportement de mouvement des cas pathologiques.

Conclusion

La performance de la méthode d'estimation de mouvement proposée dans le chapitre 4 est évaluée avec plusieurs types de séquences simulées. Par rapport aux deux autres méthodes efficaces (Alessandrini et Sun classicNL), la méthode proposée conduit à une réduction notable des erreurs d'estimation. De plus, la méthode proposée est moins sensible à la fois à la variation d'intensité des pixels dans le temps et la faiblesse de contraste des séquences. Ces deux phénomènes se produisent généralement dans des situations cliniques réelles. En outre, en appliquant la méthode proposée pour deux cas cliniques de pathologies, nous avons présenté les déformations radiales sur les images de fin de systole, ainsi que les résultats de suivi de région local du myocarde. Nos résultats distinguent entre les différents comportements de mouvement des régions locales du myocarde. Nous avons également souligné que les résultats de suivi locaux sont potentiellement un indicateur utile pour les anomalies du mouvement cardiaque.

II Background

Chapter 1

Introduction

1.1 Motivation

Cardiovascular disease (CVD) is the cause of half of all deaths in developed countries, and it is also a major cause of death in many developing countries. Every year since 1900 except 1918, CVD has accounted for more deaths than any other major cause of death in the United States. On the basis of the 2010 death rate data, an average of one death by CVD occurred every 40s. An estimated 83.6 million American adults have more than one type of CVD. Of these, 42.2 million are estimated to be more than 60 years of age [Go *et al.* (2014)]. CVD is the leading cause of death in adults.

As reported in [Go *et al.* (2014)]: "Coronary heart disease (CHD) alone caused ≈1 of every 6 deaths in the United States in 2010. In 2010, 379559 Americans died of CHD. Each year, an estimated ≈620 000 Americans have a new coronary attack (defined as first hospitalized myocardial infarction or coronary heart disease death) and ≈295000 have a recurrent attack. It is estimated that an additional 150000 silent first myocardial infarctions occur each year. Approximately every 34 seconds, one American has a coronary event, and approximately every 1 minute 23 seconds, an American will die of one."

A key to preventing CVD is to know the warning signs of a heart attack. Researchers have found certain indicators from studies involving thousands of patients. These indicators play an important role in the chances of developing heart disease. The early screening and diagnosis results of myocardial motion abnormality, one of the indicators, are usually considered an important element in CHD diagnosis. This can be assessed from dynamic image acquisition in magnetic resonance imaging (MRI) and ultrasound imaging.

1.2 Thesis objective

Two main objectives drive this thesis. The first is to propose complex/hypercomplex signals and to define the local phases and local amplitude. The proposed hypercomplex signals should be able to extend into the higher dimension within a uniform definition. The properties of the complex/hypercomplex signals should correspond to our application purpose, such as 2D/3D amplitude and local phase calculation. The second objective is to propose a motion estimation method based on the local phase information of cardiac image sequences. The definition of the complex/hypercomplex signal phase should be suitable to estimate the motion of the tagged MRI sequence. Since there are several motion estimation methods in the literature to ensure sufficient estimation accuracy, the proposed method should achieve adequate or better estimation accuracy than the existing state-of-the-art methods.

1.3 Overview and contributions

This thesis is divided into two parts: the research work on the state of the art in chapter 2 and the contributions on hypercomplex signal study in chapter 3 and the myocardium motion estimation algorithm in chapters 4, and 5.

Chapter 2 studies the existing techniques available. A review of the literature on the complex/hypercomplex analytic signal is given for 2D and nD. Then the applications in the domain of motion estimation on the phase information of the analytic signal are presented. Finally, several studies on myocardial motion estimation are presented.

Chapter 3 presents the two types of extension: extension from a 2D signal to a 3D signal and extension from the classical complex signal to the hypercomplex signal within the framework of Clifford algebra. A 3D hypercomplex signal is defined in this chapter, which is called the 3D Clifford analytic signal. Several introductive examples and an application of the 3D Clifford analytic signal are presented at the end of this chapter.

Chapter 4 proposes a method for myocardial motion estimation. This motion estimation method is based on two spatial phases of the 2D analytic signal applied to tagged cardiac MRI sequences. By combining the information of these phases from the analytic signals of two successive frames, we propose an analytical estimator for 2D local displacements. To improve the accuracy of the motion estimation, a local bilinear deformation model is used within an iterative estimation scheme. The main advantages of this method are that the phase-based method allows the displacement to be estimated with subpixel accuracy and is robust to image intensity variation in time, and preliminary filtering (e.g., image smoothing) is not required because of the bilinear model.

Chapter 5 gives the results of the method proposed in chapter 4. The motion estimation results from seven realistic simulated tagged magnetic resonance imaging (MRI) sequences show that the method proposed herein is more accurate than the monogenic signal phase-based method and the classical optical-flow-based method. Cardiac strains are

computed from the estimated displacement fields. The frame-to-frame displacements are further accumulated in time to provide for the calculation of myocardial point trajectories. Indeed, from the estimated trajectories in time on two patients with infarcts, the shapes of the trajectories of myocardial points belonging to pathological regions are clearly reduced in magnitude compared to those from normal regions. Myocardial point trajectories, estimated from this phase-based analytic signal approach, are therefore a promising indicator of local cardiac dynamics. Moreover, they are shown to be coherent with the estimated deformation of the myocardium.

Chapter 2

State of the art

For the past two decades, several types of 2D complex/hypercomplex signals have been proposed as extensions of Gabor's analytic signal. A complex signal and hypercomplex signal result from the addition of several signals, which gives several definitions of complex and hypercomplex signals. To study higher-dimension hypercomplex signals, several previous studies are reviewed in this chapter. For the present work on cardiac motion estimation using a complex signal, we first review various algorithms based on the phase of the complex and hypercomplex signal for the different applications of motion estimation and then the studies focusing on myocardial motion estimation.

2.1 2D Complex and hypercomplex signals

This part introduces the main 2D complex signals: the complex analytic signal, the quaternionic signal, and the monogenic signal. However, one of the basic tools of complex signals is the Hilbert transform.

2.1.1 2D complex signals with single-quadrant spectra

Two-dimensional complex signals with single-quadrant spectra were proposed by Hahn [Hahn (1992)]. This signal can be obtained by 2D complex Fourier transformation by taking one quadrant's information in its frequency spectrum.

2D Complex Fourier transform and Hermitian symmetry of the Fourier spectrum

The forward complex Fourier transform for a 2D input real signal $f(x, y)$ is:

$$F(u, v) = \iint f(x, y) e^{-i' 2\pi (ux+vy)} dxdy, \tag{2.1}$$

where i' is the usual complex imaginary. The inverse Fourier transform is:

$$f(x, y) = \iint F(u, v) e^{i' (ux+vy)} dudv. \tag{2.2}$$

We have the properties

$$F^{-1}\left[sign\left(u\right)\right] = \frac{i'\delta\left(y\right)}{\pi x}, \tag{2.3}$$

$$F^{-1}\left[sign\left(v\right)\right] = \frac{i'\delta\left(x\right)}{\pi y}, \tag{2.4}$$

$$F^{-1}\left[sign\left(u\right) sign\left(v\right)\right] = \frac{-1}{\pi^2 xy}, \tag{2.5}$$

with

$$sign(x) = \begin{cases} 1 & \text{if } x > 0 \\ 0 & \text{if } x = 0 \\ -1 & \text{if } x < 0 \end{cases}. \tag{2.6}$$

In order to compute the 2D AS, the Hermitian symmetry property of this 2D FT is needed, defined by:

$$\begin{aligned} F(u, v) &= F^*(-u, -v), \\ F(-u, v) &= F^*(u, -v), \end{aligned} \tag{2.7}$$

with the symbol $*$ denoting the complex conjugate. As a result of this Hermitian symmetry, the input signal can be recovered from any of its half-plane spectrum, i.e., a half-plane with respect to any line that crosses the origin point in the frequency spectrum coordinate. For example, in Fig. 2.1, we can choose the half-plane of $u > 0$ for a simpler relation. Then the other half-plane can be represented by Eq. (2.7).

2D Hilbert transform

2D total Hilbert transform For a 2D real signal $f(x, y)$, the definition of the 2D total Hilbert transform is given by:

$$H\{f(x, y)\} = f(x, y) \star\star \frac{1}{\pi^2 xy}, \tag{2.8}$$

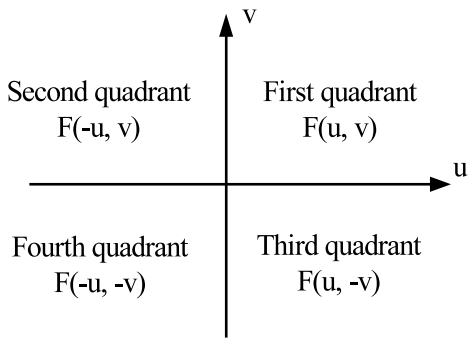

Figure 2.1: The four-quadrant Fourier spectrum of a 2D real signal in the frequency domain.

with $\star\star$ denoting the 2D convolution operation, and in the frequency domain, the definition is:

$$F_H(u,v) = -F(u,v)sign(u)sign(v), \tag{2.9}$$

with u, v, representing the spatial frequencies. $F_H(u,v)$ and $F(u,v)$ are the Fourier transform of $H\{f(x,y)\}$ and $f(x,y)$ respectively.

2D partial Hilbert transforms For a 2D real signal $f(x,y)$, the definitions of 2D partial Hilbert transform of the x-direction $H_x\{f(x,y)\}$ and for the y-direction $H_y\{f(x,y)\}$ are given, respectively, by:

$$H_x\{f(x,y)\} = f(x,y) \star\star \frac{\delta(y)}{\pi x}, \tag{2.10}$$

$$H_y\{f(x,y)\} = f(x,y) \star\star \frac{\delta(x)}{\pi y}, \tag{2.11}$$

and in the frequency domain, the definitions are:

$$F_{H_x}(u,v) = -i' F(u,v)sign(u), \tag{2.12}$$

$$F_{H_y}(u,v) = -i' F(u,v)sign(v). \tag{2.13}$$

Here, i' is the usual complex imaginary, $F_{H_x}(u,v)$, $F_{H_y}(u,v)$ and $F(u,v)$ are the Fourier transform of $H_x\{f(x,y)\}$, $H_y\{f(x,y)\}$ and $f(x,y)$ respectively.

2D Hahn single-quadrant AS

The half-plane spectrum of the first quadrant and the third quadrant in Fig. 2.1 is chosen. The single-quadrant 2D AS from the first and the third quadrant of the spectrum can be defined as $\psi_1(x,y)$ and $\psi_3(x,y)$, respectively. Moreover, by [Hahn (1992)], the 2D

AS from the second and fourth quadrants $\psi_2(x,y)$ and $\psi_4(x,y)$ are:

$$\psi_2(x,y) = \psi_3^*(x,y), \tag{2.14}$$
$$\psi_4(x,y) = \psi_1^*(x,y). \tag{2.15}$$

The definition of $\psi_1(x,y)$ and $\psi_3(x,y)$ is given by:

$$\begin{aligned}
\psi_1(x,y) &= f(x,y) \star\star \left\{ [\delta(x) + \frac{i'}{\pi x}][\delta(y) + \frac{i'}{\pi y}] \right\} \\
&= f(x,y) \star\star \left[\delta(x)\delta(y) + e_1 \frac{\delta(y)}{\pi x} + e_1 \frac{\delta(x)}{\pi y} + (-1)\frac{\delta(x)\delta(y)}{\pi^2 xy} \right] \\
&= f + i' H_x\{f\} + i' H_y\{f\} - H\{f\} \\
&= (f - H\{f\}) + i'(H_x\{f\} + H_y\{f\}) \\
&= a_1 e^{i'\varphi_1} = a_1 \cos\varphi_1 + i' a_1 \sin\varphi_1, \qquad (2.16) \\
\psi_3(x,y) &= f(x,y) \star\star \left\{ [\delta(x) + \frac{i'}{\pi x}][\delta(y) - \frac{i'}{\pi y}] \right\} \\
&= f(x,y) \star\star \left[\delta(x)\delta(y) + e_1 \frac{\delta(y)}{\pi x} - e_1 \frac{\delta(x)}{\pi y} + \frac{\delta(x)\delta(y)}{\pi^2 xy} \right] \\
&= f + i' H_x\{f\} - i' H_y\{f\} + H\{f\} \\
&= (f + H\{f\}) + i'(H_x\{f\} - H_y\{f\}) \\
&= a_3 e^{i'\varphi_3} = a_3 \cos\varphi_3 + i' a_3 \sin\varphi_3, \qquad (2.17)
\end{aligned}$$

where i' is the usual complex imaginary, $H\{f\}$ is the total Hilbert transform. $H_x\{f\}$ and $H_y\{f\}$ are the partial Hilbert transforms. a_1 and φ_1 are the amplitude and the phase of $\psi_1(x,y)$, respectively, and are given by:

$$a_1 = \sqrt{f^2 + H\{f\}^2 + H_x\{f\}^2 + H_y\{f\}^2 + 2(H_x\{f\}H_y\{f\} - fH\{f\})}, \tag{2.18}$$
$$\varphi_1 = Arg[(f - H\{f\}) + i'(H_x\{f\} + H_y\{f\})], \tag{2.19}$$

and a_3 and φ_3 are the amplitude and the phase of $\psi_3(x,y)$, respectively:

$$a_3 = \sqrt{f^2 + H\{f\}^2 + H_x\{f\}^2 + H_y\{f\}^2 - 2(H_x\{f\}H_y\{f\} - fH\{f\})}, \tag{2.20}$$
$$\varphi_3 = Arg[(f + H\{f\}) + i'(H_x\{f\} - H_y\{f\})]. \tag{2.21}$$

2.1.2 Quaternionic analytic signal

The quaternionic Fourier transform (QFT) was firstly introduced by Ernst [Ernst *et al.* (1987)] and Delsuc [Delsuc (1988)], and then by Ell [Ell (1993)] in 1993 and also by Bülow and Sommer [Bülow and Sommer (1997)] in 1997. For the 2D real signal $f(x,y)$, its QFT $F(u,v)$ is defined by:

$$F(u,v) = \iint e^{-i2\pi ux} f(x,y) e^{-j2\pi vy} dxdy, \tag{2.22}$$

and the inverse QFT (IQFT) is defined by:

$$f(x,y) = \iint e^{i2\pi ux} F(u,v) e^{j2\pi vy} du dv. \tag{2.23}$$

Based on the QFT and IQFT, the quaternionic analytic signal (QS) with a single quadrant spectrum is defined by:

$$\begin{aligned}\psi_q(x,y) &= \iint e^{i2\pi ux}[1+sign(u)][1+sign(v)]F(u,v)e^{j2\pi vy}dudv \\ &= f + iH_x\{f\} + jH_y\{f\} + kH\{f\},\end{aligned} \tag{2.24}$$

with $k = ij$. Here the filter $[1+sign(u)][1+sign(v)]$ enables us to obtain the first-quadrant spectrum of $F(u,v)$. The conjugate $(\psi_q)_c$ of ψ_q is defined by:

$$(\psi_q)_c = f - iH_x\{f\} - jH_y\{f\} - kH\{f\}. \tag{2.25}$$

A widely used type of polar form of QS in Eq. (2.24) is defined by Bülow [Bülow (1999)]:

$$\psi_q(x,y) = |\psi_q(x,y)|\, e^{i\phi_i(x,y)} e^{k\phi_k(x,y)} e^{j\phi_j(x,y)}, \tag{2.26}$$

with the amplitude

$$|\psi_q| = \sqrt{f^2 + H\{f\}^2 + H_x\{f\}^2 + H_y\{f\}^2}, \tag{2.27}$$

and the phases $\phi_i \in [-\pi, \pi[$, $\phi_j \in [-\frac{\pi}{2}, \frac{\pi}{2}[$, $\phi_k \in [-\frac{\pi}{4}, \frac{\pi}{4}]$.

A summary for the computation of phases is given as follows:

- Normalize the QS by:

$$q = \frac{\psi_q(x,y)}{|\psi_q(x,y)|} = q_0 + iq_1 + jq_2 + kq_3, \tag{2.28}$$

  then, $\phi_k = -\frac{1}{2} arcsin\left(2\left(q_1q_2 - q_0q_3\right)\right)$.

- If $\phi_k \neq \pm\frac{\pi}{4}$, then:

$$\phi_i' = \frac{1}{2} atan2\left(2\left(q_2q_3 + q_0q_1\right), q_0^2 - q_1^2 + q_2^2 - q_3^2\right), \tag{2.29}$$

$$\phi_j = \frac{1}{2} atan2\left(2\left(q_1q_3 + q_0q_2\right), q_0^2 + q_1^2 + q_2^2 - q_3^2\right). \tag{2.30}$$

- If $\phi_k = \pm\frac{\pi}{4}$, take $\phi_j = 0$, then we find:

$$\phi_i' = \frac{1}{2} atan2\left(2\left(-q_2q_3 + q_0q_1\right), q_0^2 - q_1^2 - q_2^2 + q_3^2\right). \tag{2.31}$$

- If $e^{i\phi_i'} e^{k\phi_k} e^{j\phi_j} = -q$, set $\phi_i = \phi_i' + \pi$, else $\phi_i = \phi_i'$.

Here, the function $atan2()$ is the four-quadrant arctangent with the definition:

$$atan2\left(b,a\right)=\begin{cases} arctan\left(\frac{b}{a}\right) & a>0 \\ \pm\pi & a=0 \text{ and } sign\left(b\right)=\pm1 \\ arctan\left(\frac{b}{a}\right)-\pi & a<0 \text{ and } b<0 \\ arctan\left(\frac{b}{a}\right)+\pi & a<0 \text{ and } b\geq 0 \end{cases} \tag{2.32}$$

In addition, the QFT in Eq. (2.22) is called two-sided QFT [Georgiev *et al.* (2013), Pei *et al.* (2001)]. From the noncommutativity of the quaternions, we have also the right-sided QFT and the left-sided QFT. The "two-sided", "right-sided", and "left-sided" indicate the position of the exponential terms in the QFT definitions. Unless specified otherwise, the works in this thesis is based on the two-sided QFT.

2.1.3 Monogenic signal

The monogenic signal (MS) is another type of extension of 1D AS. It was developed by Felsberg [Felsberg and Sommer (2001), Felsberg (2002)]. For a 2D real signal $f(x,y)$, its MS $\psi_m(x,y)$ is defined by:

$$\psi_m(x,y)=f+iR_x\{f\}+jR_y\{f\}, \tag{2.33}$$

where $R_x\{f\}$ and $R_y\{f\}$ are Riesz transforms in the x and y directions, respectively. In this quaternion valued function, one finds that the Riesz transforms replace the Hilbert transforms without the term $kH\{f\}$ when compared to the QS in (2.24). The Riesz transforms are defined by:

$$R_x\{f(x,y)\}=f(x,y)\star\star\frac{x}{2\pi\left[\sqrt{x^2+y^2}\right]^3}, \tag{2.34}$$

$$R_y\{f(x,y)\}=f(x,y)\star\star\frac{y}{2\pi\left[\sqrt{x^2+y^2}\right]^3}. \tag{2.35}$$

The amplitudes of MS are:

$$|\psi_m(x,y)|=\sqrt{f^2+R_x\{f\}^2+R_y\{f\}^2}. \tag{2.36}$$

An orientation angle Φ and the phase Θ are also given in [Felsberg and Sommer (2001)]:

$$\Phi=arctan\left(\frac{R_y\{f\}}{R_x\{f\}}\right),\quad \Theta=arctan\left(\frac{\sqrt{R_x\{f\}^2+R_y\{f\}}^2}{f}\right). \tag{2.37}$$

Then MS is represented as:

$$\psi_m(x,y) = |\psi_m(x,y)|\,(cos\Theta + isin\Theta cos\Phi + jsin\Theta sin\Phi). \tag{2.38}$$

2.2 nD complex and hypercomplex analytic signals

In 2011, Hahn introduced that, depending on the choice of the algebra of the basis vectors $\{e_1, e_2, e_3, ..., e_n\}$, different definitions of the hypercomplex analytic function can be obtained [Hahn and Snopek (2011)]. He proposed a theory of nD complex and hypercomplex ASs, for the 3D hypercomplex AS, an octonionic analytic signal, by applying Cayley-Dickson algebra. In the frequency domain, the complex/hypercomplex signals are defined by the inverse complex/hypercomplex Fourier transform of a single-orthant spectrum.

2.2.1 nD complex analytic signals and the nD complex Fourier transform

The nD complex analytic signals with single-orthant spectra was introduced in [Hahn (2003)]. For an nD real signal $f(\mathbf{x})$, $\mathbf{x} = (x_1, x_2, ..., x_{n-1}, x_n)$, the nD analytic signal is:

$$\psi_c(\mathbf{x}) = \frac{1}{2^n} f(\mathbf{x}) \star \prod_{k=1}^{n} \left[\delta(x_k) + e_1 \frac{1}{\pi x_k}\right], \tag{2.39}$$

where e_1 is the usual complex imaginary unit, the same as in Eq. (2.1). The factor $\frac{1}{2^n}$ is a matter of the author's convention to normalize the energy of a signal. The signs of e_1 in Eq. (2.39) are positive. They correspond to the spectrum in the first orthant of the frequency space, and the change of signs (positive or negative) defines spectral support in other orthants.

In addition, the analytic signals can be defined alternatively from the inverse Fourier transforms of their spectra. The forward nD complex Fourier transform $F(\mathbf{u})$ ($\mathbf{u} = (u_1, u_2, ..., u_{n-1}, u_n)$) for the nD real signal $f(\mathbf{x})$ is:

$$F(\mathbf{u}) = \int_{R^n} f(\mathbf{x}) \prod_{k=1}^{n} exp(-e_1 2\pi u_k x_k) d^n\mathbf{x} = Re\left[F(\mathbf{u})\right] + e_1 Im\left[F(\mathbf{u})\right], \tag{2.40}$$

and its inverse is:

$$f(\mathbf{x}) = \int_{R^n} F(\mathbf{u}) \prod_{k=1}^{n} exp(e_1 2\pi u_k x_k) d^n\mathbf{u}, \tag{2.41}$$

where e_1 is the usual complex imaginary.

2.2.2 nD hypercomplex AS

Cayley-Dickson algebra

Hahn selected Cayley-Dickson algebra for his research. Table 2.1 defines the multiplication of Cayley-Dickson algebra with three generators e_1, e_2, and e_3. For these octonions,

$\times$	1	e_1	e_2	e_3	e_4	e_5	e_6	e_7
1	1	e_1	e_2	e_3	e_4	e_5	e_6	e_7
e_1	e_1	-1	e_3	$-e_2$	e_5	$-e_4$	$-e_7$	e_6
e_2	e_2	$-e_3$	-1	e_1	e_6	e_7	$-e_4$	$-e_5$
e_3	e_3	e_2	$-e_1$	-1	e_7	$-e_6$	e_5	$-e_4$
e_4	e_4	$-e_5$	$-e_6$	$-e_7$	-1	e_1	e_2	e_3
e_5	e_5	e_4	$-e_7$	e_6	$-e_1$	-1	$-e_3$	e_2
e_6	e_6	e_7	e_4	$-e_5$	$-e_2$	e_3	-1	$-e_1$
e_7	e_7	$-e_6$	e_5	e_4	$-e_3$	$-e_2$	e_1	-1

Table 2.1: Cayley multiplication with three generators e_1, e_2, and e_3 [Hahn and Snopek (2011)].

we have $e_i e_j = -e_j e_i$, $e_i(e_j e_k) = -(e_i e_j)e_k$. Each e_i has three different representations $e_i = e_j e_k$ and $-e_i = e_k e_j$.

nD hypercomplex AS and Fourier transform

For an nD real signal $f(\mathbf{x})$, $\mathbf{x} = (x_1, x_2, ..., x_{n-1}, x_n)$, the nD hypercomplex analytic signal is:

$$\psi(\mathbf{x}) = f(\mathbf{x}) \star \prod_{k=1}^{n} \left[\delta(x_k) + e_k \frac{1}{\pi x_k}\right], \tag{2.42}$$

where e_k are the imaginary unit, and one of the choice of the algebra of the imaginary units can be the octonions. The signs of e_k in Eq. (2.42) are positive. This corresponds to the spectrum in the first orthant of the frequency space, and the sign change (positive or negative) defines spectral support in the other orthants. Compared with the imaginary unit in the nD complex analytic signal defined in Eq. (2.39), only one imaginary unit e_1 is used, for the nD hypercomplex analytic signal defined in Eq. (2.42), n imaginary units are used, which are $e_1, e_2, e_3, ..., e_k$ with $k = n$.

Choosing the imaginary units satisfying the multiplication rules of the Cayley-Dickson algebra in table 2.1, the hypercomplex Fourier transform is defined as:

$$F_{CD}(\mathbf{u}) = \int_{R^n} f(\mathbf{x}) \prod_{k=0}^{n-1} exp(-e_{2^k} 2\pi u_{k+1} x_{k+1}) d^n\mathbf{x}, \tag{2.43}$$

and its inverse is:

$$f(\mathbf{x}) = \int_{R^n} \left(\prod_{k=0}^{n-1} exp(e_{2^{n-k-1}} 2\pi u_{n-k} x_{n-k}) \right) F_{CD}(\mathbf{u}) d^n\mathbf{u}. \tag{2.44}$$

Here, the imaginary units are e_{2^k} (i.e., e_1, e_2, e_4, e_8, ...). In contradistinction to the

following section 2.2.3, Clifford biquaternion algebra applies the imaginary units: e_1, e_2, e_3, e_4, ...

2.2.3 2D+t biquaternion analytic signal in Clifford biquaternion algebra

Based on the studies of Grassmann, Hamilton and Clifford, Clifford algebras can be also called Grassmann-Hamilton-Clifford algebras or multiquaternion algebras [Girard *et al.* (2013)]. The nD analytic signal is proposed in the context of these multiquaternion algebras. It defines the nD Clifford Fourier transform with the input signal standing on the left side of all the N exponential functions.

Clifford biquaternion algebra

For $2D+t$ dimensions, 3D Clifford algebra can be used, made up of Clifford biquaternions. The quaternions are a 4D vector space. Generally, the elements of the quaternion basis are denoted as: $1, i, j$ and k. A quaternion can be represented by a linear combination of these basis elements, such as $a1+bi+cj+dk$ where a, b, c and d are real numbers. Given a quaternion $[1\, i_1\, j_1\, k_1]$, one has a quaternionic system:

$$i = i_1 \otimes 1, j = j_1 \otimes 1, k = k_1 \otimes 1, \tag{2.45}$$

here $i = i_1 \otimes 1$ is the algebraic tensor product of i_1 and 1 ($i^2 = -1$). For example: for the matrix $\mathbf{A}_{m\times n}$ and $\mathbf{B}_{p\times q}$, its algebraic tensor product $\mathbf{A} \otimes \mathbf{B}$ is a $mp \times nq$ matrix:

$$\mathbf{A} \otimes \mathbf{B} = \begin{bmatrix} a_{11}\mathbf{B} & \cdots & a_{1n}\mathbf{B} \\ \vdots & \ddots & \vdots \\ a_{m1}\mathbf{B} & \cdots & a_{mn}\mathbf{B} \end{bmatrix}. \tag{2.46}$$

Define another quaternionic system:

$$I = 1 \otimes i_1, J = 1 \otimes j_1, K = 1 \otimes k_1, \tag{2.47}$$

where I, J, K commute with i, j, k (e.g., $Ij = (1 \otimes i_1)(j_1 \otimes 1) = j_1 \otimes i_1 = jI$), then the algebra is given by the eight elements:

$$\begin{bmatrix} 1 & i & j & k \\ i'I & i'Ii & i'Ij & i'Ik \end{bmatrix}. \tag{2.48}$$

The i' is the usual complex imaginary ($i'^2 = -1$). Here we define the three generators e_1, e_2 and e_3 ($e_1 = \epsilon i, e_2 = \epsilon j, e_3 = \epsilon k, \epsilon = i'I, \epsilon^2 = 1, e_i^2 = -1$), and then obtain the full algebra:

$$\begin{bmatrix} 1 & i = e_2e_3 & j = e_3e_1 & k = e_1e_2 \\ \epsilon = i'I = -e_1e_2e_3 & e_1 = \epsilon i & e_2 = \epsilon j & e_3 = \epsilon k \end{bmatrix}. \tag{2.49}$$

$\times$	1	$\epsilon i = e_1$	$\epsilon j = e_2$	$\epsilon k = e_3$	$i = e_2e_3$	$j = e_3e_1$	$k = e_1e_2$	$\epsilon = -e_1e_2e_3$
1	1	ϵi	ϵj	ϵk	i	j	k	ϵ
$\epsilon i = e_1$	ϵi	-1	k	$-j$	$-\epsilon$	ϵk	$-\epsilon j$	i
$\epsilon j = e_2$	ϵj	$-k$	-1	i	$-\epsilon k$	$-\epsilon$	ϵi	j
$\epsilon k = e_3$	ϵk	j	$-i$	-1	ϵj	$-\epsilon i$	ϵ	$-k$
$i = e_2e_3$	i	ϵ	$-\epsilon k$	$-\epsilon j$	-1	k	$-j$	$-\epsilon i$
$j = e_3e_1$	j	$-\epsilon k$	ϵ	ϵi	$-k$	-1	i	$-\epsilon j$
$k = e_1e_2$	k	ϵj	$-\epsilon i$	$-\epsilon$	j	$-i$	-1	ϵk
$\epsilon = -e_1e_2e_3$	ϵ	i	j	k	ϵi	ϵj	ϵk	1

Table 2.2: Clifford biquaternion algebra multiplication table with three generators

The full algebra in Eq. (2.49) satisfies the multiplication rules presented in table 2.2. Then, a Clifford biquaternion A can be expressed as a general element of the algebra:

$$\begin{aligned} A &= p + \epsilon q \\ &= (p_0 + ip_1 + jp_2 + kp_3) + \epsilon(q_0 + iq_1 + jq_2 + kq_3) \\ &= [p_0, p_1, p_2, p_3] + \epsilon\,[q_0, q_1, q_2, q_3]\,. \end{aligned} \tag{2.50}$$

where p and q are quaternions. The biquaternions have the following operations:

- The product of two Clifford biquaternions A and $B = p' + \epsilon q'$:

$$\begin{aligned} AB &= (p + \epsilon q)\,(p' + \epsilon q') \\ &= (pp' + qq') + \epsilon\,(pq' + qp')\,. \end{aligned} \tag{2.51}$$

- Conjugate of Clifford biquaternion A:

$$\begin{aligned} A_c &= p_c + \epsilon q_c \\ &= [p_0, -p_1, -p_2, -p_3] + \epsilon\,[q_0, -q_1, -q_2, -q_3]\,, \end{aligned} \tag{2.52}$$

  where p_c, q_c are respectively the quaternion conjugates of p and q.

- Complex conjugate of Clifford biquaternion A:

$$\overline{A} = p - \epsilon q. \tag{2.53}$$

In addition, there are other conjugations of a biquaternion A [Girard *et al.* (2013)]. They are the transforms of a Clifford biquaternion under an orthogonal symmetry. Figure. 2.2 shows an example of an orthogonal symmetry. Define a unit vector a as: $a = \epsilon i a_1 + \epsilon j a_2 + \epsilon k a_3$, with $aa_c = {a_1}^2 + {a_2}^2 + {a_3}^2 = 1$. For a vector $X = \epsilon i x_1 + \epsilon j x_2 + \epsilon k x_3$, by an orthogonal symmetry with respect to the hyperplane that is perpendicular to the unit vector a, the vector X can be transformed into a vector $X' = aXa$. Here $X' = \epsilon i x'_1 + \epsilon j x'_2 + \epsilon k x'_3$. Most particularly, when $a = \epsilon i$, the hyperplane perpendicular to a is the hyperplane Oyz. Therefore, from an orthogonal symmetry with respect to the

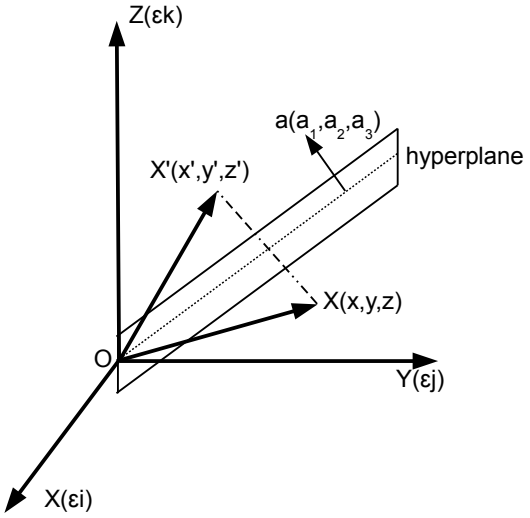

Figure 2.2: An example of orthogonal symmetry of vector X and X' with respect to a hyperplane that is perpendicular to a unit vector a [Girard *et al.* (2013)].

hyperplanes Oyz, Oxz and Oxy separately, one has the conjugations K_1, K_2 and K_3 correspondingly:

$$K_1(A) = [p_0, p_1, -p_2, -p_3] + \epsilon\,[-q_0, -q_1, q_2, q_3]\,, \tag{2.54}$$

$$K_2(A) = [p_0, -p_1, p_2, -p_3] + \epsilon\,[-q_0, q_1, -q_2, q_3]\,, \tag{2.55}$$

$$K_3(A) = [p_0, -p_1, -p_2, p_3] + \epsilon\,[-q_0, q_1, q_2, -q_3]\,. \tag{2.56}$$

Furthermore, a combination of K_1 followed by K_2 corresponds to a rotation of π around the origin:

$$K_{12}(A) = [p_0, -p_1, -p_2, p_3] + \epsilon\,[q_0, -q_1, -q_2, q_3]\,. \tag{2.57}$$

Similarly one obtains:

$$K_{13}(A) = [p_0, -p_1, p_2, -p_3] + \epsilon\,[q_0, -q_1, q_2, -q_3]\,, \tag{2.58}$$

$$K_{23}(A) = [p_0, p_1, -p_2, -p_3] + \epsilon\,[q_0, q_1, -q_2, -q_3]\,. \tag{2.59}$$

A combination of three symmetries leads to:

$$K_{123}(A) = [p_0, p_1, p_2, p_3] + \epsilon\,[-q_0, -q_1, -q_2, -q_3]\,. \tag{2.60}$$

Biquaternion analytic signal and its polar form

Given a scalar function $f(\mathbf{x})$ having its value in the Clifford algebra with $\mathbf{x} = (x, y, z)$, let $F(\mathbf{u})$ with $\mathbf{u} = (u, v, w)$ denote the CFT:

$$F(\mathbf{u}) = \int_{R^3} f(\mathbf{x}) e^{-\epsilon i 2\pi u x} e^{-\epsilon j 2\pi v y} e^{-\epsilon k 2\pi w z} dx dy dz. \tag{2.61}$$

The inverse Clifford Fourier transform (ICFT) is given by:

$$f(\mathbf{x}) = \int_{R^3} F(\mathbf{u}) e^{\epsilon k 2\pi w z} e^{\epsilon j 2\pi v y} e^{\epsilon i 2\pi u x} du dv dw, \tag{2.62}$$

it is used to calculate the $2D + t$ analytic signal.

The analytic Clifford Fourier transform is defined by:

$$F_A(\mathbf{u}) = [1 + sign\,(u)]\,[1 + sign\,(v)]\,[1 + sign\,(w)]\,F(\mathbf{u}), \tag{2.63}$$

and then the analytic signal is obtained from the ICFT:

$$f_A(\mathbf{x}) = \int_{R^3} F_A(\mathbf{u}) e^{\epsilon k 2\pi w z} e^{\epsilon j 2\pi v y} e^{\epsilon i 2\pi u x} du dv dw. \tag{2.64}$$

Due to the symmetries of the Clifford Fourier transform of a scalar function $f(x, y, z)$, only one orthant of the Fourier space is necessary to obtain the entire Fourier space.

Based on this analytic signal, a method to calculate the polar form is proposed in this section. The polar form of a $2D + t$ analytic video signal can be represented by: a scalar α, a pseudo-scalar β, and six phases φ_1, φ_2, φ_3, θ_1, θ_2, and θ_3 of a unit Clifford biquaternion a. Firstly, Eq. (2.65a) gives the polar form of the analytic signal $f_A(\mathbf{x})$ by a scalar α, a pseudo-scalar β, and a unit Clifford biquaternion a. Secondly, the unit Clifford biquaternion a is decomposed into two other unit Clifford biquaternions, which are called b and r in Eq. (2.65b). Finally, the six phases φ_1, φ_2, φ_3, θ_1, θ_2, and θ_3 of the analytic signal are obtained from b and r, which are defined in Eq. (2.65c):

$$f_A(\mathbf{x}) = (\alpha + \epsilon\beta)\, a \tag{2.65a}$$

$$= (\alpha + \epsilon\beta)\, rb \tag{2.65b}$$

$$= (\alpha + \epsilon\beta) \left(e^{i\theta_1} e^{k\theta_3} e^{j\theta_2}\right) \left\{e^{\epsilon j\varphi_2} \left[e^{\epsilon k\varphi_3} \left(e^{\epsilon i\varphi_1}\right) e^{\epsilon k\varphi_3}\right] e^{\epsilon j\varphi_2}\right\}. \tag{2.65c}$$

2.3 Application of the hypercomplex signal and the local phase to motion estimation

Over the last 20 years, various applications of hypercomplex algebras in signal and image processing have been developed. Three main motivations are discussed by Alfsmann for the application of hypercomplex signals [Alfsmann *et al.* (2007)].

- The signals are represented by a function of one or more independent parameters

such as time and location. The dimension of the algebra needs to be chosen so as to correspond to the dimension of the signal. As a consequence, each vector is processed as a whole rather than treating its components separately.

- Several applications of the hypercomplex processing of real or complex signals involve digital filtering.
- For independent signal parallel processing, the dimension of the algebra and the number of signals need to be the same.

As a mathematical tool, the work of Felsberg, Bülow and Sommer have been widely applied to signal processing and image analysis, such as motion estimation and tracking [Krause and Sommer (2005), Lee and Park (2009)], motion detection [Traversoni (2006)], and image disparity [Bülow (1999)]. In addition, the quaternion-based methods have also been applied for edge detection of color images [Sangwine and Ell (2000)]. Most of the studies are related to the research of wavelet and motion estimation.

2.3.1 Correlation of the phase of AS

As an alternative technique to the intensity correlation, various displacement measurement techniques based on spatial phase correlation have been studied [Wang *et al.* (2004), Argyriou and Vlachos (2006), Chien and Aoki (2004), Bruni *et al.* (2007), Bruni *et al.* (2009), Kumar *et al.* (2011)].

In 2004, Wang [Wang *et al.* (2004)] extracted a pseudo-phase from the analytic signal of the speckle pattern. The speckle pattern $I^{(r)}(x,y)$ is represented by a sum of the *dc* and *ac* components: $I^{(r)}(x,y) = I^{(r)}_{dc} + I^{(r)}_{ac}(x,y)$, where the superscript (r) is the real function and the Hilbert transform eliminates the dc component in this function. One can represent $I^{(r)}_{ac}(x,y)$ with an analytic signal by Hilbert filtering:

$$\tilde{I}_{ac}(x,y) = \left|\tilde{I}_{ac}(x,y)\right| e^{i\phi(x,y)}. \tag{2.66}$$

The phase $\phi(x,y)$ of the speckle pattern is defined as the pseudo-phase to differentiate it from the true phase of the optical field. $\phi(x,y)$ contains the information of the object displacement, although it is not the true phase of the input signal. From the cross-correlation of intensity of a speckle pattern on the object, the in-plane displacement is defined by:

$$\begin{aligned} C_I(\Delta x, \Delta y) &= < (I_1(x+\Delta x, y+\Delta y) - \overline{I_1(x+\Delta x, y+\Delta y)})(I_2(x,y) - \overline{I_2(x,y)}) > \\ &= < I_{1ac}(x+\Delta x, y+\Delta y) \cdot I_{2ac}(x,y) >, \end{aligned} \tag{2.67}$$

where, before and after the displacement $(\Delta x, \Delta y)$, the intensity distribution of the speckle pattern is present by I_1 and I_2, respectively. The overbar denotes the average value, and $<>$ means the averaging operation. The phase-only correlation function of the author's

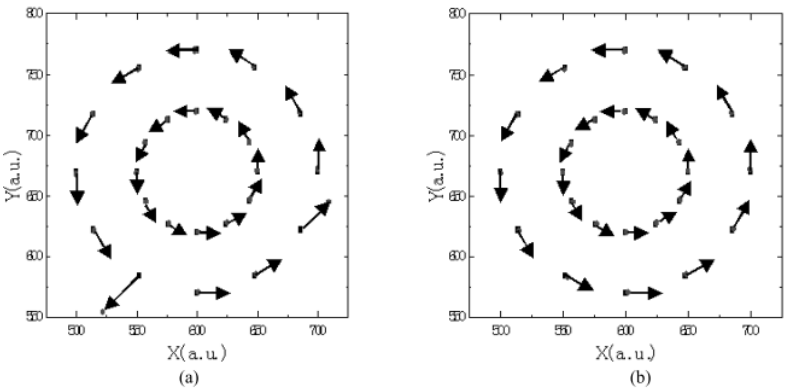

Figure 2.3: The optical flow of the in-plane displacement obtained by the conventional intensity correlation method (a), and by the SD-POC technique (b) [Wang *et al.* (2004)].

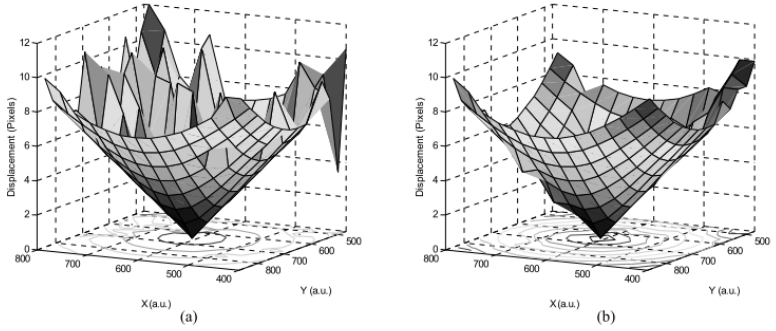

Figure 2.4: Three-dimensional view of optical flow for the rotation angle of 2°:(a) intensity correlation; (b) SD-POC [Wang *et al.* (2004)].

signal domain phase-only correlation (SD-POC) method is defined by:

$$C_P^{SD-POC}(\Delta x, \Delta y) = \left| < e^{[i\phi_1(x+\Delta x, y+\Delta y)]} e^{[-i\phi_2(x,y)]} > \right|, \tag{2.68}$$

where $\phi_1(x, y)$ and $\phi_2(x, y)$ are the pseudo-phases of the analytic signals before and after the displacement, respectively. In order to detect the local displacements, the correlations were calculated with the 15 × 15 pixel sub-window size. The results are shown in Fig. 2.3 and Fig. 2.4. Although this method is considered a simple application case, it does not indicate how this method works for other motion estimation examples.

In 2006, Argyriou and Vlachos [Argyriou and Vlachos (2006)] proposed a method for obtaining high-accuracy sub-pixel motion estimation using phase correlation. They demonstrated that, in terms of sub-pixel accuracy, their method outperforms both other surface fitting techniques and advanced phase correlation-based motion methods at that time. Their motion estimation method relies on the detection of the maximum of the cross-correlation function between two consecutive frames f_t and f_{t+1} in a motion video.

A phase correlation surface $c_{t,t+1}(x,y)$ is defined as:

$$c_{t,t+1}(x,y) = F^{-1}\left(\frac{F_t^* F_{t+1}}{|F_t^* F_{t+1}|}\right), \tag{2.69}$$

where F_t and F_{t+1} are respectively the 2D discrete Fourier transforms of f_t and f_{t+1}, F^{-1} denotes the inverse Fourier transform and $*$ denotes the complex conjugate. The coordinates (x_m, y_m) of the maximum of the real-valued array $c_{t,t+1}$ are used as the estimated horizontal and vertical motion components between f_t and f_{t+1}:

$$(x_m, y_m) = argmax Re\{c_{t,t+1}(x,y)\}. \tag{2.70}$$

In 2004, Chien [Chien and Aoki (2004)], presented a robust phase-only correlation (POC) based motion estimation method which applied on video sequences. The motion vector of a point on a video frame is changed adaptively between the motion vectors obtained by two motion estimation methods: (1) a POC-based full search and (2) a POC-based hierarchical search, which can detect both global and local motion reliably. For the POC-based full search method, one considers two image blocks of size $W \times W$ applying a Hanning window function of the same size. Since the half-width of the Hanning window function is $W/2$, the maximum reliable displacement estimate between the two image blocks is considered to be $\pm W/4$ both horizontally and vertically. For the POC-based hierarchical search method, some coarser versions of the original input images are created (coarse-to-fine correspondence search technique). *"The POC-based block matching starts at the coarsest image layer and the operation moves gradually to the finer layers. The motion vector detected at each layer is propagated to the next finer layer in order to guide the search at that layer* ([Chien and Aoki (2004)] section 3.2)." Figure 2.5 shows an overview of this technique, with an experimental result of this method in Fig. 2.6.

In 2007 and 2009, Bruni [Bruni *et al.* (2007), Bruni *et al.* (2009)] presented a novel approach for translational motion estimation based on the phase of the Fourier transform. For two successive frames, one has two aligned blocks $\{b_k(x,y)\}_{k=0,1}$ located at the same position with a translational motion:

$$b_1(x,y) = b_0(x-d_x, y-d_y), \qquad 0 \le x, y \le M-1 \tag{2.71}$$

where $M \times M$ is the block size, $b_0(x,y)$is the reference block, and (d_x, d_y) is the motion vector. Their normalized cross power spectrum is:

$$e^{j(Arg(\hat{b_0}(\omega_x,\omega_y)) - Arg(\hat{b_1}(\omega_x,\omega_y)))} = \frac{\hat{b_0}(\omega_x,\omega_y)\hat{b_1^*}(\omega_x,\omega_y)}{\left|\hat{b_0}(\omega_x,\omega_y)\hat{b_1^*}(\omega_x,\omega_y)\right|}, \tag{2.72}$$

where $\hat{\cdot}$, $Arg(,\cdot)$ and $\cdot*$, respectively, indicate the FFT, the phase, and the complex conjugation of $\cdot$. The inverse FFT of the $e^{j(Arg(\hat{b_0}(\omega_x,\omega_y)) - Arg(\hat{b_1}(\omega_x,\omega_y)))}$ part makes it possible to achieve the phase correlation surface that contains a peak $\delta(x-d_x, y-d_y)$ that corresponds

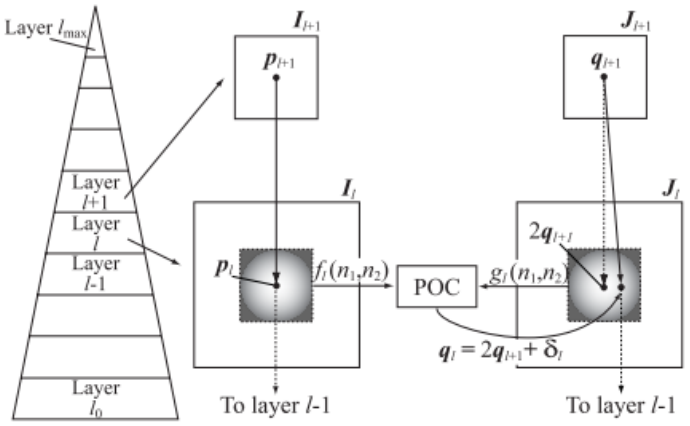

Figure 2.5: Block matching using a hierarchical coarse-to-fine approach [Chien and Aoki (2004)].

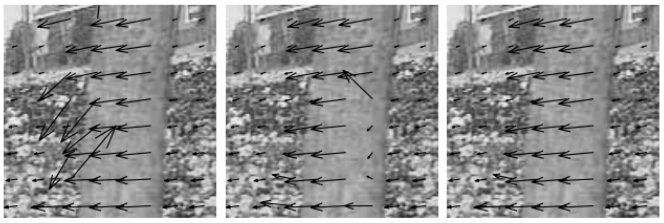

(a) (b) (c)

Figure 2.6: Motion estimation for Flower Garden using (a) the POC-based full search motion estimation method; (b) the POC-based hierarchical search motion estimation method; and (c) the POC-based adaptive search motion estimation method [Chien and Aoki (2004)].

to the displacement (d_x, d_y). Then it was proved that the average B of K aligned blocks subjected to a translational motion is equivalent to the convolution of the reference block b_0 with a suitable function δ_{comb}. Here:

$$B(x,y) = \frac{1}{K}\sum_{k=0}^{K-1} b_k(x,y). \qquad 0 \le x, y \le M-1 \tag{2.73}$$

K is the number of blocks and:

$$\delta_{comb}(x,y) = \frac{1}{K}(x - kd_x, y - kd_y). \tag{2.74}$$

Noting that the conventional phase correlation technique can only be applied to grayscale images, Sangwine et al. [Sangwine *et al.* (2001)] firstly proposed a quaternionic phase correlation technique, and later, Reddy [Reddy and Talari (2011)] introduced an extension of the phase correlation technique to the quaternion field based on quaternion Fourier transforms. The definition of a quaternion cross-correlation of two images $f(x,y)$ and $g(x,y)$

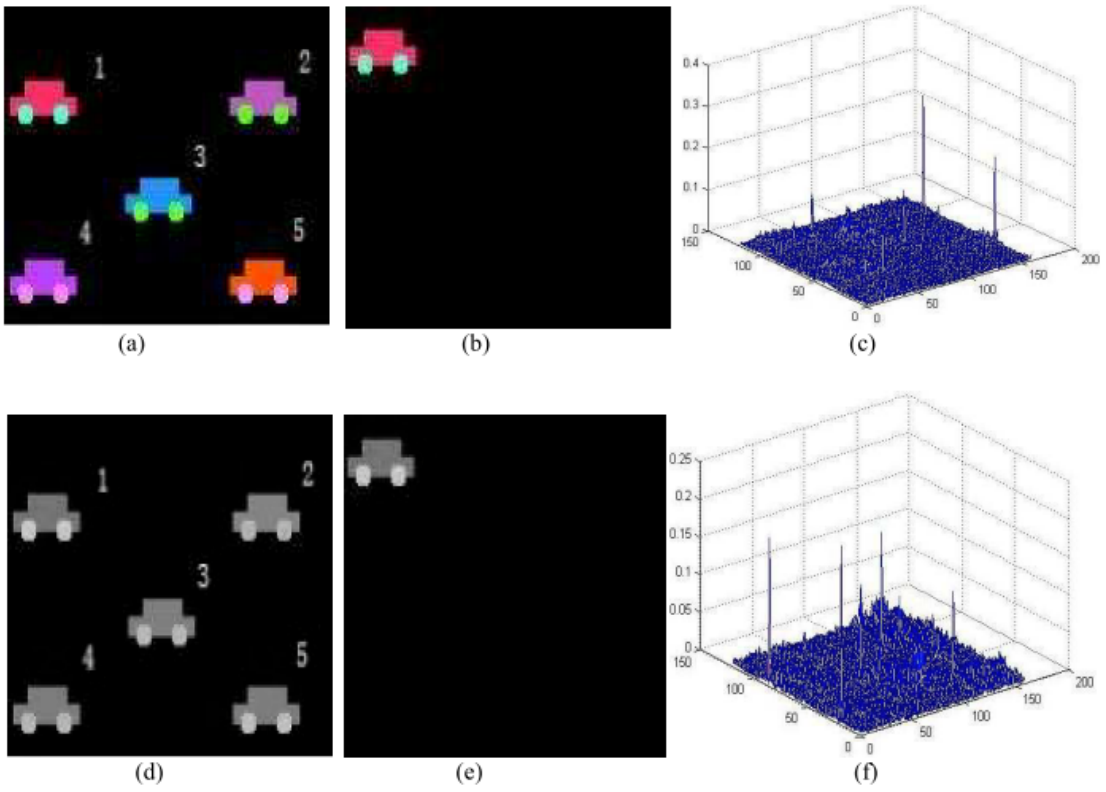

Figure 2.7: Color template matching in synthetic images (a) the input color image; (b) the color template; (c) the phase correlation surface using quaternion phase correlation; (d) and (e) the input images with grayscale information; (f) the phase correlation surface using conventional phase correlation [Reddy and Talari (2011)].

is:

$$c(m,n) = \sum_{p=0}^{M-1} \sum_{q=0}^{N-1} f(p,q)\overline{g(p-m,q-n)}, \tag{2.75}$$

where the shift operation on $g(x,y)$ is implemented cyclically using modular arithmetic [Moxey *et al.* (2003)]. $c(m,n)$ is the correlation function of the images. If the images $f(x,y)$ and $g(x,y)$ are the same images the autocorrelation of the images is computed. *"If the mean, or DC level of each image is subtracted first, the cross-covariance is obtained. Direct evaluation of the cross-correlation function is impractical for all but the smallest images due to the high computational cost* ([Reddy and Talari (2011)] section 5.1)." The artificial car shown in Fig. 2.7(b) is the color template. Figure. 2.7(a) is the input color image to be searched for the true match area. There are five candidate cars in the true input image that are the same shape and size but different colors. Only the candidate car marked 1 is the true match of the template. Following our quaternion phase correlation-based matching algorithm, the phase correlation surface is obtained as shown in Fig. 2.7(c). From this figure, it can be observed that only one outstanding peak exists, which corresponds to the true match area.

2.3.2 Optical flow by monogenic phase

In 2007, Zang adapted the combined local and global (CLG) optical flow estimation approach to estimate two-frame dense optical flow from the monogenic curvature tensor [Zang *et al.* (2007)]. Then in 2009, Demarcq estimated flows on local color phase based on the color monogenic signal associated with a color image [Demarcq *et al.* (2009)]. Both of these studies are based on the CLG approach and focus on the 2D signal. In Zang's method, there is an assuming that the image gray values $f(x, y, t)$ in subsequent frames do not change over time. One has:

$$f(x + u, y + v, t + 1) = f(x, y, t), \tag{2.76}$$

where the displacement field $[u, v]^T$ denotes the optical flow. Following this, the spatial CLG method minimizes an energy function in order to estimate the flow field:

$$E(\mathbf{w}) = \int_{\Omega} (\psi_1(\mathbf{w}^T J_\rho(\nabla_3 f)\mathbf{w}) + \alpha\psi_2 |\nabla\mathbf{w}|^2))dxdy, \tag{2.77}$$

with

$$\begin{aligned}
\nabla &= [\partial_x, \partial_y]^T, \\
\nabla_3 &:= [\partial_x, \partial_y, \partial_t]^T, \\
\mathbf{w} &:= [u, v, 1]^T, \\
|\nabla\mathbf{w}|^2 &:= |\nabla u|^2 + |\nabla v|^2, \\
J_\rho(\nabla_3 f) &:= K_\rho \star (\nabla_3 f \nabla_3 f^T),
\end{aligned}$$

where Ω denotes the image domain, α is a regularization parameter, K_ρ means a Gaussian kernel with standard deviation ρ, $\psi_1(\cdot)$ and $\psi_2(\cdot)$ indicate two nonquadratic penalizers with the following form:

$$\psi_i(z) = 2\beta_i^2\sqrt{1 + \frac{z}{\beta_i^2}}, \quad i \in \{1, 2\} \tag{2.78}$$

where β_1 and β_2 are scaling parameters to handle the outliers.

Later, in 2011, Demarcq extended his work to the 3D signal using the CLG approach for color optical flow estimation [Demarcq *et al.* (2011)]. He described this construction in a more general framework of mappings:

$$f(p) = f_3(p)e_3 + f_4(p)e_4 + f_5(p)e_5, \tag{2.79}$$

from $\mathbb{R}^2$ with values in the vectorial part of the Clifford algebra $\mathbb{R}_{5,0}$, which is shown in Fig. 2.8.

The color monogenic signal is then used to represent a polar form of a color image as

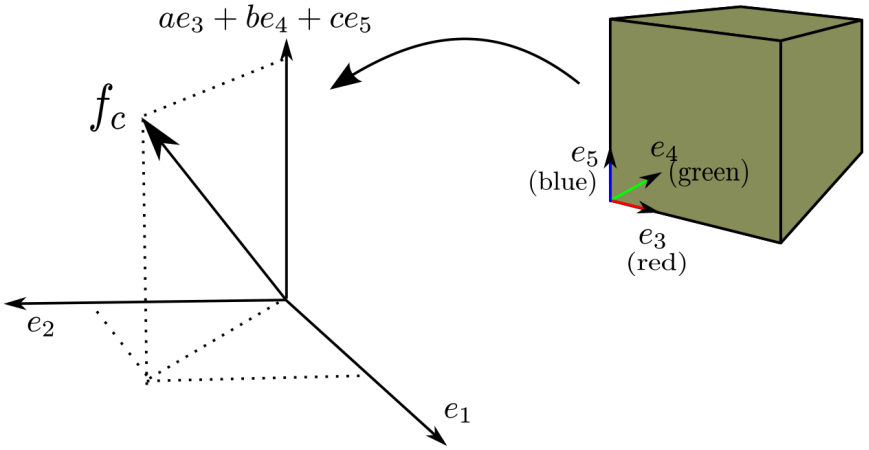

Figure 2.8: The Color Monogenic Signal representation in $\mathbb{R}_{5,0}$. Decomposition in the RGB space (right), then in $\mathbb{R}_{5,0}$ (left) [Demarcq *et al.* (2011)].

a map from $\mathbb{R}^5$ with values in the versor space of $\mathbb{R}_{5,0}$, which is given by:

$$A_v(x,y,t)e^{i\varphi_v(x,y,t)}. \tag{2.80}$$

The energy to be minimized is given by:

$$E(\mathbf{w}) = \int_\Omega (\mathbf{w}^T J_\rho(\nabla_3 f)\mathbf{w}) + \alpha\,|\nabla_3 \mathbf{w}|^2))dxdydt, \tag{2.81}$$

with

$$(P)\begin{cases} \mathbf{w} := [u,v,1]^T, \\ |\nabla_3 \mathbf{w}|^2 = |\nabla_3 u|^2 + |\nabla_3 v|^2, \\ \nabla_3 f = (f_x, f_y, f_t)^T, \\ \mathbf{w}^T J_\rho(\nabla_3 f) = K_p \times (\nabla_3 f \nabla_3 f^T). \end{cases}$$

Replacing the intensity function f with φ_v leads to the following energy:

$$E(\mathbf{w}) = \int_\Omega (\mathbf{w}^T J_\rho(\nabla_3 \varphi_v)\mathbf{w}) + \alpha\,|\nabla_3 \mathbf{w}|^2))dxdydt. \tag{2.82}$$

Figure 2.9 shows an example of a color video of moving plants in a fish tank, with the aim of extracting the optical flow of the red leaves. The motion of the plants is caused by the motion of the water. Because of the strong illumination change in this example, the Horn-Schunck method result is very poor. However, the polar representation of the color optical flow obtained is presented in the second row, right, which is accurate and robust against illumination changes.

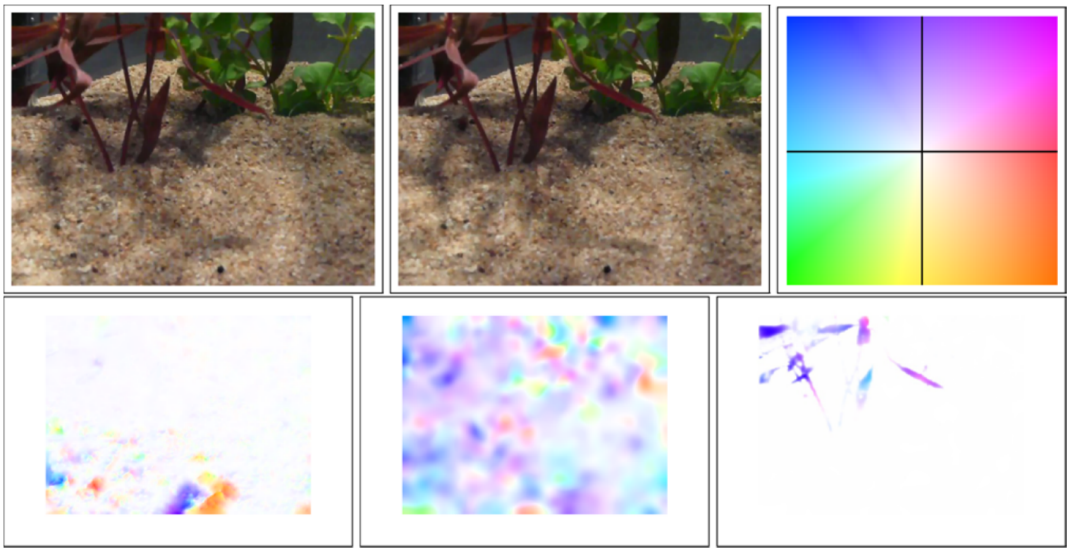

Figure 2.9: From left to right. First row: two frames from the fish tank plant sequence, flow coding pattern. Second row: Horn-Schunck result, CLG result, and the Demarcq color optical flow method result with the prescribed color set to red [Demarcq *et al.* (2011)].

2.4 Application to myocardium motion estimation

In 1999, Osman [Osman *et al.* (1999)] showed that: from the inverse Fourier transform of a spectral peak, one obtains a complex angle called a harmonic phase (HARP) image, which was used for rapid analysis of tagged cardiac magnetic resonance image sequences. Brotman improved this method in 2013 for the motion on left ventricular rotation using a slice following harmonic phase imaging [Brotman *et al.* (2013)]. The HARP imaging method makes use of a bandpass filter to isolate the k-th spectral peak centered at frequency ω_k, which is the lowest harmonic frequency in a certain tag direction. Then, a complex harmonic image is obtained from the inverse Fourier transform of the bandpass region. A circle drawn in Fig. 2.10(b) represents the -3 dB isocontour of the bandpass filter, which is used to process the data. Because the harmonic phase cannot be directly calculated when considering the application of HARP tracking, the value of the HARP angle is used in the computations. As the result, there are many points in the image plane corresponding to the same pair of HARP angles. For a point with two HARP angles, only one of them sharing the same HARP angles in the later image is the correct match. It is to say that it shares as well the same pair of harmonic phases. If there is a small motion between two successive images, it could be the nearest of these points considered as the correct point. That is strategy of the HARP tracking on an apparent motion through a cine sequence of tagged MR images.

Another excellent study on cardiac tagged MR images was conducted by Arts in 2010 for the displacement estimation at subpixel accuracy, which is called the SinMod method [Arts *et al.* (2010)]. In this study, the displacement is estimated more accurately with the SinMod method than the HARP method. The basic idea is that a summation

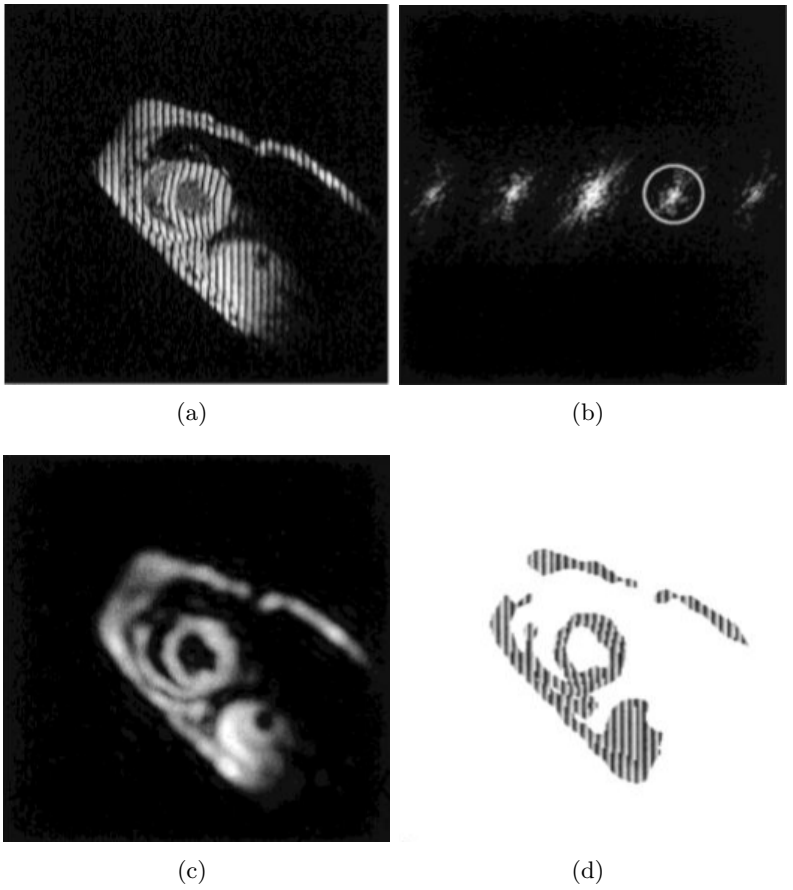

Figure 2.10: (a) An MR image with vertical spatial modulation of magnetization (SPAMM) tags. (b) The magnitude of its Fourier transform. By extracting the spectral peak inside the circle in (b), a complex image is produced with a magnitude (c) and a phase (d). [Osman *et al.* (1999)]

of sine wave fronts is used to model the pixel intensity. It has a local relation with the motion of myocardial tissue. In addition, the sine-wave components are selected by 2D bandpass filters.

Given planar coordinates p and q in Fig. 2.11, two successive images, I_1 and I_2, the intensity of a local region around a pixel $[p, q]$ is modeled as a cosine wavefront, which has a displacement u along the p-direction:

$$\begin{aligned} I_1(p,q) &= A_1 cos\left(\omega_p(p+\tfrac{u}{2})+\varphi\right)+n_1(p,q), \\ I_2(p,q) &= A_2 cos\left(\omega_p(p-\tfrac{u}{2})+\varphi\right)+n_2(p,q), \end{aligned} \tag{2.83}$$

where ω_p is the spatial frequency, φ is the phase and A_1, A_2 are the amplitudes of the wave; n_1 and n_2 are the independent noise images.

The main idea of this work is the following. From the cosine wavefront model, a bandpass filter is employed to remove the noise images. Then a complex cross-power image is calculated from the first image and the complex conjugates of the second image. In the

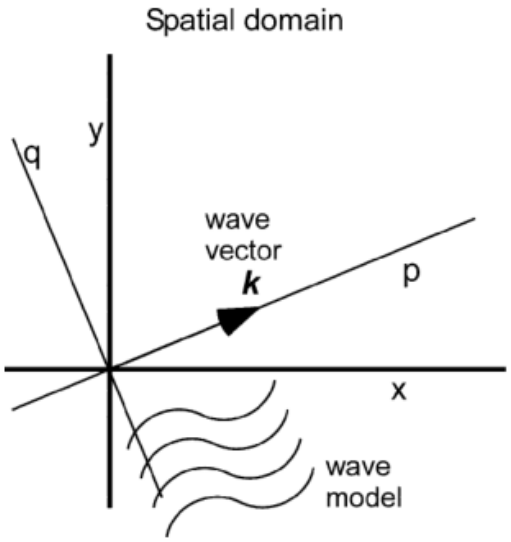

Figure 2.11: Sine wave with wavefronts parallel to the q-axis propagates along the p-axis. Wave vector k points in the direction of propagation, with a length equal to the wavelength. The x and y coordinates represent image coordinates. [Arts *et al.* (2010)]

phase of the complex cross-power image, the terms p and φ in Eq. (2.83) are eliminated and hence the displacement u is obtained. For the low-level noise sequence, the SinMod and HARP methods have similar performance. However, the SinMod method provides a better result on suppressing the effects of image noise, aliasing artifacts, and aberrations in grid orientation.

In 2012 Xavier also used the phase-based optical flow method for cardiac wall motion from cine MRI sequences [Xavier *et al.* (2012)]. She developed a modified version of the phase-based optical flow algorithm (MPOF) using the spatial filtering introduced by Bruno and Pellerin [Bruno and Pellerin (2002)]. The MPOF method uses a complex 2D spatial Gabor filtering for estimating optical flow with a temporal second-order differentiation. It uses a complex 2D Gabor filter bank made of N filters. Each filter corresponds to a pair of opposed 2D Gaussians oriented at an angle θ_i, and whose impulse response $g_i(x, y)$ at the i-th filter is:

$$g_i(x,y) = \frac{1}{2\pi\sigma^2} e^{-(x^2+y^2)/2\sigma^2} \times e^{j2\pi f_0(xcos\theta_i + ysin\theta_i)}, \tag{2.84}$$

where f_0 and σ are, respectively, the central frequency and the standard deviation of the Gaussian envelope of the filter.

The angular error (AE) in Xavier's work is used to evaluate optical flow performance:

$$AE = arccos\left(\frac{u_e u_c + v_e v_c + 1}{\sqrt{u_e^2 + v_e^2 + 1}\sqrt{u_c^2 + v_c^2 + 1}}\right), \tag{2.85}$$

with (u_c, v_c) the correct velocity and (u_e, v_e) the estimated velocity. Then she used the

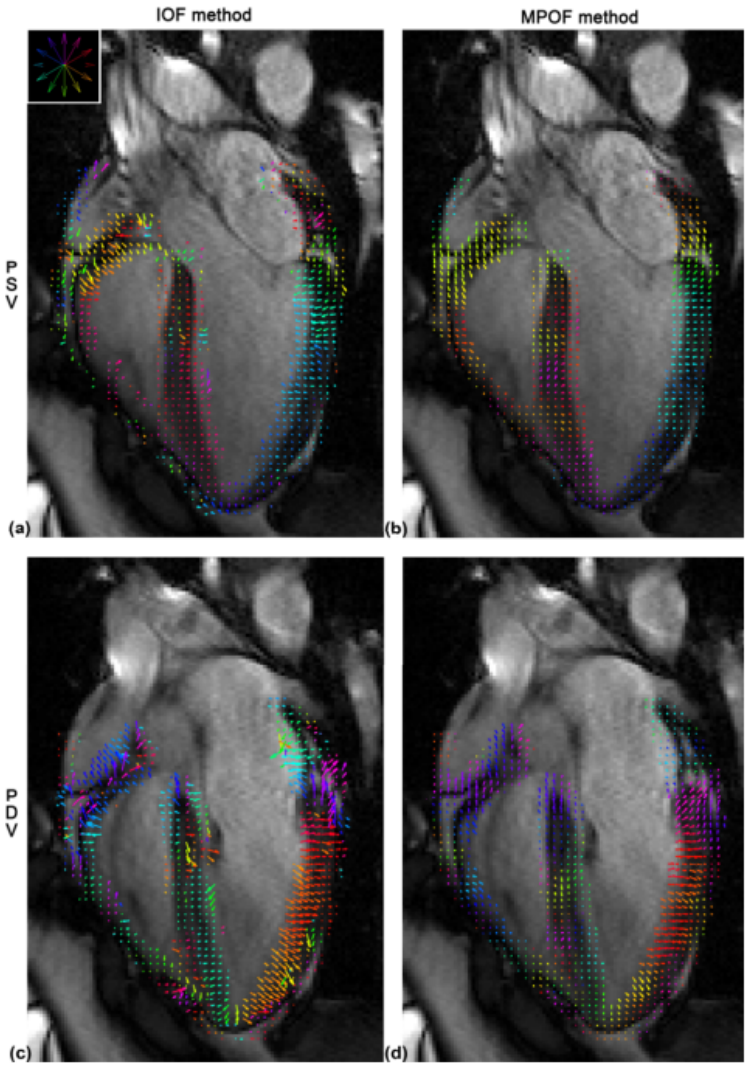

Figure 2.12: OF estimates on the four-chamber MRI sequence for the first normal heart at PSV (on the first row) and PDV (on the second row) using either the IOF on the left (with the constraint on gradient magnitude set to $||\Delta||>=1$) or the MPOF method on the right. The OF visualization was restricted to the myocardium area. A mask was applied to display the vector field only at the level of the myocardium. [Xavier *et al.* (2012)]

Horn-Schunck intensity-based optical flow method (IOF) and the MPOF techniques to test a simulated cardiac MRI sequence of healthy heart on the long-axis and short-axis orientations, which are shown in Fig. 2.12 and Fig. 2.13.

On the B-mode echocardiographic cardiac images, a new optical-flow-based method was proposed by Sühling [Sühling *et al.* (2005)]. The method uses a local-affine model for the spatial velocity computation and also a linear model in time, which allow to process the complex myocardium motion (rotation, contraction/expansion and shear). Given

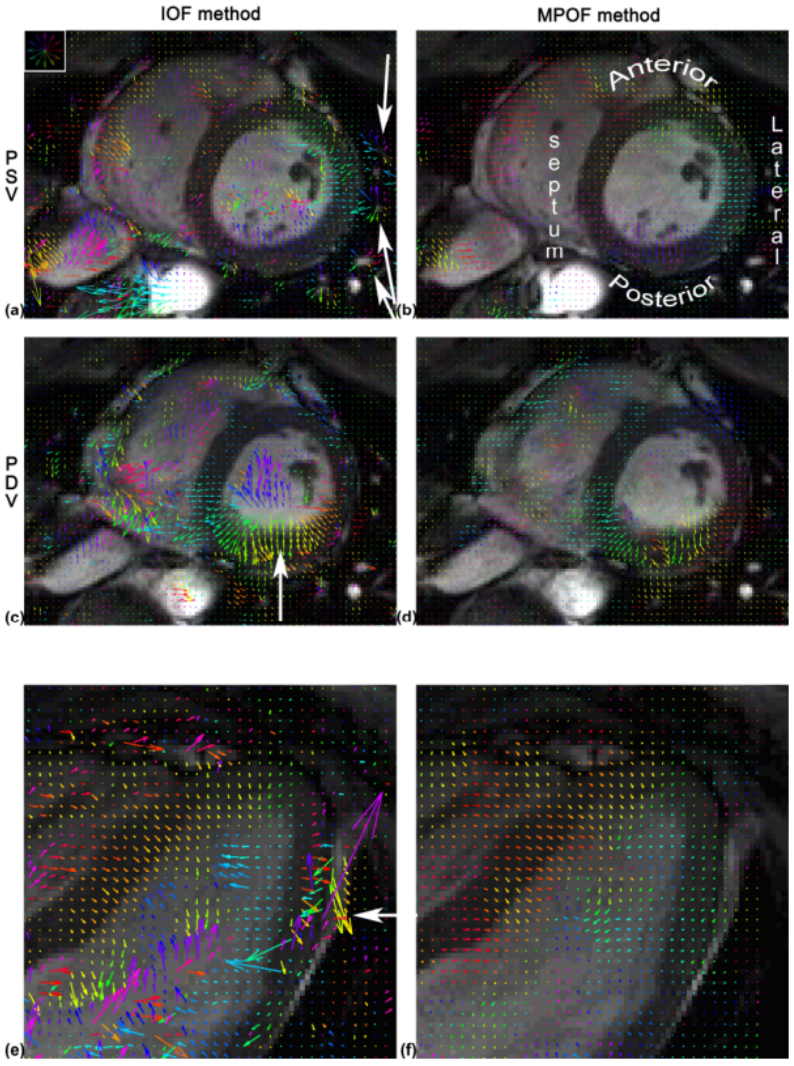

Figure 2.13: OF estimates on the short-axis MRI sequence for the first normal heart (a–d) and on the long-axis orientation for the second normal heart (e, f). For the first sequence, motion is displayed at (a, b) PSV and (c, d) PDV. For the second sequence, motion is depicted during early systole. Two OF techniques are used, the IOF on the left (with the constraint on gradient magnitude set to $||\Delta||>=1$) and the MPOF method on the right. Considering the IOF technique, the white arrows depict (a) motion singularities due to blood inflow through vessels; (c) overestimated movement due to important through-plane motion; and (e) poorer results due to the through-plane incoming of fat tissues. [Xavier *et al.* (2012)]

(x_0, y_0, t_0) the center of a small image region, the local-affine model is defined as:

$$\begin{pmatrix} u(x,y,t) \\ v(x,y,t) \end{pmatrix} = \begin{pmatrix} u_0 \\ v_0 \end{pmatrix} + \begin{pmatrix} u_x & u_y & u_t \\ v_x & v_y & v_t \end{pmatrix} \begin{pmatrix} x - x_0 \\ y - y_0 \\ t - t_0 \end{pmatrix}, \tag{2.86}$$

where (u_0, v_0) is the velocity of the center point (x_0, y_0, t_0), with u_x, u_y, v_x, v_y, the first-

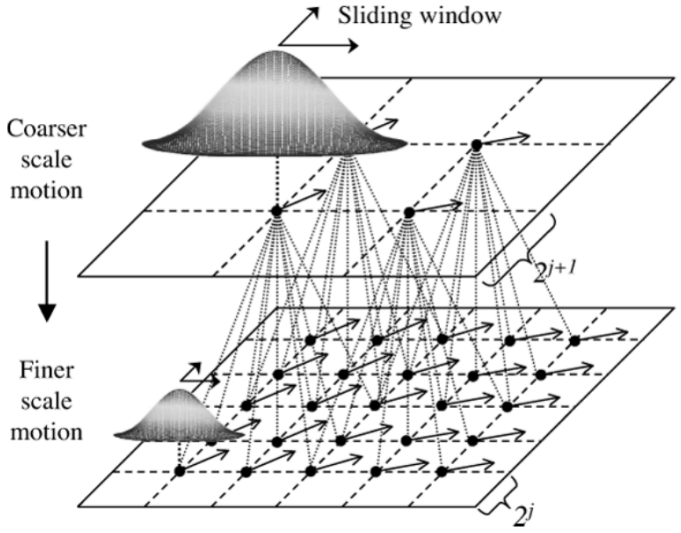

Figure 2.14: Coarse-to-fine multiscale strategy in space. [Sühling *et al.* (2005)]

order spatial derivatives of u and v; u_t, v_t the first-order temporal derivatives of u and v, respectively. The parameters of regional motion are estimated inside a spatiotemporal B-spline window. A wavelet-like algorithm is employed to compute B-spline-weighted inner products and moments at dyadic scales, which enable to increase the computational efficiency. In addition, in order to solve the problem of large motion estimation accuracy, a coarse-to-fine strategy is proposed, illustrated in Fig. 2.14. This method is validated on the realistic motion fields yielded from clinical echocardiograms and then applied to clinical data.

Sühling's echocardiographic-cardiac-images-oriented method was adopted by Alessandrini in 2013 [Alessandrini *et al.* (2013)], which works well on both of the cardiac echocardiographic and tagged MR images. Different from Sühling's method, Felsberg's monogenic phase is used in Alessandrini's method. Based on a conservation assumption of the monogenic phase over time, the displacement is computed locally. In order to adapt myocardial motion, a local affine displacement model is used to replace the previous Felsberg's pure translation model. As a local optical flow method, Alessandrini proposed a full automatic image windows size selection, which avoids the problem of choosing an inadequate image window size when computing the regional motion parameters inside the spatiotemporal B-spline window.

The method was evaluated on simulated tagged MR sequences, which are generated by the software ASSESS [Clarysse *et al.* (2011)]. The performance of Alessandrini's method has been proved to be better than the SinMod method and Zang's method (monogenic curvature tensor-based method) [Zang *et al.* (2007)]. Figure 2.15 shows the error map of motion vectors on one frame from two synthetic tagged MR sequences: a rotation sequence "R20F20" and a contraction/expansion sequence "D30F20." In addition, the evaluation was carried out on echocardiographic sequences. Hence, this method is declared to be a valid alternative to state-of-the-art techniques with more accurate results than the other

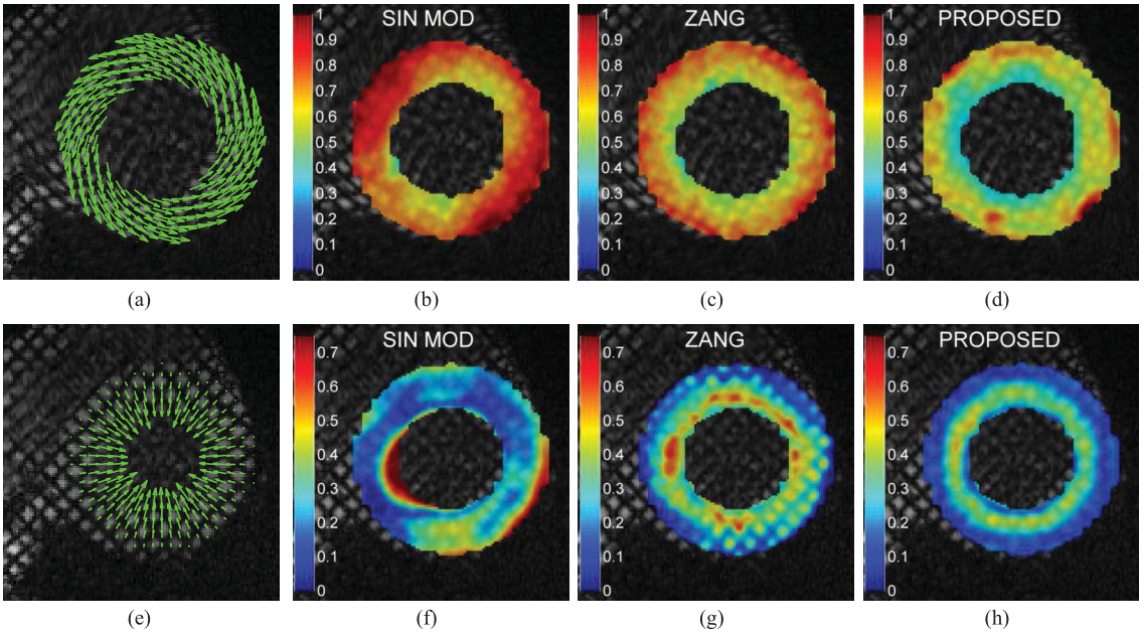

Figure 2.15: Error map of three method on one frame from two sequences. (a)–(d) R20F20; (e)–(h) D30F20. The green arrows in (a) and (e) denote the benchmark field. [Alessandrini *et al.* (2013)]

monogenic signal based methods.

2.5 Conclusion

In this chapter, two types of study were reviewed: (1) the complex and hypercomplex signals in 1D and nD and (2) the motion estimation studies for myocardium in medical images. The connection of these two components is the application of phase information on medical images that are used for motion estimation instead of the application to the widely used intensity information of the images. Moreover, since most applications are based on the 2D complex/hypercomplex signal, little research is available that shows possible extension applications to 3D or nD data processing.

As a result, we focused on the solution to the following problems: (1) which type of complex/hypercomplex analytic signal has suitable phase information for our application and more importantly, which algebra could be chosen to extend the complex/hypercomplex analytic signal to a higher dimension with the potential for application of nD data processing? (2) Is it possible to obtain a more accurate myocardial motion estimation result from the phase-based method such as the SinMod method and Alessandrini's monogenic phase method?

As to the first problem, we note that Hahn used the complex 2D Hahn single-quadrant AS to construct the hypercomplex 2D QS represented by Clifford algebra. From this idea, using the complex 3D Hahn AS, we were able to construct a 3D hypercomplex analytic signal in the framework of Clifford algebra. This work is presented in chapter 3. A new

definition of the hypercomplex analytic signal is given by 3D Clifford algebra based on 3D Hahn AS.

For the second problem, we propose a new myocardial motion analysis method based on the phases of 2D Hahn AS. We show that the phases of 2D Hahn AS have an outstanding ability for accurate motion detection on the cardiac tagged MR image, without any multiscale strategy, as observed in Sühling and Alessandrini's work. The details of the method and experimental results are presented in chapter 4 and chapter 5, respectively.

III Contribution

Chapter 3

2D and 3D Clifford analytic signals from Hahn single-orthant analytic signals

New algebraic structures have been developed during the past few decades [Vince (2008)]. Based on Clifford algebras and quaternions, many new complex analytic signals have also been defined [Sangwine and Le Bihan (2007), Hahn and Snopek (2011), Unser *et al.* (2009), Said *et al.* (2008)]. As a useful mathematical tool, the analytical signal (AS) enables one to extract local features from images. Based on this tool, many applications have been proposed for signal processing and image analysis. For example, motion detection [Krause and Sommer (2005), Lee and Park (2009)], image disparity estimation [Witten and Shragge (2006), Bülow (1999)] and edge detection of a color image [Sangwine and Ell (2000)]. For the application of an analytic signal to a medical image, Woo [Woo *et al.* (2009)] and Lee [Lee *et al.* (2011)] used the 2D local phase and the intensity of the ultrasound image for registration. Another registration approach for 3D ultrasound image was also introduced by Zhang [Zhang *et al.* (2006)], based on phase information. Furthermore, Harput et al. [Harput *et al.* (2011)] used the ultrasound phase image to measure the enamel thickness of the human tooth, and Maltaverne et al. [Maltaverne *et al.* (2010)] extracted the phase from the monogenic signal of the ultrasound image to estimate subpixel motion. Both of them proved that their phase-based methods produced more accurate results.

Since we know that identity split is one of the properties of the analytic signal, i.e., the information of a signal can be separated into the local phase and the local amplitude. Moreover, the partial angles and partial moduli of the hypercomplex signal are introduced

in [Bayro-Corrochano (2006)]. However, most of the research cited above applies phase information, but the local amplitude information or partial modulus of the analytical signal have not been widely used. On the other hand, medical ultrasound data are often presented as 3D spatial volumes or 4D spatial-temporal volumes (3D volume variation in time). Since most of the previous studies focused on only one or two dimensions of the volume data separately [Wachinger *et al.* (2011)], they may contribute to a loss of information owing to processing the dimensions separately. Hence, multidimensional data processing of the whole medical volume is required to obtain more accurate results.

As a result, based on Clifford biquaternion algebra, we conducted several preliminary studies on the 2D+t analytical signal [Wang *et al.* (2012)a, Wang *et al.* (2012)c] and its application to 3D ultrasound pseudo-envelope detection [Wang *et al.* (2012)b]. In this chapter, focusing on the extension of the 2D quaternion signal (QS), we propose a 3D hypercomplex analytic signal within the framework of Clifford algebra. From the proposed 3D hypercomplex analytic signal, we present an envelope detection result for a 3D radio frequency (RF) ultrasound volume.

Considering the conception of the Hilbert transform, we first reviewed the 1D classic AS that can be obtained by the 1D Hilbert transformation. Then we illustrated the elements of 2D QS that are also constituted by 2D Hilbert transformation. Next, we proposed the 3D Clifford analytic signal (CAS) in its biquaternion form and the calculation of this 3D CAS by 3D Hilbert transform. All these types of analytic signals result from different combinations of the original signal and its partial and total Hilbert transforms. In each section, we presented the details of how these analytic signals can be calculated from the partial and total Hilbert transforms. Finally, an application of the 3D CAS for RF ultrasound envelope detection was shown.

Before going to the 2D and 3D Clifford analytic signal, let us recall the 1D Hilbert transform and the 1D classical analytic signal to give an explanation of the analytic signal.

3.1 Hilbert transform and Gabor's 1D analytic signal

3.1.1 Hilbert transform

The Hilbert transform was introduced by a German mathematician David Hilbert in his works of the early 20th century and is widely used for signal processing [Hahn (1996)]. For a 1D real signal $f(t)$ varying with time, the definition of the 1D Hilbert transform is given by:

$$H\{f(t)\} = f(t) \star \frac{1}{\pi t}, \tag{3.1}$$

where $\star$ denotes the 1D convolution operation. Since the term $\frac{1}{\pi t}$ introduces a singularity in the integral of convolution, the Hilbert transform is defined using the Cauchy principal

value (P.V.) of the integral:

$$\begin{aligned} H\{f(t)\} &= \frac{1}{\pi} P.V. \int_{\mathbb{R}} \frac{f(\tau)}{t-\tau} d\tau \\ &= \frac{1}{\pi} \lim_{\epsilon \to 0} \left(\int_{-\infty}^{t-\epsilon} \frac{f(\tau)}{t-\tau} d\tau + \int_{t+\epsilon}^{\infty} \frac{f(\tau)}{t-\tau} d\tau \right). \end{aligned} \tag{3.2}$$

From the Fourier transformation of $\frac{1}{\pi t}$:

$$F\left\{\frac{1}{\pi t}\right\} = -i' sign(u), \quad \text{with } sign(u) = \begin{cases} 1 & \text{if } u > 0 \\ 0 & \text{if } u = 0 \\ -1 & \text{if } u < 0 \end{cases}, \tag{3.3}$$

the Hilbert transform in the frequency domain is defined as:

$$F\left\{f(t) \star \frac{1}{\pi t}\right\} = F\left\{H\{f(t)\}\right\} = F(u) \cdot (-i' sign(u)) = F_H(u), \tag{3.4}$$

where i' is the imaginary unit, $F_H(u)$ and $F(u)$ are the Fourier transform of $H\{f(t)\}$ and $f(t)$, respectively. Hence, the modulus $|F_H(u)|$ and phase $Arg[F_H(u)]$ of $F_H(u)$ are:

$$|F_H(u)| = |F(u)|, \tag{3.5}$$

$$Arg[F_H(u)] = Arg[F(u)] - \frac{\pi}{2} sign(u). \tag{3.6}$$

The Hilbert transform is usually used to shift by $-\frac{\pi}{2}$ the phase of a signal. In other words, calculating the Hilbert transform of a signal is equivalent to shifting the phase by $-\frac{\pi}{2}$. For example, given a signal $f(t) = cos(x)$,

- Hilbert transform of $f(t)$:$H\{f(t)\} = \frac{1}{\pi} P.V. \int_{\mathbb{R}} \frac{cos(\tau)}{t-\tau} d\tau = sin(t)$.
- Shift the signal phase by $-\frac{\pi}{2}$: $f\left(t - \frac{\pi}{2}\right) = cos\left(t - \frac{\pi}{2}\right) = sin(t)$.

This property is satisfied by a general signal $f(x)$ since any signal can be decomposed into a mixture of cosine functions.

3.1.2 Gabor's 1D analytic signal

Based on the Hilbert transform, Gabor defined firstly the analytic signal of a 1D real signal [Gabor (1946)]. An AS $\psi(t)$ of a real signal $f(t)$ contains two parts: a real part (the real signal itself) and an imaginary part (Hilbert transform of $f(t)$), which can be written as:

$$\psi(t) = f(t) + i' H\{f(t)\} = f(t) \star \left(\delta(t) + \frac{i'}{\pi t}\right), \tag{3.7}$$

where i' is the imaginary unit. In the frequency domain, the AS is given by:

$$\Psi(u) = F(u) + i'F_H(u) = F(u)(1 + sign(u)) = \begin{cases} 0 & \text{if } u < 0 \\ F(0) & \text{if } u = 0 \\ 2F(u) & \text{if } u > 0 \end{cases}. \tag{3.8}$$

In addition, the AS of $\psi(t)$ enables us to calculate the instantaneous amplitude and instantaneous phase of $f(t)$, which are defined by:

$$\text{instantaneous amplitude: } a_1(t) = |\psi(t)|, \tag{3.9}$$

$$\text{instantaneous phase: } \varphi_1(t) = Arg[\psi(t)]. \tag{3.10}$$

An example of a cosine signal (dashed line) is shown in Fig. 3.1. The instantaneous amplitude of this cosine signal is its envelope which is presented by the dash-dot line, with a constant value of 10 along the time. The instantaneous phase is presented by the solid line, and its range is $[-\pi, \pi]$. During each period of the cosine signal, when it arrives at the minimum value, the phase is π and then it jumps to $-\pi$ when the signal begins to increase.

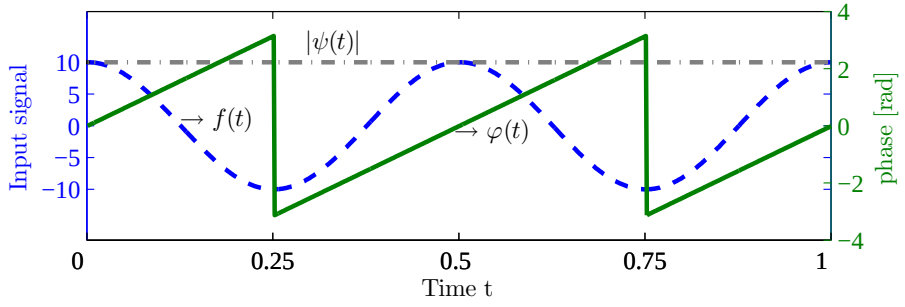

Figure 3.1: An example of cosine signal (blue dashed line) with its time-invariant instantaneous amplitude of 10 (gray dash-dot line) and instantaneous phase (green solid line). The phase is limited to $[-\pi, \pi]$ with a phase jump at the minimum value of each period of the input cosine signal.

In addition, a complex valued signal, $\psi(t)$ can be considered as a vector that rotates in the complex plane. The projection of this vector to the real axis is the original real signal f, and the projection to the imaginary axis is the Hilbert transform of the original signal f. Furthermore, at a given time t_0, the length of the vector is the instantaneous amplitude of f, and the angle between this vector and the real axis gives the instantaneous phase of f. Fig. 3.2 shows an example of these definitions as below.

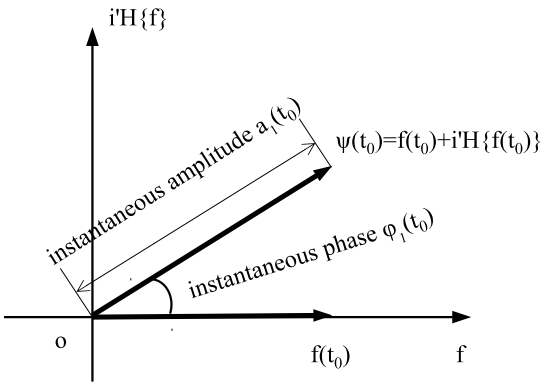

Figure 3.2: The analytic signal of $\psi(t)$ of $f(t)$ at a given time t_0 with the instantaneous amplitude and phase. $\psi(t)$ can be consider as a rotating vector in the complex plane.

3.2 2D single-quadrant complex signals

In this chapter, we refer to 2D complex signals with single-quadrant spectra as 2D Hahn AS for short. On one hand, the 2D Hahn AS can be obtained by 2D complex Fourier transformation by taking one quadrant information in its frequency spectrum. On the other hand, another direct method to obtain the 2D Hahn AS is using the Hilbert transform of the original signal. Furthermore, 2D partial and total Hilbert transforms of the original signal can be used to present the relation of the 2D Hahn AS and 2D QS.

For a 2D real signal $f(x, y)$, the 2D Hahn AS are:

$$\begin{aligned}
\psi_1(x,y) &= F^{-1}\left[(1+s_1)(1+s_2)F(u,v)\right] \\
&= (f - H\{f\}) + i'\left(H_x\{f\} + H_y\{f\}\right) \\
&= a_1 e^{i'\varphi_1} = a_1\cos\varphi_1 + i' a_1 \sin\varphi_1, \qquad (3.11)\\
\psi_3(x,y) &= F^{-1}\left[(1+s_1)(1-s_2)F(u,v)\right] \\
&= (f + H\{f\}) + i'\left(H_x\{f\} - H_y\{f\}\right) \\
&= a_3 e^{i'\varphi_3} = a_3\cos\varphi_3 + i' a_3 \sin\varphi_3, \qquad (3.12)
\end{aligned}$$

where i' is the usual complex imaginary, $H\{f\}$ is the total Hilbert transform. $H_x\{f\}$ and $H_y\{f\}$ are the partial Hilbert transform computed in x or y directions. a_1 and φ_1 are the modulus and the phase of $\psi_1(x, y)$, respectively, and a_3 and φ_3 are the modulus and the phase of $\psi_3(x, y)$, respectively.

The 2D Hahn AS in Eqs. (3.11) and (3.12) are computed by the single-quadrant operators: $(1 + s_1)(1 + s_2)$ and $(1 + s_1)(1 - s_2)$, with $s_1 = sign(u)$, $s_2 = sign(v)$. Figure 3.3 shows the two corresponding quadrants from the single-quadrant operators.

Based on the 2D Hahn AS, we want to find the relation between the modulus/phase and the Hilbert transforms of the signal for further study. From Eqs. (3.11) and (3.12),

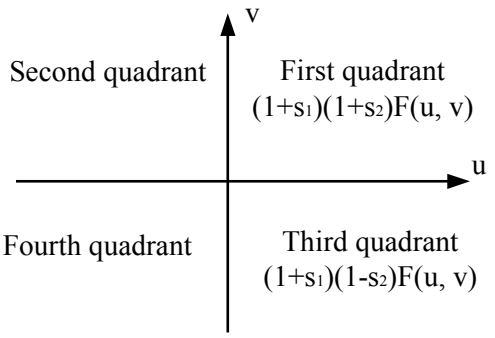

Figure 3.3: The first and third single-quadrant Fourier spectrum obtained from the single-quadrant operators $(1+s_1)(1+s_2)$ and $(1+s_1)(1-s_2)$, respectively.

we have:

$$\begin{aligned} a_1\cos\varphi_1 &= f - H\{f\}, \quad a_1\sin\varphi_1 = H_x\{f\} + H_y\{f\}, \\ a_1^2 &= (f - H\{f\})^2 + (H_x\{f\} + H_y\{f\})^2, \\ \tan\varphi_1 &= \frac{H_x\{f\} + H_y\{f\}}{f - H\{f\}}, \end{aligned}$$

and

$$\begin{aligned} a_3\cos\varphi_3 &= (f + H\{f\}), \quad a_3\sin\varphi_3 = (H_x\{f\} - H_y\{f\}), \\ (a_3)^2 &= (f + H\{f\})^2 + (H_x\{f\} - H_y\{f\})^2, \\ \tan\varphi_3 &= \frac{H_x\{f\} - H_y\{f\}}{f + H\{f\}}. \end{aligned}$$

Then, we have the following equations:

$$f - H\{f\} = a_1\cos\varphi_1, \quad f + H\{f\} = a_3\cos\varphi_3, \tag{3.13}$$

and similarly:

$$H_x\{f\} + H_y\{f\} = a_1\sin\varphi_1, \quad H_x\{f\} - H_y\{f\} = a_3\sin\varphi_3. \tag{3.14}$$

Finally, from these equations, one obtains the solutions as:

$$f(x,y) = \frac{1}{2}(a_1\cos\varphi_1 + a_3\cos\varphi_3), \tag{3.15}$$

$$H\{f(x,y)\} = \frac{1}{2}(-a_1\cos\varphi_1 + a_3\cos\varphi_3), \tag{3.16}$$

$$H_x\{f(x,y)\} = \frac{1}{2}(a_1\sin\varphi_1 + a_3\sin\varphi_3), \tag{3.17}$$

$$H_y\{f(x,y)\} = \frac{1}{2}(a_1\sin\varphi_1 - a_3\sin\varphi_3). \tag{3.18}$$

These solutions means that when we have two 2D Hahn AS of a 2D real signal, we are able to recover the 2D original signal and its total and partial 2D Hilbert transforms by the 2D Hahn AS phases and moduli. Section 3.3.3 gives an example by a 2D real cosine function.

3.3 2D QS

Several works of 2D QS have been previously presented. Here we review the 2D QS calculation from 2D total and partial Hilbert transform. The purpose of this review is to extend this approach to the 3D case which will be presented in the next section.

3.3.1 Definition of 2D QS by Clifford algebra

When extending the AS notion to the 2D case, one of the possible ways is by taking the quaternions as a 2D Clifford algebra with two generators e_1, e_2. The full algebra contains four elements

$$[1 \quad i = e_1 \quad j = e_2 \quad k = e_1 e_2]. \tag{3.19}$$

For a 2D real signal $f(x, y)$, the 2D QS $\psi_q(x, y)$ can be written as:

$$\begin{aligned}
\psi_q(x,y) &= f(x,y) \star\star \left\{ [\delta(x) + \frac{e_1}{\pi x}][\delta(y) + \frac{e_2}{\pi y}] \right\} \\
&= f(x,y) \star\star \left\{ \delta(x)\delta(y) + e_1 \frac{\delta(y)}{\pi x} + e_2 \frac{\delta(x)}{\pi y} + e_1 e_2 \frac{\delta(x)\delta(y)}{\pi^2 xy} \right\} \\
&= f(x,y) \star\star \delta(x)\delta(y) + f(x,y) \star\star e_1 \frac{\delta(y)}{\pi x} + f(x,y) \star\star e_2 \frac{\delta(x)}{\pi y} \\
&\quad + f(x,y) \star\star e_1 e_2 \frac{\delta(x)\delta(y)}{\pi^2 xy} \\
&= f + iH_x\{f\} + jH_y\{f\} + kH\{f\},
\end{aligned} \tag{3.20}$$

where e_1, e_2 are the imaginary units with $e_1 = i, e_2 = j, e_1 e_2 = k$. $\star\star$ is the 2D convolution. $H\{f\}$ is the total Hilbert transform of $f(x, y)$, $H_x\{f\}, H_y\{f\}$ are the partial Hilbert transform of $f(x, y)$ with respect to the orientation x and y, respectively:

$$H_x\{f\} = f(x,y) \star\star \frac{\delta(y)}{\pi x}, \tag{3.21}$$

$$H_y\{f\} = f(x,y) \star\star \frac{\delta(x)}{\pi y}, \tag{3.22}$$

$$H\{f\} = f(x,y) \star\star \frac{\delta(x)\delta(y)}{\pi^2 xy}. \tag{3.23}$$

In addition, we note that there are three types of QFT form [Georgiev *et al.* (2013), Pei *et al.* (2001)]: two-sided QFT, left-sided QFT, and right-sided QFT. The 2D QS in Eq. (3.20) can be computed by the two-sided QFT (see Appendix A). Therefore, it presents

the relation between the two-sided QFT and the classical convolutions in Eqs. (3.21), (3.22), and (3.23). Furthermore, the relation between the right-sided QFT and the classical convolutions are also presented in appendix A, for 2D and also 3D signal. It provides a less complicated way to calculate 2D/3D hypercomplex signals from the classical convolutions instead of from the QFT.

3.3.2 Expression of the 2D QS in terms of 2D Hahn AS

First, we rewrite the 2D QS $\psi_q(x, y)$ in Eq. (2.24) as:

$$\psi_q(x, y) = f + iH_x\{f\} + jH_y\{f\} + kH\{f\} = [f, H_x\{f\}, H_y\{f\}, H\{f\}]. \tag{3.24}$$

Then, substituting the result of single-quadrant 2D Hahn AS in Eqs. (3.15), (3.16), (3.17), (3.18) in Eq. (3.24), we obtain:

$$\begin{aligned}\psi_q &= \frac{1}{2}(a_1\cos\varphi_1 + a_3\cos\varphi_3) + i\left(\frac{1}{2}(a_1\sin\varphi_1 + a_3\sin\varphi_3)\right) \\ &\quad + j\left(\frac{1}{2}(a_1\sin\varphi_1 - a_3\sin\varphi_3)\right) + k\left(\frac{1}{2}(-a_1\cos\varphi_1 + a_3\cos\varphi_3)\right) \\ &= \frac{1}{2}[a_1\cos\varphi_1 + a_3\cos\varphi_3, a_1\sin\varphi_1 + a_3\sin\varphi_3, a_1\sin\varphi_1 - a_3\sin\varphi_3, -a_1\cos\varphi_1 + a_3\cos\varphi_3].\end{aligned} \tag{3.25}$$

This result shows that the QS can be obtained from the Hahn single-quadrant AS. In addition, one has the property:

$$\psi_q(\psi_q)_c = \left[\frac{1}{2}\left(a_1^2 + a_3^2\right), 0, 0, 0\right], \tag{3.26}$$

with the $(\psi_q)_c$ the conjugation of ψ_q defined in Eq. (2.25):

$$(\psi_q)_c = f - iH_x\{f\} - jH_y\{f\} - kH\{f\} = [f, -H_x\{f\}, -H_y\{f\}, -H\{f\}]. \tag{3.27}$$

3.3.3 Numerical implementation of 2D QS calculation by 2D Hahn analytic signal

In order to realize the numerical implementation introduced in the previous sections, we calculate the 2D Hahn analytic signal for the first step. The calculation employs a discrete form of the continuous formula based on the standard FFT and IFFT algorithm. The forward complex Fourier transform result in Eq. (2.1) can be obtained first. Then, applying IFFT on single-quadrant spectrums, we acquire the two 2D Hahn AS in Eqs. (3.11) and (3.12). Hence, the four elements of 2D QS will be calculated by Eqs. (3.15), (3.16), (3.17) and (3.18), which are the original input signal and its total and partial Hilbert transforms. Based on these results and from Eq. (3.20), 2D QS is finally carried out.

We found that in this numerical implementation, only the standard FFT and IFFT on a 2D input data is used to get the 2D QS. As a consequence of our calculation method, to obtain the 2D QS, the Quaternion forward and inverse Fourier transform are not required, which may bring more complexities during the numerical implementation.

Example

One considers a 2D real signal given by:

$$f(x, y) = cos(\omega_1 x)cos(\omega_2 y), \tag{3.28}$$

where ω_1 and ω_2 are the angular frequencies of the signal, $\omega_1 = \omega_2 = 2\pi$. x, y represent the horizontal and vertical directions, respectively. The signal is shown in Fig. 3.4(a). A vertical and a horizontal profiles are marked by two dashed lines, respectively, in this figure, and Fig. 3.4(b) and Fig. 3.4(c) are the corresponding profiles which present the 1D cosine signal with the fixed value of $x = 0.5$ and $y = 0.5$, respectively.

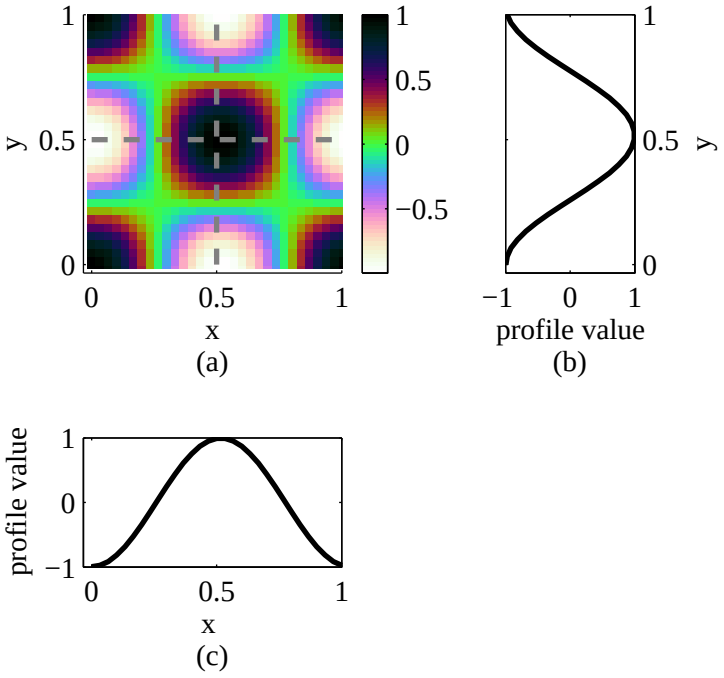

Figure 3.4: (a) the input 2D real signal. $f(x, y) = cos(\omega_1 x)cos(\omega_2 y)$. (b) a vertical profile at $x = 0.5$. (c) a horizontal profile at $y = 0.5$. These profiles represent the 1D cosine signals.

Then, the two 2D Hahn AS are given by:

$$\psi_1(x, y) = cos(\omega_1 x + \omega_2 y) + i' sin(\omega_1 x + \omega_2 y) = e^{(\omega_1 x + \omega_2 y)} = a_1 e^{\varphi_1}, \tag{3.29}$$

$$\psi_3(x, y) = cos(\omega_1 x - \omega_2 y) + i' sin(\omega_1 x - \omega_2 y) = e^{(\omega_1 x - \omega_2 y)} = a_3 e^{\varphi_3}, \tag{3.30}$$

where i' is the usual complex imaginary. The amplitudes $a_1 = a_3 = 1$, and the phases

$\varphi_1 = \omega_1 x + \omega_2 y$, $\varphi_3 = \omega_1 x - \omega_2 y$. For the complex signal $\psi_1(x, y)$, Fig. 3.5(a) and Fig. 3.6(a) show its real part and imaginary part, respectively. Fig. 3.5(b) and (c) present the vertical and horizontal profiles of 1D cosine signals, as well, Fig. 3.6(b) and (c) present the vertical and horizontal profiles of sine signals.

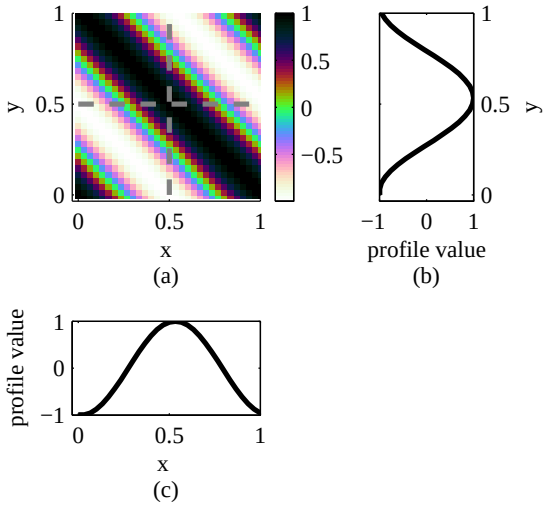

Figure 3.5: The 2D single-quadrant Hahn AS $\psi_1(x, y)$ of $f(x, y)$. (a) The real part of $\psi_1(x, y)$: $cos(\omega_1 x + \omega_2 y)$. (b) and (c) are the vertical and horizontal profiles of (a), respectively.

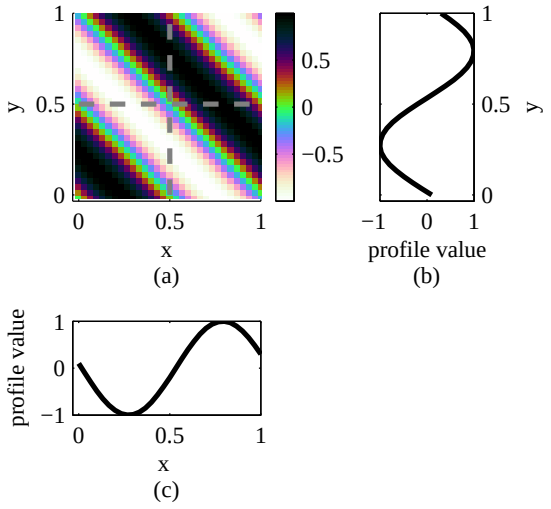

Figure 3.6: The 2D single-quadrant Hahn AS $\psi_1(x, y)$ of $f(x, y)$. (a) The imaginary part of $\psi_1(x, y)$: $sin(\omega_1 x + \omega_2 y)$. (b) and (c) are the vertical and horizontal profiles of (a), respectively.

Similarly, Fig. 3.7 and Fig. 3.8 show the real part and imaginary part, respectively, of the complex signal $\psi_3(x, y)$, with their relevant vertical and horizontal profiles.

When substituting the $a_1, a_3, \varphi_1, \varphi_3$ into Eqs. (3.16)–(3.18), we obtain the total and partial Hilbert transform of the real signal $f(x, y) = cos(\omega_1 x)cos(\omega_2 y)$ from its 2D Hahn AS, it reads:

$$
\begin{aligned}
H\{f(x,y)\} &= \frac{1}{2}\left[-\cos(\omega_1 x + \omega_2 y) + \cos(\omega_1 x - \omega_2 y)\right], \\
H_x\{f(x,y)\} &= \frac{1}{2}\left[\sin(\omega_1 x + \omega_2 y) + \sin(\omega_1 x - \omega_2 y)\right], \\
H_y\{f(x,y)\} &= \frac{1}{2}\left[\sin(\omega_1 x + \omega_2 y) - \sin(\omega_1 x - \omega_2 y)\right].
\end{aligned}
$$

As the result, by Eq. (3.24), the 2D QS $\psi_q(x, y)$ of $f(x, y)$ from these two 2D Hahn AS is:

$$
\begin{aligned}
&\psi_q(x,y) = f(x,y) + iH_x\{f(x,y)\} + jH_y\{f(x,y)\} + kH\{f(x,y)\} \\
&= cos(\omega_1 x)cos(\omega_2 y) + isin(\omega_1 x)cos(\omega_2 y) + jcos(\omega_1 x)sin(\omega_2 y) + ksin(\omega_1 x)sin(\omega_2 y),
\end{aligned}
\tag{3.31}
$$

and it is shown in Fig. 3.9.

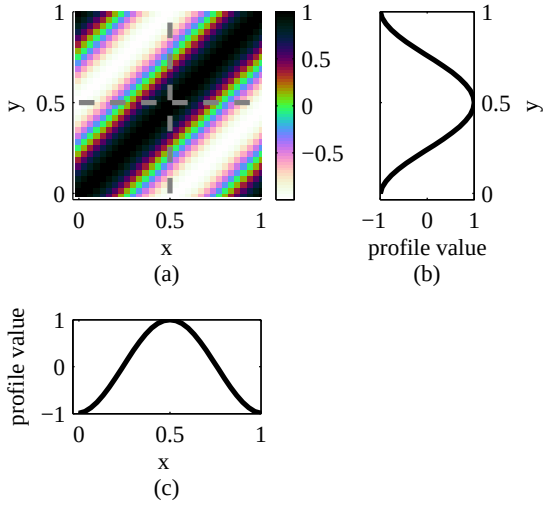

Figure 3.7: The 2D single-quadrant Hahn AS $\psi_3(x,y)$ of $f(x,y)$. (a) The real part of $\psi_3(x,y)$: $cos(\omega_1 x - \omega_2 y)$. (b) and (c) are the vertical and horizontal profiles of (a), respectively.

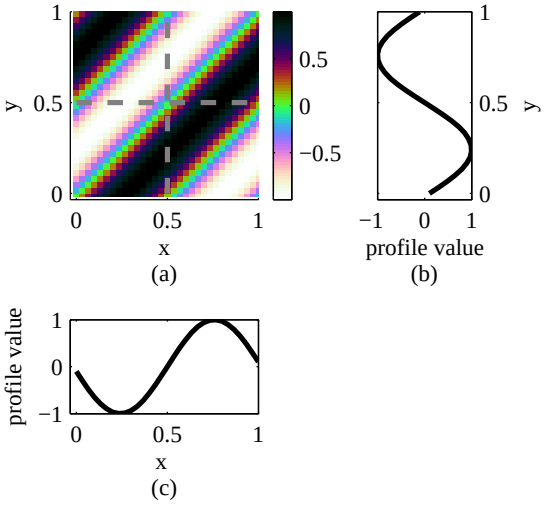

Figure 3.8: The 2D single-quadrant Hahn AS $\psi_3(x,y)$ of $f(x,y)$. (a) The imaginary part of $\psi_3(x,y)$: $sin(\omega_3 x - \omega_2 y)$. (b) and (c) are the vertical and horizontal profiles of (a), respectively.

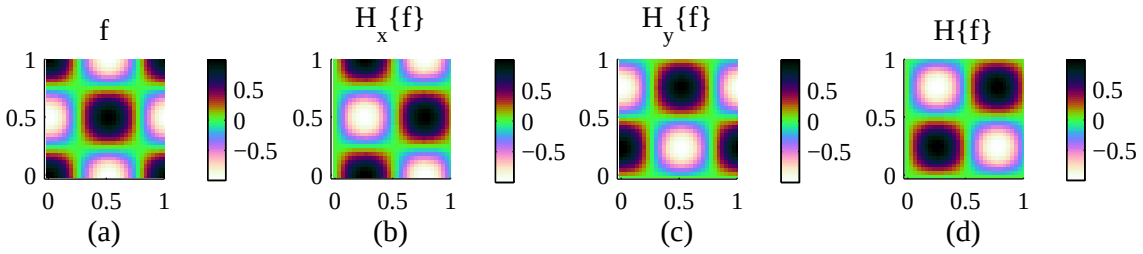

Figure 3.9: The 2D QS $\psi_q(x,y)$=(a)+i(b)+j(c)+k(d). (a) The real part: $cos(\omega_1 x)cos(\omega_2 y)$. (b) The imaginary part of i: $H_x\{f(x,y)\}$=$sin(\omega_1 x)cos(\omega_2 y)$. (c) The imaginary part of j: $H_y\{f(x,y)\}$=$cos(\omega_1 x)sin(\omega_2 y)$. (d) The imaginary part of k: $H\{f(x,y)\}$=$sin(\omega_1 x)sin(\omega_2 y)$.

3.4 3D complex signals with single-orthant spectra

In 2011, the theory of 2D complex signals was extended to n-dimensions by Hahn [Hahn and Snopek (2011)]. For the 3D case, we have the 3D complex analytic signals with single-orthant spectra, which could be obtained by complex nD Fourier Transform. Here, we shall call this signal 3D Hahn AS for short. First we shall introduce the 3D complex Fourier transform in this section. Since all these 3D Hahn AS can be represented by 3D total and partial Hilbert transform, we present therefore the definition of 3D total and partial Hilbert Transform. Then eight 3D Hahn AS with single-orthant spectra are calculated and represented by the Hilbert transforms of the original signal. The results in this section will by employed next for our proposed 3D Clifford analytic signal.

3.4.1 3D complex Fourier transform

The forward complex Fourier transform for a 3D input real signal $f(x, y, z)$ is:

$$F(u, v, w) = \int f(x, y, z) e^{-i' 2\pi(ux+vy+wz)} dxdydz, \tag{3.32}$$

where i' is the usual complex imaginary. The inverse Fourier transform is:

$$f(x, y, z) = \int F(u, v, w) e^{i' 2\pi(ux+vy+wz)} dudvdw. \tag{3.33}$$

From this Fourier transform, several properties are needed to present the Hilbert transformation in the frequency domain, which are listed below:

$$\begin{aligned}
&F\left[\frac{\delta(y)\delta(z)}{\pi x}\right] = -i' sign(u),\\
&F\left[\frac{\delta(x)\delta(z)}{\pi y}\right] = -i' sign(v),\\
&F\left[\frac{\delta(x)\delta(y)}{\pi z}\right] = -i' sign(w),\\
&F\left[\frac{\delta(z)}{\pi^2 xy}\right] = -sign(u)sign(v),\\
&F\left[\frac{\delta(x)}{\pi^2 yz}\right] = -sign(v)sign(w),\\
&F\left[\frac{\delta(y)}{\pi^2 xz}\right] = -sign(u)sign(w),\\
&F\left[\frac{1}{\pi^3 xyz}\right] = i' sign(u)sign(v)sign(w).
\end{aligned} \tag{3.34}$$

3.4.2 3D Hilbert transform

3D total Hilbert transform

For a 3D real signal $f(x, y, z)$, the definition of 3D total Hilbert transform is given by:

$$H\{f(x, y, z)\} = f(x, y, z) \star\star\star \frac{1}{\pi^3 xyz}, \tag{3.35}$$

where $\star\star\star$ denotes the 3D convolution operation. In the frequency domain, by using Eq. (3.34), the definition is:

$$F_H(u, v, w) = i' F(u, v, w) sign(u) sign(v) sign(w), \tag{3.36}$$

with u, v, w are the spatial frequencies and i' is the usual complex imaginary. $F_H(u, v, w)$ and $F(u, v, w)$ are the Fourier transform of $H_{\{}f(x, y, z)\}$ and $f(x, y, z)$, respectively.

3D partial Hilbert transforms

For a 3D real signal $f(x, y, z)$, the definitions of 3D partial Hilbert transforms for one direction x,y and z separately are $H_x\{f(x, y, z)\}$, $H_y\{f(x, y, z)\}$ and $H_z\{f(x, y, z)\}$,

respectively, which are given by:

$$H_x\{f(x,y,z)\} = f(x,y,z) \star\star\star \frac{\delta(y)\delta(z)}{\pi x}, \tag{3.37}$$

$$H_y\{f(x,y,z)\} = f(x,y,z) \star\star\star \frac{\delta(x)\delta(z)}{\pi y}, \tag{3.38}$$

$$H_z\{f(x,y,z)\} = f(x,y,z) \star\star\star \frac{\delta(x)\delta(y)}{\pi z}. \tag{3.39}$$

Similarly, the definitions of 3D partial Hilbert transforms for two directions (x,y),(y,z) and (x,z) separately are $H_{xy}\{f(x,y,z)\}$, $H_{yz}\{f(x,y,z)\}$ and $H_{xz}\{f(x,y,z)\}$, respectively, which are given by:

$$H_{xy}\{f(x,y,z)\} = f(x,y,z) \star\star\star \frac{\delta(z)}{\pi^2 xy}, \tag{3.40}$$

$$H_{yz}\{f(x,y,z)\} = f(x,y,z) \star\star\star \frac{\delta(x)}{\pi^2 yz}, \tag{3.41}$$

$$H_{xz}\{f(x,y,z)\} = f(x,y,z) \star\star\star \frac{\delta(y)}{\pi^2 xz}, \tag{3.42}$$

with $\star\star\star$ denotes the 3D convolution operation. In the frequency domain, by using Eq. (3.34), the definitions are:

$$F_{H_x}(u,v,w) = -i' F(u,v,w) sign(u), \tag{3.43}$$

$$F_{H_y}(u,v,w) = -i' F(u,v,w) sign(v), \tag{3.44}$$

$$F_{H_z}(u,v,w) = -i' F(u,v,w) sign(w), \tag{3.45}$$

$$F_{H_{xy}}(u,v,w) = -F(u,v,w) sign(u) sign(v), \tag{3.46}$$

$$F_{H_{yz}}(u,v,w) = -F(u,v,w) sign(v) sign(w), \tag{3.47}$$

$$F_{H_{xz}}(u,v,w) = -F(u,v,w) sign(u) sign(w), \tag{3.48}$$

where $F_{H_x}(u,v,w)$, $F_{H_y}(u,v,w)$, $F_{H_z}(u,v,w)$, $F_{H_{xy}}(u,v,w)$, $F_{H_{yz}}(u,v,w)$ and $F_{H_{xz}}(u,v,w)$ are the Fourier transform of $H_x\{f(x,y,z)\}$, $H_y\{f(x,y,z)\}$, $H_z\{f(x,y,z)\}$, $H_{xy}\{f(x,y,z)\}$, $H_{yz}\{f(x,y,z)\}$ and $H_{xz}\{f(x,y,z)\}$, respectively.

3.4.3 3D Hahn single-orthant AS

The Hermitian symmetry, which is one property of 3D Fourier transform in 3D case, is applied to calculate the 3D single-orthant AS. As shown in Fig. 3.10, the 3D frequency space has eight (2^3) orthants. Based on the Hermitian symmetry of the Fourier transformation, that the input signal can be recovered from any of its half plane spectrum, the 3D real signal can be represented by four ($2^3/2$) analytic signals.

In the following, without loss of generality, we work on the half space spectra with $u > 0$ to calculate the four single-orthant analytic signals, that is to say the orthants with the labels I, III, V and VII in Fig. 3.10.

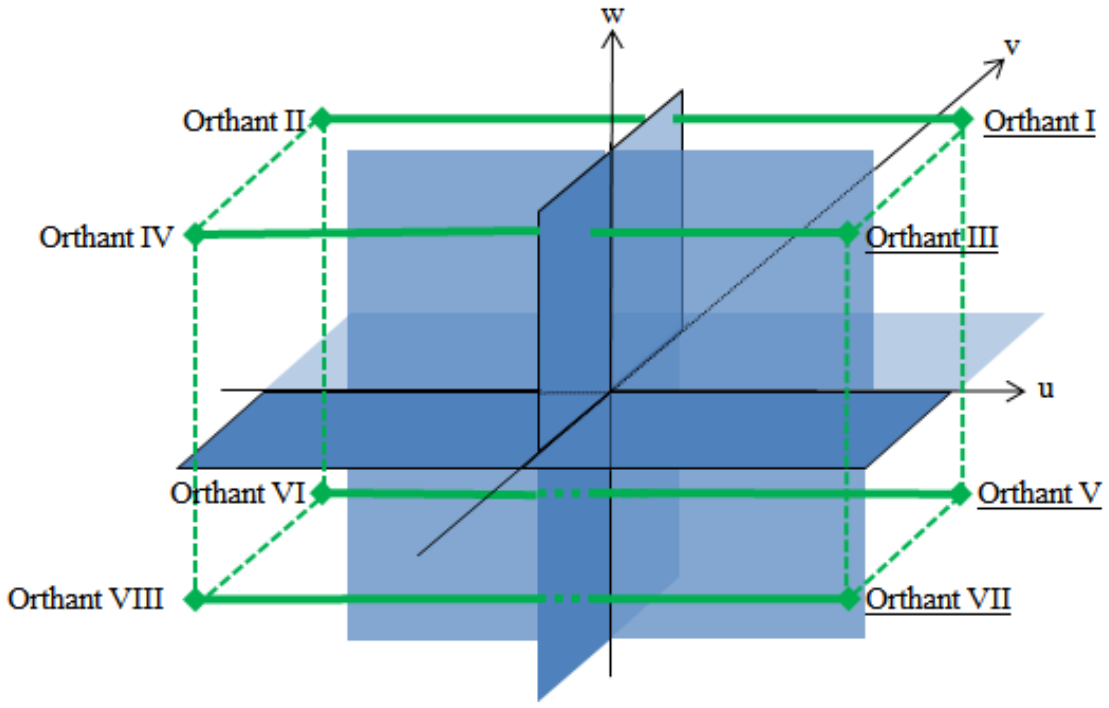

Figure 3.10: The eight orthant frequency space with a label number of each orthant.

(1) Writing $s_1 = sign(u)$, $s_2 = sign(v)$ and $s_3 = sign(w)$, we have the 3D Hahn AS from the first orthant:

$$\begin{aligned}\psi_1(x,y,z) =& F^{-1}\left[(1+s_1)(1+s_2)(1+s_3)F(u,v,w)\right]\\ =& (f - H_{xy}\{f\} - H_{xz}\{f\} - H_{yz}\{f\})\\ &+ i'(H_x\{f\} + H_y\{f\} + H_z\{f\} - H\{f\})\\ =& a_1 e^{i'\varphi_1} = a_1\cos\varphi_1 + i' a_1 \sin\varphi_1,\end{aligned} \tag{3.49}$$

where a_1 and φ_1 are the modulus and the phase, respectively, of the polar form of ψ_1. Hence,

$$\begin{aligned}a_1\cos\varphi_1 &= (f - H_{xy}\{f\} - H_{xz}\{f\} - H_{yz}\{f\}),\\ a_1\sin\varphi_1 &= (H_x\{f\} + H_y\{f\} + H_z\{f\} - H\{f\}).\end{aligned}$$

Then, the modulus a_1 and the phase φ_1 can be found from:

$$(a_1)^2 = (f - H_{xy}\{f\} - H_{xz}\{f\} - H_{yz}\{f\})^2 + (H_x\{f\} + H_y\{f\} + H_z\{f\} - H\{f\})^2, \tag{3.50}$$

$$\tan\varphi_1 = \frac{(H_x\{f\} + H_y\{f\} + H_z\{f\} - H\{f\})}{(f - H_{xy}\{f\} - H_{xz}\{f\} - H_{yz}\{f\})}. \tag{3.51}$$

(2) Similarly, the 3D Hahn AS from the third orthant:

$$\begin{aligned}\psi_3(x,y,z) =& F^{-1}\left[(1+s_1)(1-s_2)(1+s_3)F(u,v,w)\right]\\ =& (f + H_{xy}\{f\} - H_{xz}\{f\} + H_{yz}\{f\})\\ &+ i'(H_x\{f\} - H_y\{f\} + H_z\{f\} + H\{f\})\\ =& a_3 e^{i'\varphi_3} = a_3\cos\varphi_3 + i' a_3 \sin\varphi_3,\end{aligned} \tag{3.52}$$

where a_3 and φ_3 are the modulus and the phase, respectively, of the polar form of ψ_3. Hence,

$$\begin{aligned}a_3\cos\varphi_3 &= (f + H_{xy}\{f\} - H_{xz}\{f\} + H_{yz}\{f\}),\\ a_3\sin\varphi_3 &= (H_x\{f\} - H_y\{f\} + H_z\{f\} + H\{f\}).\end{aligned}$$

Then, the modulus a_3 and the phase φ_3 can be found from:

$$(a_3)^2 = (f + H_{xy}\{f\} - H_{xz}\{f\} + H_{yz}\{f\})^2 + (H_x\{f\} - H_y\{f\} + H_z\{f\} + H\{f\})^2, \tag{3.53}$$

$$\tan\varphi_3 = \frac{(H_x\{f\} - H_y\{f\} + H_z\{f\} + H\{f\})}{(f + H_{xy}\{f\} - H_{xz}\{f\} + H_{yz}\{f\})}. \tag{3.54}$$

(3) For the 3D Hahn AS from the fifth orthant, we have:

$$\begin{aligned}\psi_5(x,y,z) =& F^{-1}\left[(1+s_1)(1+s_2)(1-s_3)F(u,v,w)\right]\\ =& (f - H_{xy}\{f\} + H_{xz}\{f\} + H_{yz}\{f\})\\ &+ i'(H_x\{f\} + H_y\{f\} - H_z\{f\} + H\{f\})\\ =& a_5 e^{i'\varphi_5} = a_5\cos\varphi_5 + i' a_5 \sin\varphi_5,\end{aligned} \tag{3.55}$$

where a_5 and φ_5 are the modulus and the phase, respectively, of the polar form of ψ_5. Hence,

$$\begin{aligned}a_5\cos\varphi_5 &= (f - H_{xy}\{f\} + H_{xz}\{f\} + H_{yz}\{f\}),\\ a_5\sin\varphi_5 &= (H_x\{f\} + H_y\{f\} - H_z\{f\} + H\{f\}).\end{aligned}$$

Then, the modulus a_5 and the phase φ_5 can be found from:

$$(a_5)^2 = (f - H_{xy}\{f\} + H_{xz}\{f\} + H_{yz}\{f\})^2 + (H_x\{f\} + H_y\{f\} - H_z\{f\} + H\{f\})^2, \tag{3.56}$$

$$\tan\varphi_3 = \frac{(H_x\{f\} + H_y\{f\} - H_z\{f\} + H\{f\})}{(f - H_{xy}\{f\} + H_{xz}\{f\} + H_{yz}\{f\})}. \tag{3.57}$$

(4) For the 3D Hahn AS from the seventh orthant, we have:

$$\begin{aligned}\psi_7(x,y,z) =& F^{-1}\left[(1+s_1)(1-s_2)(1-s_3)F(u,v,w)\right]\\ =& (f + H_{xy}\{f\} + H_{xz}\{f\} - H_{yz}\{f\})\\ &+ i'(H_x\{f\} - H_y\{f\} - H_z\{f\} - H\{f\})\\ =& a_7 e^{i'\varphi_7} = a_7\cos\varphi_7 + i' a_7 \sin\varphi_7,\end{aligned} \tag{3.58}$$

where a_7 and φ_7 are the modulus and the phase, respectively, of the polar form of ψ_7. Hence,

$$\begin{aligned}a_7\cos\varphi_7 &= (f + H_{xy}\{f\} + H_{xz}\{f\} - H_{yz}\{f\}),\\ a_7\sin\varphi_7 &= (H_x\{f\} - H_y\{f\} - H_z\{f\} - H\{f\}).\end{aligned}$$

Then, the modulus a_7 and the phase φ_7 can be found from:

$$(a_7)^2 = (f + H_{xy}\{f\} + H_{xz}\{f\} - H_{yz}\{f\})^2 + (H_x\{f\} - H_y\{f\} - H_z\{f\} - H\{f\})^2, \tag{3.59}$$

$$\tan\varphi_7 = \frac{(H_x\{f\} - H_y\{f\} - H_z\{f\} - H\{f\})}{(f + H_{xy}\{f\} + H_{xz}\{f\} - H_{yz}\{f\})}. \tag{3.60}$$

Finally, we have the following equations:

$$\begin{aligned}f - H_{xy}\{f\} - H_{xz}\{f\} - H_{yz}\{f\} &= a_1\cos\varphi_1, \quad f + H_{xy}\{f\} - H_{xz}\{f\} + H_{yz}\{f\} = a_3\cos\varphi_3,\\ f - H_{xy}\{f\} + H_{xz}\{f\} + H_{yz}\{f\} &= a_5\cos\varphi_5, \quad f + H_{xy}\{f\} + H_{xz}\{f\} - H_{yz}\{f\} = a_7\cos\varphi_7,\\ H_x\{f\} + H_y\{f\} + H_z\{f\} - H\{f\} &= a_1\sin\varphi_1, \quad H_x\{f\} - H_y\{f\} + H_z\{f\} + H\{f\} = a_3\sin\varphi_3,\\ H_x\{f\} - H_y\{f\} - H_z\{f\} - H\{f\} &= a_5\sin\varphi_5, \quad H_x\{f\} - H_y\{f\} - H_z\{f\} - H\{f\} = a_7\sin\varphi_7.\end{aligned}$$

From these equations, one obtains the solutions:

$$f = \tfrac{1}{4}(a_1\cos\varphi_1 + a_3\cos\varphi_3 + a_5\cos\varphi_5 + a_7\cos\varphi_7), \tag{3.61}$$

$$H_{yz}\{f\} = \tfrac{1}{4}(-a_1\cos\varphi_1 + a_3\cos\varphi_3 + a_5\cos\varphi_5 - a_7\cos\varphi_7), \tag{3.62}$$

$$-H_{xz}\{f\} = \tfrac{1}{4}(a_1\cos\varphi_1 + a_3\cos\varphi_3 - a_5\cos\varphi_5 - a_7\cos\varphi_7), \tag{3.63}$$

$$H_{xy}\{f\} = \tfrac{1}{4}(-a_1\cos\varphi_1 + a_3\cos\varphi_3 - a_5\cos\varphi_5 + a_7\cos\varphi_7), \tag{3.64}$$

$$-H\{f\} = \tfrac{1}{4}(a_1\sin\varphi_1 - a_3\sin\varphi_3 - a_5\sin\varphi_5 + a_7\sin\varphi_7), \tag{3.65}$$

$$H_x\{f\} = \tfrac{1}{4}(a_1\sin\varphi_1 + a_3\sin\varphi_3 + a_5\sin\varphi_5 + a_7\sin\varphi_7), \tag{3.66}$$

$$H_y\{f\} = \tfrac{1}{4}(a_1\sin\varphi_1 - a_3\sin\varphi_3 + a_5\sin\varphi_5 - a_7\sin\varphi_7), \tag{3.67}$$

$$H_z\{f\} = \tfrac{1}{4}(a_1\sin\varphi_1 + a_3\sin\varphi_3 - a_5\sin\varphi_5 - a_7\sin\varphi_7). \tag{3.68}$$

From these eight equations, we conclude that similarly to the 2D signal in section 3.2: a 3D signal, itself and its total and partial 3D Hilbert transforms can be recovered by

the phases and moduli of its 3D Hahn ASs. Moreover, for the 3D case, four 3D Hahn signal-orthant ASs are needed, which correspond to the half plane spectrum of the input signal. This result will be used in section 3.5.2. An example of 3D Hahn signal-orthant AS is presented in the section 3.5.3.

3.5 3D Clifford analytic signal

In section 3.3.1, we presented the 2D QS in the frame of 3D Clifford algebra (with two generators e_1, e_2), then we showed in section 3.3.2, that the hypercomplex QS can be recovered by simpler complex Hahn ASs. Hence, in the framework of 2D Clifford algebra, we obtain a relation between 2D hypercomplex signal (QS) and 2D complex signal (AS). Therefore, in this section, we take the framework of 3D Clifford algebra (with three generators), to find a relation between 3D hypercomplex signal and the 3D complex signal.

3.5.1 Definition

In order to extend the notion of 2D QS to 3D case in the Clifford algebra, we consider the Clifford biquaternions, which have three generators as: e_1, e_2, e_3. The full algebra contains eight elements:

$$\begin{bmatrix} 1 & i = e_2e_3 & j = e_3e_1 & k = e_1e_2 \\ \epsilon = i'I = -e_1e_2e_3 & \epsilon i = e_1 & \epsilon j = e_2 & \epsilon k = e_3 \end{bmatrix}. \tag{3.69}$$

with $\epsilon^2 = 1, e_1^2 = e_2^2 = e_3^2 = -1$, i' representing the usual complex imaginary ($i'^2 = -1$) and where the tensor product $I = 1 \otimes i$ ($I^2 = -1$) commutes with $i = i \otimes 1, j = j \otimes 1, k = k \otimes 1$. For a 3D input real signal $f(x, y, z)$, the 3D Clifford analytic signal (CAS) can be defined as:

$$\psi_{bq}(x, y, z) = f(x, y, z) \star\star\star \left\{ \left[\delta(x) + \frac{e_1}{\pi x} \right] \left[\delta(y) + \frac{e_2}{\pi y} \right] \left[\delta(z) + \frac{e_3}{\pi z} \right] \right\}. \tag{3.70}$$

The mathematical development of $\psi_{bq}(x, y, z)$ of Eq. (3.70) results in the sum of the original signal, the Hilbert transform as pseudo-scalar part, and six partial Hilbert transforms as the imaginary parts. All the eight elements constitute a biquaternion:

$$\begin{aligned} \psi_{bq}(x, y, z) =& f(x, y, z) \star\star\star \left\{ \left[\delta(x) + \frac{e_1}{\pi x} \right] \left[\delta(y) + \frac{e_2}{\pi y} \right] \left[\delta(z) + \frac{e_3}{\pi z} \right] \right\} \\ =& f(x, y, z) \star\star\star \left\{ \delta(x)\delta(y)\delta(z) + \delta(x)\delta(y)\frac{e_3}{\pi z} + \delta(x)\frac{e_2}{\pi y}\delta(z) + \delta(x)\frac{e_2}{\pi y}\frac{e_3}{\pi z} \right. \\ & \left. + \frac{e_1}{\pi x}\delta(y)\delta(z) + \frac{e_1}{\pi x}\delta(y)\frac{e_3}{\pi z} + \frac{e_1}{\pi x}\frac{e_2}{\pi y}\delta(z) + \frac{e_1}{\pi x}\frac{e_2}{\pi y}\frac{e_3}{\pi z} \right\}, \end{aligned} \tag{3.71}$$

with

$$f(x,y,z) \star\star\star [\delta(x)\delta(y)\delta(z)] = f(x,y,z), \qquad f(x,y,z) \star\star\star [\delta(x)\delta(y)\frac{e_3}{\pi z}] = e_3 H_z\{f\},$$
$$f(x,y,z) \star\star\star [\delta(x)\frac{e_2}{\pi y}\delta(z)] = e_2 H_y\{f\}, \qquad f(x,y,z) \star\star\star [\frac{e_1}{\pi x}\delta(y)\delta(z)] = e_1 H_x\{f\},$$
$$f(x,y,z) \star\star\star [\delta(x)\frac{e_2}{\pi y}\frac{e_3}{\pi z}] = e_2 e_3 H_{yz}\{f\}, \qquad f(x,y,z) \star\star\star [\frac{e_1}{\pi x}\delta(y)\frac{e_3}{\pi z}] = e_1 e_3 H_{xz}\{f\},$$
$$f(x,y,z) \star\star\star [\frac{e_1}{\pi x}\frac{e_2}{\pi y}\delta(z)] = e_1 e_2 H_{xy}\{f\}, \qquad f(x,y,z) \star\star\star [\frac{e_1}{\pi x}\frac{e_2}{\pi y}\frac{e_3}{\pi z}] = e_1 e_2 e_3 H\{f\},$$

where e_1, e_2, e_3 are the imaginary units with the relation in Eq. (3.69), $\star\star\star$ are the 3D convolution. $H\{f\}$ is the total 3D Hilbert transform of $f(x,y,z)$ and $H_x\{f\}$, $H_y\{f\}$, $H_z\{f\}$, $H_{xy}\{f\}$, $H_{xz}\{f\}$, $H_{yz}\{f\}$ are the partial Hilbert transform of $f(x,y,z)$. Hence, by 3D Clifford algebra in Eq. (3.69), $\psi_{bq}(x,y,z)$ is written by:

$$\psi_{bq}(x,y,z) = \begin{bmatrix} f & iH_{yz}\{f\} & j(-H_{xz}\{f\}) & kH_{xy}\{f\} \\ \epsilon(-H\{f\}) & \epsilon i H_x\{f\} & \epsilon j H_y\{f\} & \epsilon k H_z\{f\} \end{bmatrix}. \tag{3.72}$$

3.5.2 Expression of the 3D Clifford analytic signal in terms of 3D Hahn analytic signals

From Eq. (3.72) and section 3.4.3, we found that all the elements in both of the 3D Hahn AS and 3D CAS can be represented by the total and partial Hilbert Transform of the original real signal. As the result, when substituting the 3D Hahn AS results of section 3.4.3 in the 3D CAS of ψ_{bq} in Eq. (3.72), we obtain the 3D CAS which is represented by the 3D Hahn single-quadrant AS as follows:

$$\psi_{bq} = \frac{1}{4}\begin{bmatrix} (a_1\cos\varphi_1 + a_3\cos\varphi_3 + a_5\cos\varphi_5 + a_7\cos\varphi_7), \\ i(-a_1\cos\varphi_1 + a_3\cos\varphi_3 + a_5\cos\varphi_5 - a_7\cos\varphi_7), \\ j(a_1\cos\varphi_1 + a_3\cos\varphi_3 - a_5\cos\varphi_5 - a_7\cos\varphi_7), \\ k(-a_1\cos\varphi_1 + a_3\cos\varphi_3 - a_5\cos\varphi_5 + a_7\cos\varphi_7), \\ \epsilon(a_1\sin\varphi_1 - a_3\sin\varphi_3 - a_5\sin\varphi_5 + a_7\sin\varphi_7), \\ \epsilon i(a_1\sin\varphi_1 + a_3\sin\varphi_3 + a_5\sin\varphi_5 + a_7\sin\varphi_7), \\ \epsilon j(a_1\sin\varphi_1 - a_3\sin\varphi_3 + a_5\sin\varphi_5 - a_7\sin\varphi_7), \\ \epsilon k(a_1\sin\varphi_1 + a_3\sin\varphi_3 - a_5\sin\varphi_5 - a_7\sin\varphi_7) \end{bmatrix}. \tag{3.73}$$

Using the biquaternion product in Eq. (2.51) and the biquaternion conjugate in Eq. (2.52), one obtains the property:

$$\psi_{bq}(\psi_{bq})_c = \begin{bmatrix} \frac{1}{4}\left(a_1^2 + a_3^2 + a_5^2 + a_7^2\right), \\ i(0), \\ j(0), \\ k(0), \\ \epsilon\left(\frac{1}{2}\left[a_1 a_3 \sin\left(\varphi_1 - \varphi_3\right) - a_5 a_7 \sin\left(\varphi_5 - \varphi_7\right)\right]\right), \\ \epsilon i(0), \\ \epsilon j(0), \\ \epsilon k(0), \end{bmatrix}. \tag{3.74}$$

The modulus for ψ_{bq} could be defined to be $|\psi_{bq}|$. The calculation of $|\psi_{bq}|$ is in the following: Let's define:

$$\psi_{bq} = |\psi_{bq}| e^{\epsilon\varphi} a,$$

where $|\psi_{bq}|$ is the modulus of the biquaternion. a is the unit biquaterion, with $a a_c = 1$.

The product of $\psi_{bq}(\psi_{bq})_c$ may be represented by:

$$\psi_{bq}(\psi_{bq})_c = |\psi_{bq}|^2 e^{2\epsilon\varphi} = A + \epsilon B, \tag{3.75}$$

where A is the scalar part and B is the pseudo-scalar part of the biquaternion $\psi_{bq}(\psi_{bq})_c$, respectively.

By the series expansion, one obtains:

$$\begin{aligned} e^{2\epsilon\varphi} &= 1 + 2\epsilon\varphi + \frac{(2\epsilon\varphi)^2}{2!} + \frac{(2\epsilon\varphi)^3}{3!} + \cdots + \frac{(2\epsilon\varphi)^{2r}}{(2r)!} + \frac{(2\epsilon\varphi)^{2r+1}}{(2r+1)!} \cdots \\ &= \left[1 + \frac{(2\epsilon\varphi)^2}{2!} + \frac{(2\epsilon\varphi)^4}{4!} + \cdots \frac{(2\epsilon\varphi)^{2r}}{(2r)!} + \cdots\right] \\ &\quad + \left[2\epsilon\varphi + \frac{(2\epsilon\varphi)^3}{3!} + \frac{(2\epsilon\varphi)^5}{5!} + \cdots + \frac{(2\epsilon\varphi)^{2r+1}}{(2r+1)!} + \cdots\right] \\ &= \left[1 + \frac{(2\varphi)^2}{2!} + \frac{(2\varphi)^4}{4!} + \cdots + \frac{(2\varphi)^{2r}}{(2r)!} + \cdots\right] \\ &\quad + \epsilon\left[2\varphi + \frac{(2\varphi)^3}{3!} + \frac{(2\varphi)^5}{5!} + \cdots + \frac{(2\varphi)^{2r+1}}{(2r+1)!} + \cdots\right] \\ &= ch(2\varphi) + \epsilon sh(2\varphi), \end{aligned}$$

where $r \in \mathbb{Z}^+$, and $\epsilon^2 = 1$ (see Eq. (3.69)). $sh()$ and $ch()$ are the hyperbolic sine and hyperbolic cosine function, respectively.

Hence,

$$\psi_{bq}(\psi_{bq})_c = |\psi_{bq}|^2 e^{2\epsilon\varphi} = A + \epsilon B = |\psi_{bq}|^2 ch(2\varphi) + \epsilon |\psi_{bq}|^2 sh(2\varphi).$$

One obtains:

$$A = |\psi_{bq}|^2 ch(2\varphi), \qquad B = |\psi_{bq}|^2 sh(2\varphi),$$

and

$$A^2 - B^2 = |\psi_{bq}|^4 [ch^2(2\varphi) - sh^2(2\varphi)] = |\psi_{bq}|^4.$$

Then,

$$|\psi_{bq}| = \sqrt[4]{A^2 - B^2}. \tag{3.76}$$

Finally, from Eq. (3.74), Eq. (3.75), and Eq. (3.76), the modulus $|\psi_{bq}|$ is represented as:

$$|\psi_{bq}| = \sqrt[4]{\left[\frac{1}{4}\left(a_1^2 + a_3^2 + a_5^2 + a_7^2\right)\right]^2 - \left[\frac{1}{2}\left[a_1 a_3 \sin\left(\varphi_1 - \varphi_3\right) - a_5 a_7 \sin\left(\varphi_5 - \varphi_7\right)\right]\right]^2}, \tag{3.77}$$

which can be employed to calculate the modulus of a 3D input signal as an application.

3.5.3 Numerical implementation of 3D CAS calculation by 3D Hahn AS

Similar procedures are employed for the numerical implementation of 3D CAS as in the 2D case. We derive the 3D Hahn analytic signal for the first step. The calculation employs a discrete from of the continuous formula based on the standard 3D FFT and IFFT algorithm. The forward complex Fourier transform result in Eq. (3.32) is obtained first. Then, applying the IFFT on single-quadrant spectra, we acquire the four 3D Hahn AS in Eqs. (3.49), (3.52), (3.55), and (3.58). Hence, the eight elements of 3D CAS will be calculated by Eqs. (3.61) to (3.68), which are the original real signal and its total and partial Hilbert transforms. Based on these results and from Eq. (3.73), the 3D CAS is obtained at last.

During this numerical implementation of the 3D CAS calculation, only the standard FFT and IFFT on a 3D input data are used, which give a simple and fast way of calculation without defining the biquaternion Fourier transformation and its numerical implementation.

Example 1: introductory 3D cosine signal

One considers a 3D real signal given by:

$$f(x, y) = cos(\omega_1 x) cos(\omega_2 y) cos(\omega_3 z), \tag{3.78}$$

where ω_1, ω_2, and ω_3 are the angular frequencies of the signal with $\omega_1 = \omega_2 = \omega_3 = 2\pi$. $(x, y, z$ represent three orthogonal directions, respectively). The signal is shown in Fig. 3.11. Three slices are presented in this figure, each slice corresponds to a fixed value of $x = 0.5$, $y = 0.5$, and $z = 0$, respectively.

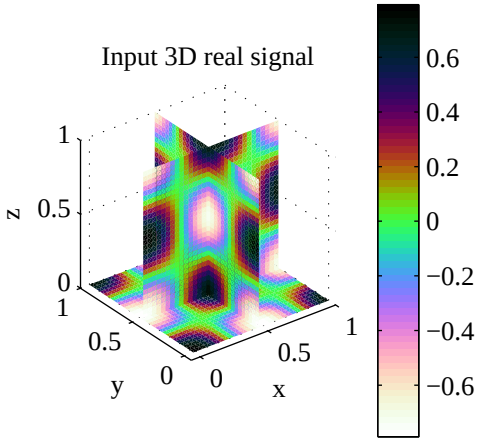

Figure 3.11: The input 3D real signal. $f(x, y, z) = cos(\omega_1 x)cos(\omega_2 y)cos(\omega_3 z)$. The three slices are presented for a fixed value of $x = 0.5$, $y = 0.5$, and $z = 0$, respectively.

Then, the four 3D Hahn single-orthant AS are given by:

$$\psi_1(x, y, z) = cos(\omega_1 x + \omega_2 y + \omega_3 z) + i' sin(\omega_1 x + \omega_2 y + \omega_3 z), \tag{3.79}$$
$$\psi_3(x, y, z) = cos(\omega_1 x - \omega_2 y + \omega_3 z) + i' sin(\omega_1 x - \omega_2 y + \omega_3 z), \tag{3.80}$$
$$\psi_5(x, y, z) = cos(\omega_1 x + \omega_2 y - \omega_3 z) + i' sin(\omega_1 x + \omega_2 y - \omega_3 z), \tag{3.81}$$
$$\psi_7(x, y, z) = cos(\omega_1 x - \omega_2 y - \omega_3 z) + i' sin(\omega_1 x - \omega_2 y - \omega_3 z), \tag{3.82}$$

where i' is the usual complex imaginary (Fig. 3.12 illustrate the 3D Hahn AS of the first orthant $\psi_1(x, y, z)$). Several slice images of the 3D data are presented. For the real part, three fixed values on each axis are given to show three slice images. For example, from Eq. (3.79), the real part of $\psi_1(x, y, z)$ is:

$$Re\left[\psi_1(x, y, z)\right] = cos(\omega_1 x + \omega_2 y + \omega_3 z). \tag{3.83}$$

Figure. 3.12(a) presents three slices from the real part of $\psi_1(x, y, z)$ at fixed x values of 0, 0.5, and 1. Therefore, the three slices are:

$$Re\left[\psi_1(x, y, z)\right] = cos(\omega_2 y + \omega_3 z), \text{ for } x = 0,$$
$$Re\left[\psi_1(x, y, z)\right] = cos(\tfrac{1}{2}\omega_1 + \omega_2 y + \omega_3 z), \text{ for } x = 0.5,$$
$$Re\left[\psi_1(x, y, z)\right] = cos(\omega_1 + \omega_2 y + \omega_3 z), \text{ for } x = 1,$$

with the angular frequencies $\omega_1 = \omega_2 = \omega_3 = 2\pi$. In the same way, Fig. 3.12(b) presents the other three slice image at fixed y values of 0, 0.5, and 1. and Fig. 3.12(c) are the slices

from the fixed z values of 0, 0.5, and 1. Moreover, the imaginary part of $\psi_1(x, y, z)$ is presented similarly in Fig. 3.12(d)–(f).

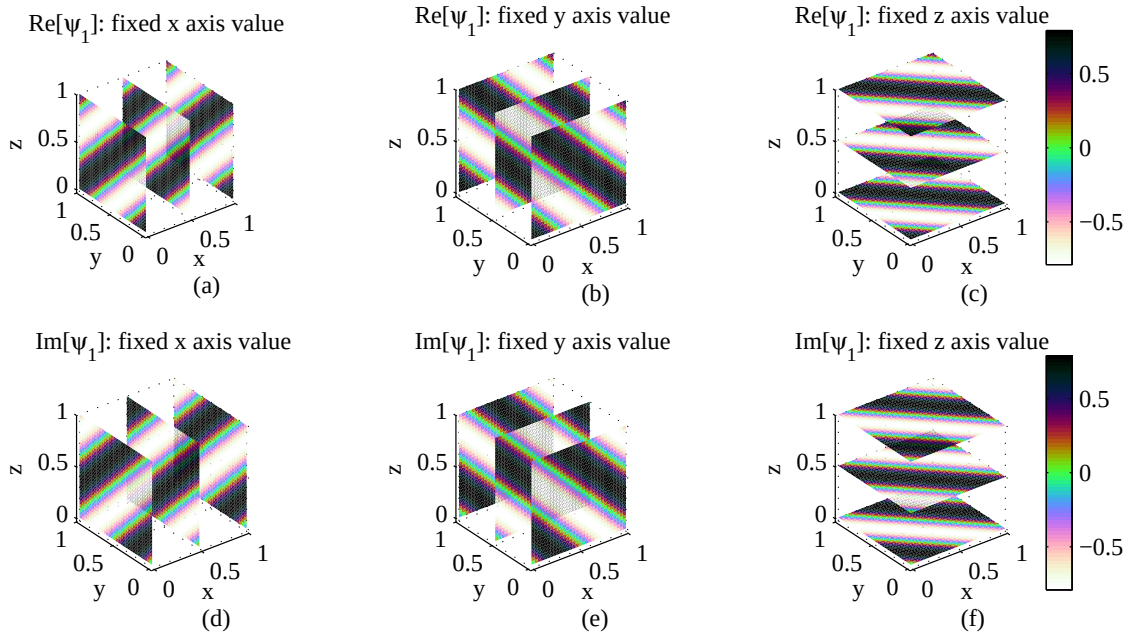

Figure 3.12: The slices of the 3D single-orthant Hahn AS $\psi_1(x, y, z)$ of $f(x, y, z)$ with their real part in (a)–(c) and imaginary part in (d)–(f). In (a) and (d) three slices are presented at the fixed values of x values of 0, 0.5, and 1. (b) and (e) present the fixed y value slices; (c) and (f) present the fixed z value slices.

As result, the 3D CAS $\psi_bq(x, y, z)$ of $f(x, y, z)$ from these four 3D Hahn AS is:

$$\psi_{bq}(x,y,z) = \begin{bmatrix} (cos(\omega_1 x)cos(\omega_2 y)cos(\omega_3 z))\,, \\ i\,(cos(\omega_1 x)sin(\omega_2 y)sin(\omega_3 z))\,, \\ j\,(-sin(\omega_1 x)cos(\omega_2 y)sin(\omega_3 z))\,, \\ k\,(sin(\omega_1 x)sin(\omega_2 y)cos(\omega_3 z))\,, \\ \epsilon\,(-sin(\omega_1 x)sin(\omega_2 y)sin(\omega_3 z))\,, \\ \epsilon i\,(sin(\omega_1 x)cos(\omega_2 y)cos(\omega_3 z))\,, \\ \epsilon j\,(cos(\omega_1 x)sin(\omega_2 y)cos(\omega_3 z))\,, \\ \epsilon k\,(cos(\omega_1 x)cos(\omega_2 y)sin(\omega_3 z))\,, \end{bmatrix}, \tag{3.84}$$

and is shown in Fig. 3.13 by one slice on x, y, z axis, respectively, for each of the eight components.

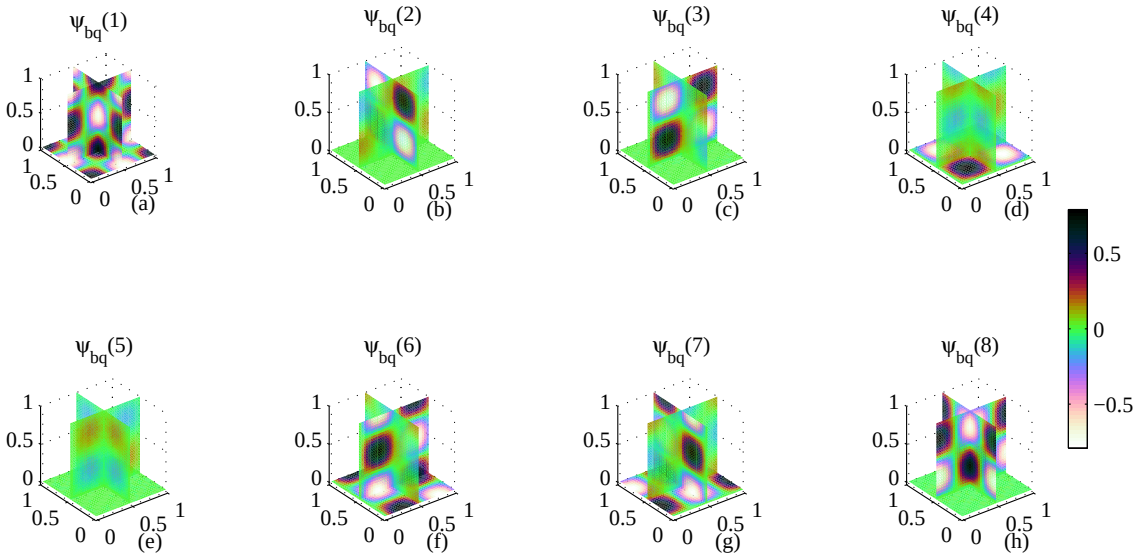

Figure 3.13: The 3D CAS $\psi_{bq}(x, y, z)$ of $f(x, y, z)$. (a)–(h) The eight elements of $\psi_{bq}(x, y, z)$. One slice on x, y, z axis, respectively, is chosen to present each of these eight components.

Example 2: demodulation by 3D CAS

To verify the envelope detection method of 3D CAS, we consider a modulated 3D signal given by:

$$f(x, y, z) = (1 + K \cos(\omega_1 x) \cos(\omega_2 y) \cos(\omega_3 z)) \cos(\Omega_1 x) \cos(\Omega_2 y) \cos(\Omega_3 z), \quad (3.85)$$

where ω_1, ω_2 and ω_3 are the low spatial frequencies, and Ω_1, Ω_2 and Ω_3 are the high spatial carrier frequencies, K is the amplitude of the low spatial frequency wave. This input signal is shown in Fig. 3.14.

As in the introductory example, we compute the 3D CAS $\psi_{bq}(x, y, z)$ first. Then its modulus $|\psi_{bq}(x, y, z)|$ in Eq. (3.77) can be obtained. The 3 slices on each axis, respectively, in Fig. 3.15 show the numerical result of the modulus $|\psi_{bq}(x, y, z)|$ of the modulated 3D input signal. This result corresponds to the expected low frequency part of the input signal, i.e. $(1 + K \cos(\omega_1 x) \cos(\omega_2 y) \cos(\omega_3 z))$, with the values $\omega_1 = 2\pi$, $\omega_2 = 4\pi$, $\omega_3 = 6\pi$, $\Omega_1 = 16\pi$, $\Omega_2 = 18\pi$, $\Omega_3 = 20\pi$, and $K = 0.6$. The error between the algebraical and numerical result is less than $1 \times 10^{-14} \approx 0$, which is shown in Fig. 3.16. Hence, it means that we correctly recover the envelope of the modulated 3D signal in Eq. (3.85) from its 3D CAS.

3.6 Application of 3D envelope detection by 3D CAS

Radio frequency and B-mode ultrasound images are two different data types. There are several steps to convert from RF to B-mode [Hedrick *et al.* (2004)], such as demodulation,

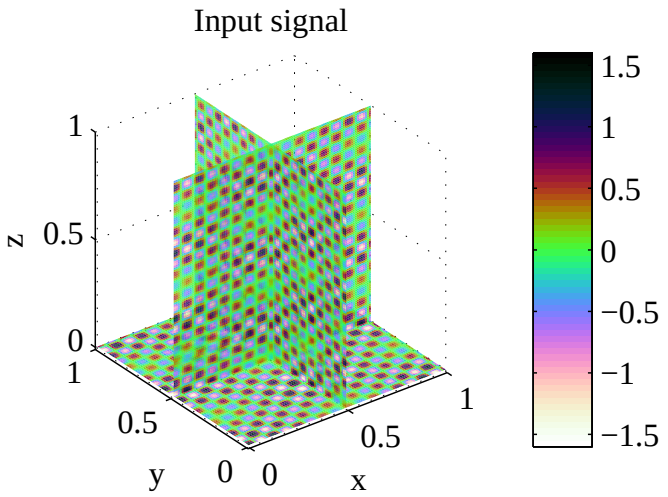

Figure 3.14: a modulated 3D signal $f(x, y, z)$.

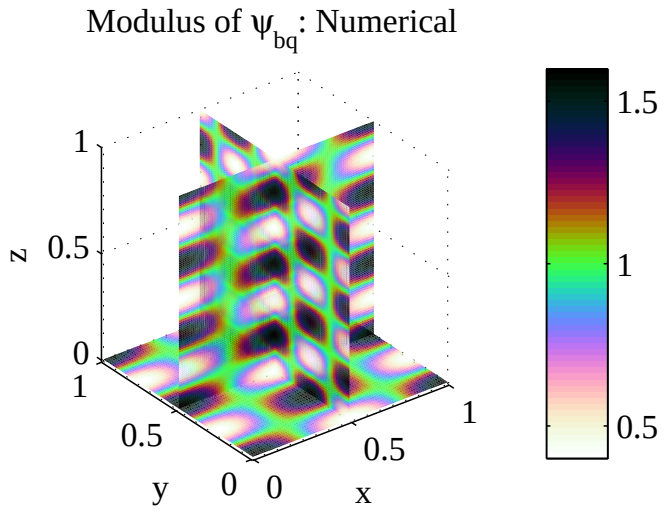

Figure 3.15: 3 slices on axis x, y and z, respectively, for the modulus $|\psi_{bq}(x, y, z)|$ of a 3D modulated signal.

nonlinear intensity mapping, filtering, etc. Figure 3.17 shows an example diagram of the processing pipeline for the conversion of an RF ultrasound signal to a B-mode image [Barva (2007)]. One of these important steps is considered to be demodulation, which can be carried out by envelope detection in ultrasound processing. Therefore, from the analytic signal of RF ultrasound, the amplitude of the analytic signal can be calculated and it is used as the envelope of the RF signal. Usually, we calculate the analytic signal of 1D scan lines separately from the RF signal [Schlaikjer *et al.* (2003)] by the 1D Hahn AS modulus, then the amplitude of this 1D analytic signal can be obtained from its local amplitude.

Compared with separate 1D scan lines processing, we calculate the RF ultrasound volume all at once. The 3D CAS of the RF ultrasound volume is constructed, and then the modulus $|\psi_{bq}(x, y, z)|$ of Eq. (3.77) of the 3D CAS is used as an envelope of the

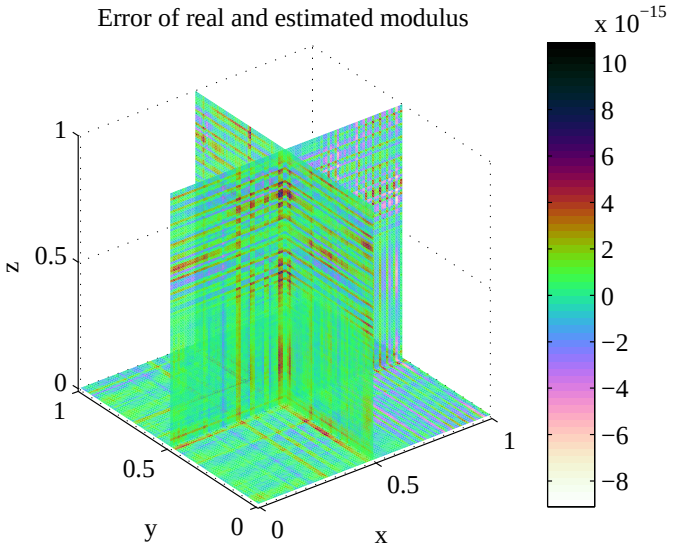

Figure 3.16: The error between the algebraical and numerical of the modulus of a 3D modulated signal.

ultrasound volume. Since the 3D CAS analyzes the information of the lateral, axial and elevation directions, this method provides improved envelope detection for the ultrasound volume.

The experiments were conducted with the ultrasound imaging platform at CREATIS Laboratory. The acquisition of the volume was carried out using an Ultrasonix MDP scanner and an ultrasound linear probe 4D motorized abdominal transducer: 4DC7-3/40 (Ultrasonix) with a 40-MHz sampling frequency. A biopsy needle was inserted into a homemade agar ultrasound phantom. The acquisition depth on this phantom was 50 mm, the width 88 mm, and the field of view was 45.6° for 33 slices. Figure 3.18 shows the platform of the ultrasound volume data acquisition. The size of the volume was $128 \times 1280 \times 33$ pixels in lateral, axial and elevation directions, respectively. Figure 3.19 illustrates the numerical calculation that corresponds to the acquisition platform of the ultrasound volume data in Fig. 3.18. The biopsy needle was inserted in the middle along the z-direction (elevation). Therefore, along the z-direction, we can take a slice around the middle of the ultrasound volume data, such as slice 15 (z index = 15).

We compared the 3D CAS envelope results with the 1D Hahn AS and 2D QS envelope detection results as shown in Fig. 3.20. To compare the results under the same reference, for all the envelope slices, the gray value of the slice images were normalized between minimum and maximum value of all three types of data. One slice of the total 33 slices along the elevation direction is presented. On slice 15 along z-direction, the profile on the envelope image from the 3D CAS shows the biopsy needle structure more clearly. The vertical profiles of the envelope from the 1D, 2D, and 3D methods are presented in Fig. 3.20(d). Moreover, the parallelograms in Fig. 3.20(a)–(c) indicate the position of the biopsy needle. In the parallelogram region, the profiles along the direction of the biopsy needle axis are

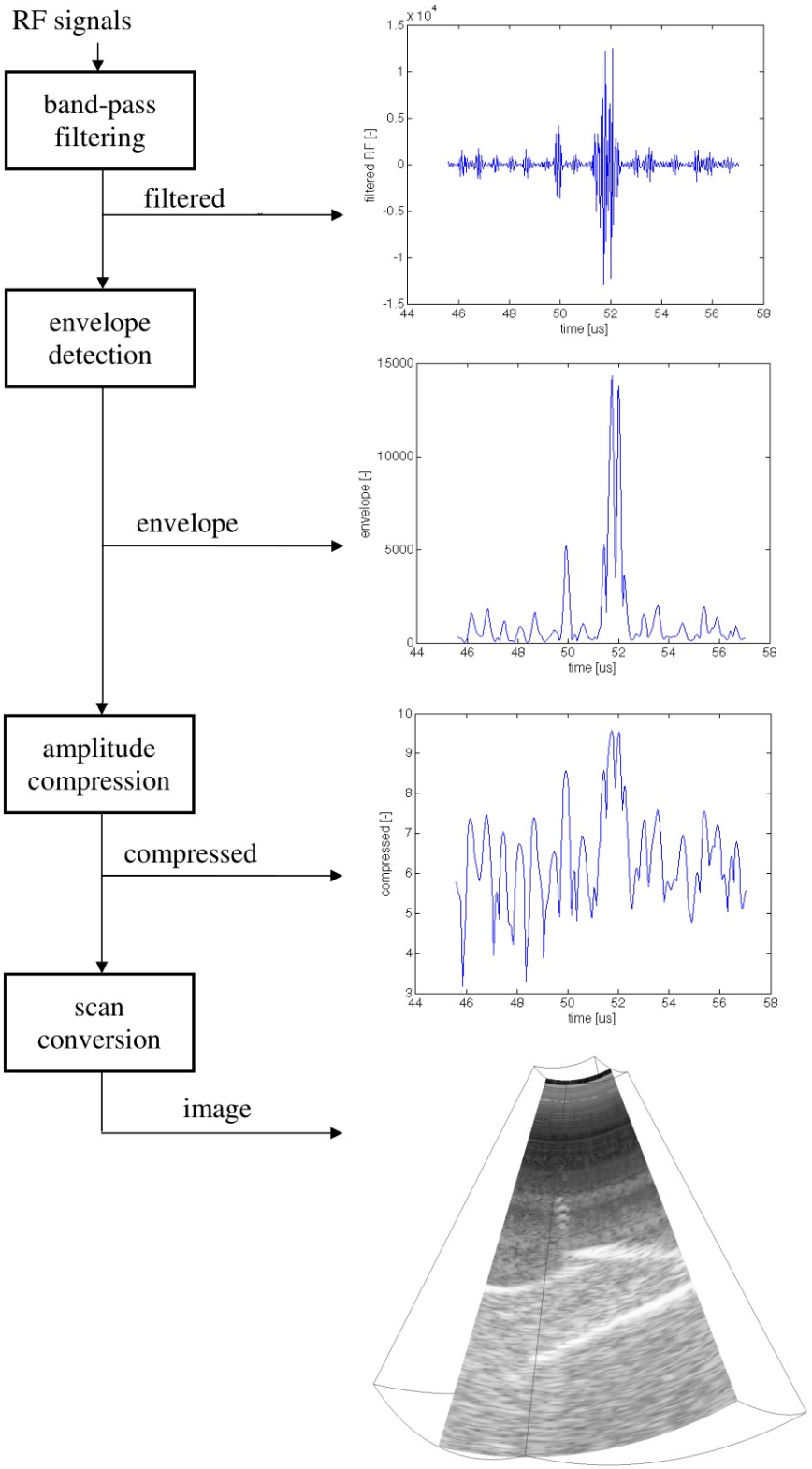

Figure 3.17: An example diagram of processing pipeline for the conversion of RF ultrasound signal into a B-mode image. Intermediate data are shown on the right side [Barva (2007)].

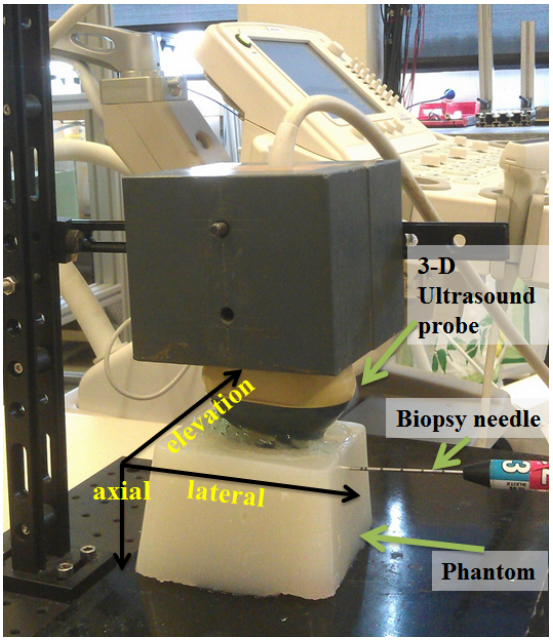

Figure 3.18: CREATIS experimental platform for RF ultrasound volume acquisition of a biopsy needle in a homemade agar ultrasound phantom.

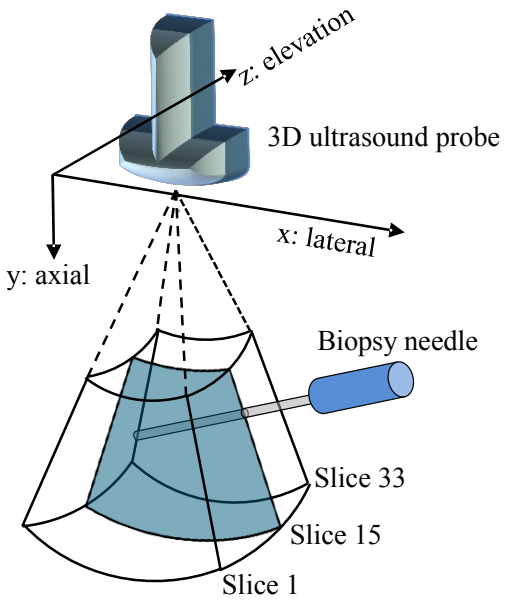

Figure 3.19: An illustration of the experimental platform. The biopsy needle is inserted into a plane around the middle of the 3D ultrasound volume around z-direction slice 15.

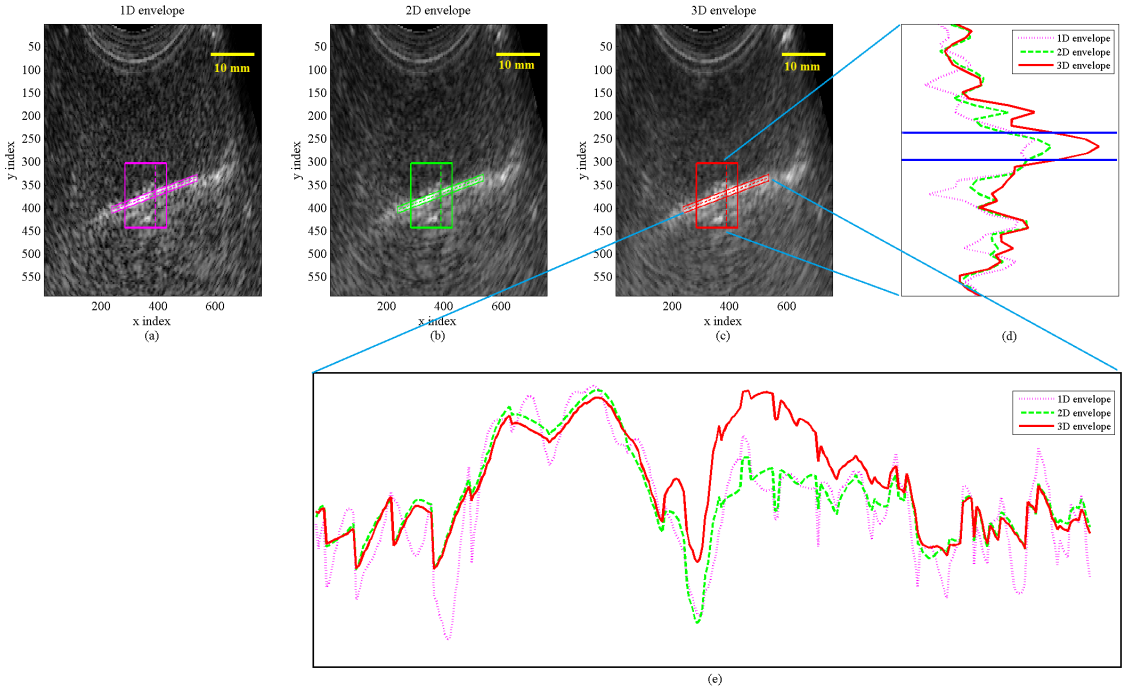

Figure 3.20: RF ultrasound filtered envelope comparison of a slice in elevation direction: (a) 1D Hahn envelope; (b) 2D QS envelope; (c) 3D CAS; (d) three vertical profiles of 1D, 2D, and 3D envelope in the same position; (e) three profiles along the biopsy needle axis of 1D, 2D, and 3D envelope at the same position.

presented in Fig. 3.20(e). From these profiles, the 3D CAS envelope result shows the biopsy needle position more clearly than the 1D and 2D envelopes. From the parallelogram region (the biopsy needle location), the envelope results show a contrast optimization of 8% and 6% compared with 1D and 2D envelope detection methods, respectively.

3.7 Conclusion

Based on 1D and 2D Hahn single-quadrant AS, 1D Hahn AS and 2D QS were discussed first. Then we demonstrated that both the 2D Hahn AS and 2D QS could be represented by the total and partial Hilbert transform of the original real signal, which means that there is a direct relation between 2D Hahn AS and 2D QS. Therefore, we presented how to compute the 2D QS by two 2D single-quadrant Hahn AS. Hence, we found that only the classic Fourier transform is needed to obtain the 2D QS without quaternion Fourier transformation.

After that, we proposed the 3D CAS, an extension of 2D QS in the framework of Clifford algebra. Next, we introduced the relation between the 3D CAS and four single-orthant 3D Hahn AS, and established a direct relation between them by the total and partial Hilbert transform of the original 3D real signal (see Eq. (3.73)). As result, with the tools of 3D classic Fourier transform, we were able to obtain the 3D CAS.

Finally, after presenting the cosine function as an introductory example, we applied this to the 3D CAS modulus, which was applied for a 3D envelope detection of a RF ultrasound volume. The results show that this application of the 3D CAS has advantages for RF ultrasound volume. We calculated the 1D, 2D, and 3D envelope for an RF ultrasound volume that was acquired from an ultrasound phantom with a biopsy needle inserted. Comparing the three types of envelope results, the 3D CAS envelope gives a more precise local feature image of the biopsy needle. This potentially improves the quality for applications such as image segmentation, detection, and registration.

Chapter 4

Analytic signal phase-based myocardial motion estimation on tagged MRI sequence by a bilinear model and motion compensation

4.1 Introduction

The mechanical status of the pathological heart can be assessed from the cardiac motion and strains evaluated in cardiac imaging. Among the different medical imaging modalities, echocardiography and cardiac magnetic resonance imaging (MRI) are the most widely used for cardiac motion estimation. In the technique of MR tagging, the cardiac tissue is marked with a grid of magnetically saturated tags. MR tagging consists in applying a prior radio frequency pulse sequence to perturb the magnetic moments in straight bands in space [Axel *et al.* (2005), Ibrahim (2011)]. On an imaging plane, this results in regular black stripes. To assess the motion in 2D or 3D, 2 to 3 sets of bands are applied orthogonally. Then a conventional cine sequence is applied during several cardiac cycles. The deformation of the tags follows that of the myocardium during the cardiac cycle. The quantification of the motion proceeds from the analysis of the deforming pattern in the sequence of tagged images.

To date, several methods have been proposed to estimate the motion from tagged MRI sequences [Axel and Dougherty (1989)] from prior semi-automatic tag pattern extrac-

tion [Guttman *et al.* (1994), O'Dell *et al.* (1995)] and optical flow-based techniques [Prince and McVeigh (1992)]. Spatial phase has been proposed as a measurement less prone to image intensity variations. Osman et al. introduced the harmonic phase (HARP) approach, which relies on the bandpass filtering of the tagged MR images in the Fourier domain [Osman *et al.* (1999), Dallal *et al.* (2012)]. In the SinMod approach introduced in [Arts *et al.* (2010)], the intensity distribution in the environment of each pixel is modeled as a summation of sine wavefronts, obtained from tuned 2D bandpass filters. The method is fast and has shown better robustness to noise than the reference HARP method [Arts *et al.* (2010)]. Alternatively, a new method has been developed based on the temporal conservation of the monogenic phase [Alessandrini *et al.* (2013)]. In that work, a coarse-to-fine B-spline scheme allows for the effective and robust computation of the displacement, and also a pyramidal refinement scheme helps to deal with large motions.

From the myocardial motion field, various further studies have been realized in order to extract motion-related information, such as myocardium segmentation [Dietenbeck *et al.* (2014)], local deformation [Kar *et al.* (2014), Oubel *et al.* (2012)], and local region tracking [Arif *et al.* (2014), Luo *et al.* (2014), Sun *et al.* (2011)]. For these information extraction methods, the key point is to estimate an accurate myocardium motion field.

Therefore, in this chapter, we focus on an accurate motion estimation method for myocardium tagged MR image sequences. The main contribution of this work is to propose a two dimensional (2D) phase-based motion estimation method. The specificities of the proposed approach are the following: The estimated motion vectors are locally controlled by a bilinear transformation; the motion field between each two successive images is refined iteratively; the local non-rigid motion model and the global motion compensation model provide an accurate motion field estimation.

The proposed method estimates the displacement between two images. It is based on two spatial phase images, provided by 2D analytic signals of tagged MR images. Firstly, the procedure of spatial phase extraction is introduced. Next, we describe the mathematical development of the proposed displacement/velocity analytical estimator, which is applied on the phase images. Then, we show how the local complexity of cardiac motion is taken into account by a local bilinear model. Finally, an iterative scheme is presented to achieve subpixel motion accuracy.

4.2 Spatial phases from 2D analytic signal

The multidimension extension of the 1D analytic signal (AS) can be found in the work on the 2D AS by Hahn [Hahn (1992)], the quaternion analytic signal (QS) of Bülow and Sommer [Bülow and Sommer (2001)], as well as the monogenic signal of Felsberg [Felsberg and Sommer (2001)]. Multidimensional ASs have different forms but are all based on direct extensions of the 1D, 2D, or n-dimensional Hilbert transform. A phase-based method has been proposed by Basarab [Basarab *et al.* (2009)] for the application of subsample shift estimation on ultrasound images, which has stable accuracy for the low sampled signal.

The 1D and 2D AS is introduced in chapter 2 and chapter 3. Let us recall that, an AS $\psi(x)$ of a real-value signal $f(x)$ contains the real part, which is the signal itself, and the imaginary part $H\{f(x)\}$, which is the Hilbert transform of $f(x)$:

$$\psi(x) = f(x) + i' f_H(x) = f(x) + i' f(x) \star \frac{1}{\pi x}, \tag{4.1}$$

where i' is the imaginary unit, and $\star$ denotes the convolution operator.

For a 2D real-valued signal $f(x, y)$ with Cartesian coordinates (x, y), the total and the partial Hilbert transforms are, respectively, defined by:

$$H\{f(x,y)\} = f(x,y) \star\star (\frac{1}{\pi^2 xy}), \tag{4.2}$$

$$H_x\{f(x,y)\} = f(x,y) \star (\frac{1}{\pi x}), \tag{4.3}$$

$$H_y\{f(x,y)\} = f(x,y) \star (\frac{1}{\pi y}), \tag{4.4}$$

where $\star$ and $\star\star$ are the 1D and 2D convolution products, respectively. These three Hilbert transforms may be further combined to form the 2D QS and the 2D AS. The 2D QS is defined as:

$$\psi_q(x,y) = f(x,y) + iH_x\{f(x,y)\} + jH_y\{f(x,y)\} + kH\{f(x,y)\}, \tag{4.5}$$

where i, j, k are the imaginary units with $ij = -ji = k, jk = -kj = i, ki = -ik = j$. Its polar form introduced by Bülow's definition is given in Eq. (4.6):

$$\psi_q(x,y) = |\psi_q(x,y)|\, e^{i\phi_i(x,y)} e^{k\phi_k(x,y)} e^{j\phi_j(x,y)}, \tag{4.6}$$

where $|\psi_q(x,y)|$ is the modulus of $\psi_q(x,y)$ and $(\phi_i(x,y),\ \phi_j(x,y),\ \phi_k(x,y))$ is called the phase of $\psi_q(x,y)$.

The 2D AS is composed of four single-quadrant complex signals respectively given as a function of total and partial Hilbert transforms of $f(x,y)$ by [Hahn (1992)],

$$\begin{aligned}\psi_1(x,y) &= (f(x,y) - H\{f(x,y)\}) + i'(H_x\{f(x,y)\} + H_y\{f(x,y)\}) \\ &= |\psi_1(x,y)|\, e^{i\phi_1(x,y)},\end{aligned} \tag{4.7}$$

$$\begin{aligned}\psi_2(x,y) &= (f(x,y) + H\{f(x,y)\}) + i'(-H_x\{f(x,y)\} + H_y\{f(x,y)\}) \\ &= |\psi_2(x,y)|\, e^{i\phi_2(x,y)},\end{aligned} \tag{4.8}$$

$$\begin{aligned}\psi_3(x,y) &= (f(x,y) + H\{f(x,y)\}) + i'(H_x\{f(x,y)\} - H_y\{f(x,y)\}) \\ &= |\psi_3(x,y)|\, e^{i\phi_3(x,y)},\end{aligned} \tag{4.9}$$

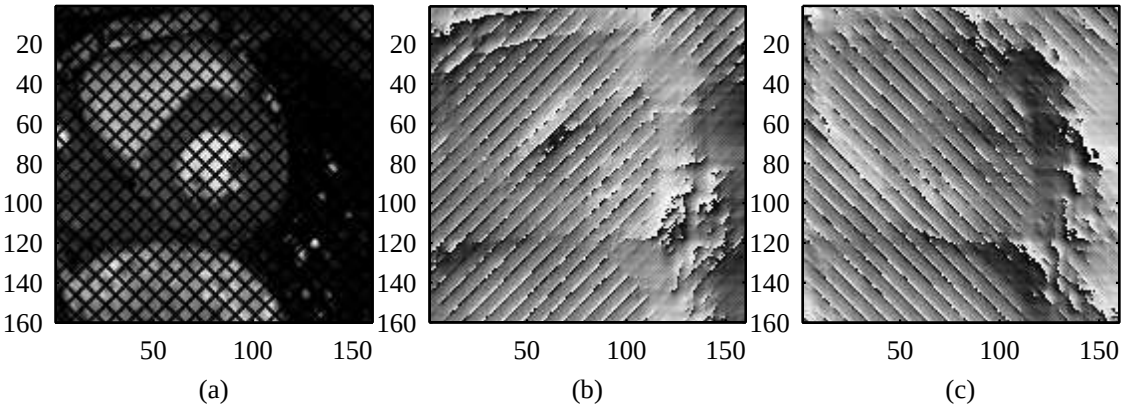

Figure 4.1: (a) Tagged MR image with 45° and 135° tagging lines. (b) Phase image ϕ_1 from analytic signal ψ_1, contains 45° tagging lines structural information. (c) Phase image ϕ_2 from analytic signal ψ_2, contains 135° tagging lines structural information.

$$\begin{aligned}\psi_4(x,y) &= (f(x,y) - H\{f(x,y)\}) + i'(-H_x\{f(x,y)\} - H_y\{f(x,y)\}) \\ &= |\psi_4(x,y)|\, e^{i\phi_4(x,y)},\end{aligned} \tag{4.10}$$

where i' is the imaginary unit, $|\psi_1(x,y)|$, $|\psi_2(x,y)|$, $|\psi_3(x,y)|$, $|\psi_4(x,y)|$ are the modulus, and $\phi_1(x,y)$, $\phi_2(x,y)$, $\phi_3(x,y)$, $\phi_4(x,y)$ are the phases of $\psi_1(x,y)$, $\psi_2(x,y)$, $\psi_3(x,y)$, $\psi_4(x,y)$, respectively.

For our 2D motion estimation problem, we have locally two unknown variables to estimate, which are the displacement/velocity along the horizontal and vertical directions. Since it is known that the phase is less sensitive to global changes in the intensity of the image, in order to solve the 2D motion estimation problem, the information of two suitable phases should be chosen from the QS phases in Eq. (4.6) and AS phases in Eqs. (4.7)-(4.10). Due to the 2D spectrum symmetry of the 2D Fourier transform of real images, ψ_1 together with ψ_2 (or ψ_3 with ψ_4) contains all the information of the original image. Moreover, these two spatial phases contain complementary information about the image structure. For example, in the tagged MR image of Fig. 4.1, the tagging lines along two directions constitute two sets of complementary structural information.

Although there exists a linear relation between the QS phases ϕ_i, ϕ_j and the AS phases $\phi_1, \phi_2, \phi_3, \phi_4$, while the QS phase ϕ_k is presented by the modulus of AS [Hahn and Snopek (2004),Hahn and Snopek (2011)], the QS phases do not split information in the two tagging line directions. This makes QS less suitable for calculating the spatial gradient of the phase needed in the next step of our method. Therefore, we use ϕ_1, ϕ_2 of ψ_1, ψ_2 in Eq. (4.7) and Eq. (4.8) as a basis for the myocardium displacement estimation in our method.

As part of the illustration, Figure 4.1 shows the spatial phases obtained via the AS ψ_1 and ψ_2, on a tagged MR image with tagging lines along the 45° and 135° directions. ϕ_1 holds the structural information of the 45° tagging lines, while ϕ_2 holds the ones of the 135° tagging lines. An example of the profile of phase ϕ_1 in a region of interest (ROI) of Fig. 4.1(b) is shown in Fig. 4.2.

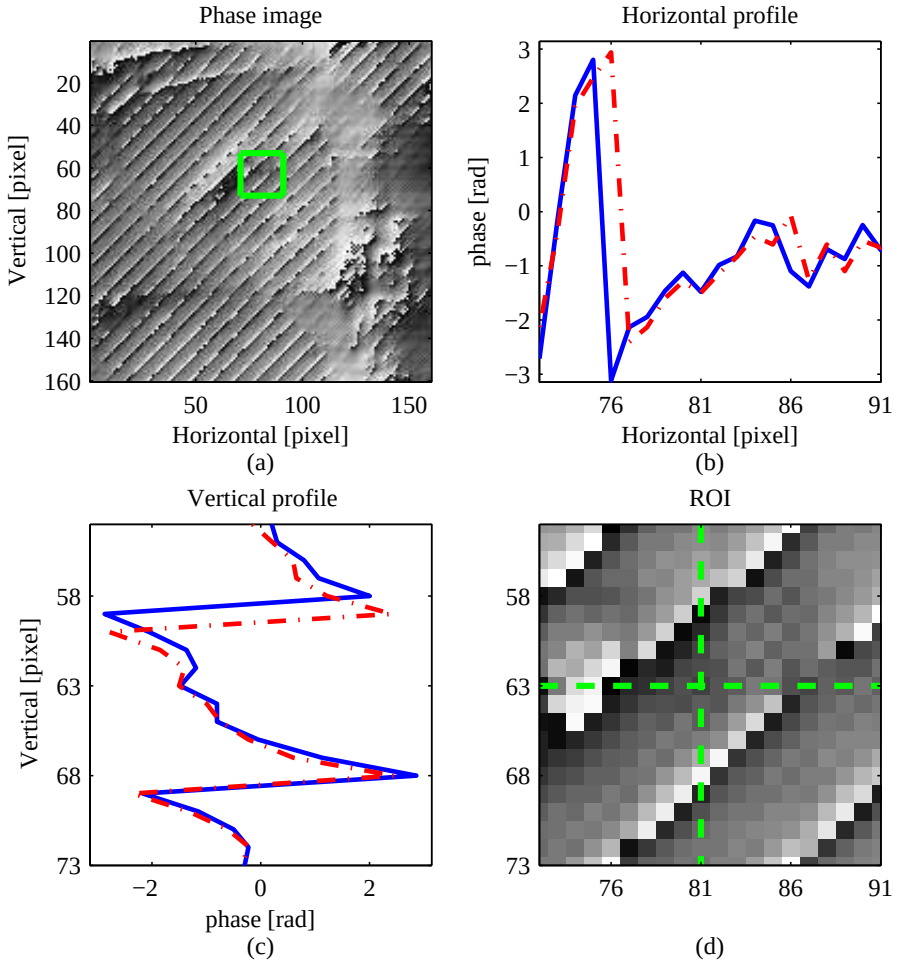

Figure 4.2: (a) Phase image ϕ_1 from analytic signal ψ_1 with an ROI in the green rectangle. (b) Horizontal profiles of two successive frames in ϕ_1 ROI in (d). (c) Vertical profile of two successive frames in ϕ_1 ROI in (d). (d) ROI (zoomed in) of ϕ_1 in (a) with horizontal/vertical profile lines (green dashed lines).

4.3 Optical flow method from the spatial phase images

The optical flow equation is largely used for motion estimation in various application domains. It is based on the assumption of pixel intensity conservation over time, and of small displacements between consecutive frames (typically smaller than 1 pixel). Based on these hypotheses and using a Taylor series development of order 1, the optical flow equation is written as:

$$\begin{aligned} i(x,y,t) &= i(x+d_x, y+d_y, t+d_t) \\ &= i(x,y,t) + d_x\frac{\partial i}{\partial x} + d_y\frac{\partial i}{\partial y} + d_t\frac{\partial i}{\partial t} + O(d_x^2, d_y^2, d_t^2) \\ \Leftrightarrow & d_x\frac{\partial i}{\partial x} + d_y\frac{\partial i}{\partial y} + d_t\frac{\partial i}{\partial t} = 0 \end{aligned} \tag{4.11}$$

where i is the intensity function of space (x, y) and time (t) variables, d_x and d_y the displacement of the pixel at position (x, y), d_t the temporal sampling step, and $O(d_x^2, d_y^2, d_t^2)$ is the higher-order term. In the following, without loss of generality, we use $d_t = 1$ in order to simplify the mathematical expressions.

In this section, we propose replacing the intensity invariance assumption by the phase over time. Thus, Eq. (4.11) is replaced hereafter by two equations holding on the two phases ϕ_1, ϕ_2 of AS ψ_1 and ψ_2:

$$d_x \frac{\partial \phi_1}{\partial x} + d_y \frac{\partial \phi_1}{\partial y} + \frac{\partial \phi_1}{\partial t} = 0, \tag{4.12}$$

$$d_x \frac{\partial \phi_2}{\partial x} + d_y \frac{\partial \phi_2}{\partial y} + \frac{\partial \phi_2}{\partial t} = 0. \tag{4.13}$$

Hence, dx, dy can be obtained by solving the previous system of two equations with two unknowns:

$$d_x = \frac{\frac{\partial \phi_1}{\partial y}\frac{\partial \phi_2}{\partial t} - \frac{\partial \phi_2}{\partial y}\frac{\partial \phi_1}{\partial t}}{\frac{\partial \phi_1}{\partial x}\frac{\partial \phi_2}{\partial y} - \frac{\partial \phi_1}{\partial y}\frac{\partial \phi_2}{\partial x}}, \tag{4.14}$$

$$d_y = \frac{\frac{\partial \phi_1}{\partial x}\frac{\partial \phi_2}{\partial t} - \frac{\partial \phi_2}{\partial x}\frac{\partial \phi_1}{\partial t}}{\frac{\partial \phi_1}{\partial y}\frac{\partial \phi_2}{\partial x} - \frac{\partial \phi_1}{\partial x}\frac{\partial \phi_2}{\partial y}}, \tag{4.15}$$

where $\frac{\partial \phi_1}{\partial x}$, $\frac{\partial \phi_2}{\partial x}$, $\frac{\partial \phi_1}{\partial y}$, $\frac{\partial \phi_2}{\partial y}$ are the spatial derivatives of ϕ_1 and ϕ_2 with respect to the spatial coordinates. The terms $\frac{\partial \phi_1}{\partial t}$ and $\frac{\partial \phi_2}{\partial t}$ are the temporal derivatives of the phases. They may be classically calculated by finite difference numerical differentiation. We propose, in order to avoid the phase jumps problem and possible errors of phase unwrapping, computing the temporal derivatives of the phases directly from the AS and its conjugates:

$$\frac{\partial \phi_1}{\partial t} = Arg[\psi_1^*(x, y, t) \cdot \psi_1(x, y, t+1)], \tag{4.16}$$

$$\frac{\partial \phi_2}{\partial t} = Arg[\psi_2^*(x, y, t) \cdot \psi_2(x, y, t+1)], \tag{4.17}$$

with ψ_1^* the conjugate of ψ_1, and ψ_2^* the conjugate of ψ_2. In the following, phases are computed using Eqs. (4.7) and (4.8) within local blocks extracted from tagged MR images and used to assess a local bilinear model.

4.4 Bilinear model of the local motion

Since the human myocardium has a relatively complex motion, the local displacement of myocardium cannot be estimated accurately by a simple rigid translation model. As a consequence, a more complex motion model is needed to approach local displacement better. In our method, we used a bilinear model consisting of translation, dilation, rotation, and motion components. Such a model has already been used, for instance, for tissue displacement estimation in ultrasound elastographic image sequences [Basarab *et al.*

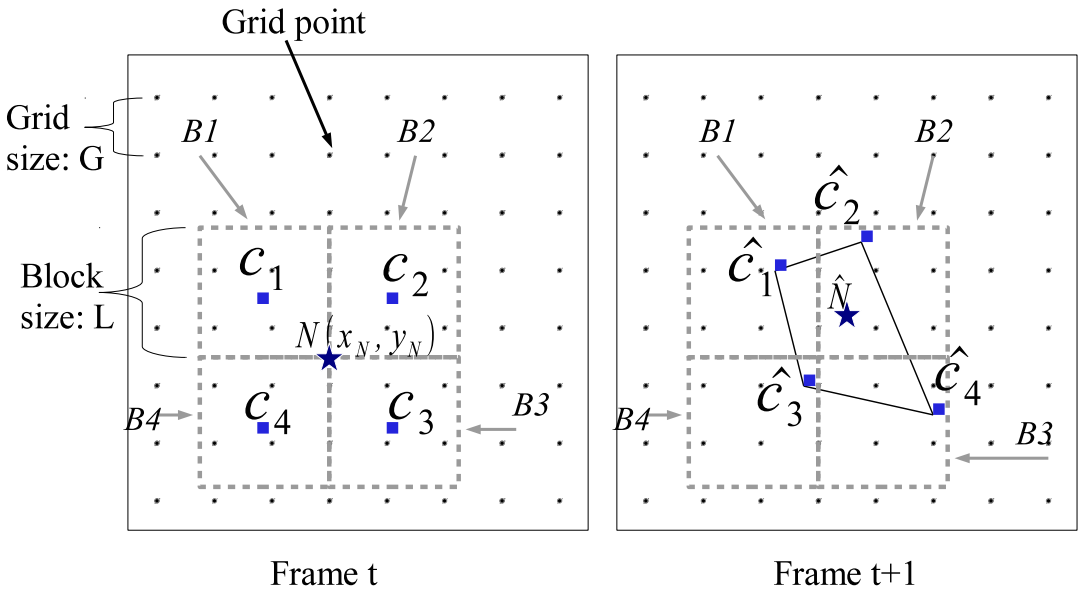

Figure 4.3: Displacement estimation between point $N(x_N, y_N)$ (star) on frame t and point $\hat{N}$ on frame t+1: Firstly, the displacement of four neighbor blocks $B1, B2, B3, B4$ of N are estimated separately, the average motion vector of each block is used as its center displacement from c_i to $\hat{c}_i$ (i=1,2,3,4). Next, the displacement of N to $\hat{N}$ is calculated by the bilinear model based on the position of $\hat{c}_1, \hat{c}_2, \hat{c}_3, \hat{c}_4$.

(2008)].

The basic principle is shown in Fig. 4.3. It illustrates how to calculate the displacement of the pixel $N(x_N, y_N)$ (star) between frame t and frame $t+1$. Let us define $B1, B2, B3, B4$ as the four blocks having in common the pixel N, and C_1, C_2, C_3, C_4 the centers of the blocks $B1, B2, B3, B4$. By applying Eqs. (4.7) and (4.8) on block Bi, we get its AS ψ_{1B}, ψ_{2B} and the phases ϕ_{1B}, ϕ_{2B}. Substituting into Eqs. (4.14), (4.15), we obtain the two displacement components $(d_x(C), d_y(C))$:

$$d_x(C) = \frac{\frac{\partial\phi_{1B}}{\partial y}\frac{\partial\phi_{2B}}{\partial t} - \frac{\partial\phi_{2B}}{\partial y}\frac{\partial\phi_{1B}}{\partial t}}{\frac{\partial\phi_{1B}}{\partial x}\frac{\partial\phi_{2B}}{\partial y} - \frac{\partial\phi_{1B}}{\partial y}\frac{\partial\phi_{2B}}{\partial x}}, \tag{4.18}$$

$$d_y(C) = \frac{\frac{\partial\phi_{1B}}{\partial x}\frac{\partial\phi_{2B}}{\partial t} - \frac{\partial\phi_{2B}}{\partial x}\frac{\partial\phi_{1B}}{\partial t}}{\frac{\partial\phi_{1B}}{\partial y}\frac{\partial\phi_{2B}}{\partial x} - \frac{\partial\phi_{1B}}{\partial x}\frac{\partial\phi_{2B}}{\partial y}}, \tag{4.19}$$

with $\frac{\partial\phi_{1B}}{\partial t} = Arg[\psi_{1B}(x,y,t)\cdot\psi^*_{1B}(x,y,t+1)]$, and $\frac{\partial\phi_{2B}}{\partial t} = Arg[\psi_{2B}(x,y,t)\cdot\psi^*_{2B}(x,y,t+1)]$. Therefore, we obtain the displacements $[d_x(C_1), d_y(C_1)]$, $[d_x(C_2), d_y(C_2)]$, $[d_x(C_3), d_y(C_3)]$, and $[d_x(C_4), d_y(C_4)]$ from blocks $B1$, $B2$, $B3$, and $B4$, respectively. The displacement $[d_x(N), d_y(N)]$ of grid point $N(x_N, y_N)$ can be calculated by the four displacements of point C_1, C_2, C_3, and C_4 as below. For this, the eight parameters of the bilinear model

are estimated as follows:

$$\begin{pmatrix} a_x \\ b_x \\ c_x \\ d_x \end{pmatrix} = M \begin{pmatrix} d_x(C_1) \\ d_x(C_2) \\ d_x(C_3) \\ d_x(C_4) \end{pmatrix}, \qquad \begin{pmatrix} a_y \\ b_y \\ c_y \\ d_y \end{pmatrix} = M \begin{pmatrix} d_y(C_1) \\ d_y(C_2) \\ d_y(C_3) \\ d_y(C_4) \end{pmatrix}, \tag{4.20}$$

where the matrix M depends on the block size L in Fig. 4.3:

$$M = \frac{1}{2} \begin{pmatrix} -\frac{1}{L} & \frac{1}{L} & \frac{1}{L} & -\frac{1}{L} \\ -\frac{1}{L} & -\frac{1}{L} & \frac{1}{L} & \frac{1}{L} \\ \frac{2}{L^2} & -\frac{2}{L^2} & \frac{2}{L^2} & -\frac{2}{L^2} \\ \frac{1}{2} & \frac{1}{2} & \frac{1}{2} & \frac{1}{2} \end{pmatrix}. \tag{4.21}$$

Then, the displacement of point $N(x_N, y_N)$ is obtained by:

$$d_x(N) = a_x x_N + b_x y_N + c_x x_N y_N + d_x, \tag{4.22}$$

$$d_y(N) = a_y x_N + b_y y_N + c_y x_N y_N + d_y. \tag{4.23}$$

The detailed procedure is introduced in [Basarab *et al.* (2008)]. Finally, the dense motion field is calculated by linear interpolation from the displacement of the grid points. In order to improve the estimation accuracy, a global refining method is proposed in the following.

4.5 Refined model

For two successive images i_t and i_{t+1}, an initial estimation of the displacement field (d_x^0, d_y^0) is obtained as described in the previous section:

$$\left[d_x^0(x,y), d_y^0(x,y)\right] = \Delta\left[i_t(x,y), i_{t+1}(x,y)\right], \tag{4.24}$$

where Δ is the motion estimator described in section 4.4. Based on this motion field and the first image $i_t(x,y)$, an inter-frame $\hat{i}_{t+1}^1(x,y)$ is generated by:

$$\hat{i}_{t+1}^1(x,y) = i_t\left(x + d_x^0(x,y), y + d_y^0(x,y)\right), \tag{4.25}$$

where the new position of the pixel (x_0, y_0) in $i_t(x,y)$ is $[x_0 + d_x^0(x_0,y_0), y_0 + d_y^0(x_0,y_0)]$ and each pixel value of $\hat{i}_{t+1}^1(x,y)$ is obtained by spline interpolation.

Ideally, the generated image $\hat{i}_{t+1}^1(x,y)$ and the image $i_{t+1}(x,y)$ should contain the same phase information. However, in practice, this is not true because of motion estimation errors. Therefore, a compensated motion field $[d_{xc}^1(x,y), d_{yc}^1(x,y)]$ is estimated between image $\hat{i}_{t+1}^1(x,y)$ and $i_{t+1}(x,y)$ by the same bilinear phase-based method proposed in

section 4.4:

$$\left[d^1_{xc}(x,y), d^1_{yc}(x,y)\right] = \Delta\left[\hat{i}^1_{t+1}(x,y), i_{t+1}(x,y)\right]. \tag{4.26}$$

Then, the estimated motion field $[d_x(x,y), d_y(x,y)]$ between two successive images i_t and i_{t+1} with improved accuracy is obtained by:

$$d_x(x,y) = d^0_x(x,y) + d^1_{xc}(x,y), \tag{4.27}$$
$$d_y(x,y) = d^0_y(x,y) + d^1_{yc}(x,y). \tag{4.28}$$

This process can be iterated a number of times leading to the iterative scheme:

$$d^k_x(x,y) = d^{k-1}_x(x,y) + d^k_{xc}(x,y), \tag{4.29}$$
$$d^k_y(x,y) = d^{k-1}_y(x,y) + d^k_{yc}(x,y), \tag{4.30}$$

with k the iteration number ($k \geqslant 1$). This iteration procedure is part of step 2 of Algorithm 1 (see section 5.1). With this iterative scheme, a more accurate motion field $[d_x(x,y), d_y(x,y)]$ is obtained, that enables us to get a desired estimation result.

4.6 Lagrangian motion estimation

The Lagrangian motion field represents the spatial displacement of material points in the reference state (first frame) along time. This spatio-temporal Lagrangian displacement field $[u_L(x,y), v_L(x,y)]$ can be recovered through forward integration of the Eulerian motion field $[d_x(x,y), d_y(x,y)]$. For a motion field between time t and $t+1$, we calculate the Lagrangian motion field $[u_L(x,y,t+1), v_L(x,y,t+1)]$ from the Lagrangian motion field $[u_L(x,y,t), v_L(x,y,t)]$ at time t and the Eulerian motion field $[d_x(x,y,t+1), d_y(x,y,t+1))]$ at time $t+1$:

$$u_L(x,y,t+1) = u_L(x + d_x(x,y,t+1), y + d_y(x,y,t+1), t), \tag{4.31}$$
$$v_L(x,y,t+1) = v_L(x + d_x(x,y,t+1), y + d_y(x,y,t+1), t), \tag{4.32}$$

with the initial conditions $u_L(x,y,1) = d_x(x,y,1)$, $v_L(x,y,1) = d_y(x,y,1)$. A bilinear interpolation is applied on the four neighbor points of the current point to calculate the motion field $u_L(x + d_x(x,y,t+1), y + d_y(x,y,t+1), t)$ and $v_L(x + d_x(x,y,t+1), y + d_y(x,y,t+1), t)$.

The Lagrangian motion field enables us to compute the strain and to track local regions. The myocardial strain is one major indicator for cardiac function diagnosis [Qian *et al.* (2011)], which can be computed from spatial derivatives of the Lagrangian accumulated motion field $\mathbf{u} = [u_L(x,y,t), v_L(x,y,t)]$ with respect to time. The Green-Lagrange strain tensor is defined as:

$$\mathbf{E} = \frac{1}{2}\left(\nabla\mathbf{u} + \nabla\mathbf{u}^T + \nabla\mathbf{u}^T\nabla\mathbf{u}\right), \tag{4.33}$$

where ∇ is the spatial derivative operator and $\mathbf{u}^T$ is the transpose of $\mathbf{u}$. In addition, the radial deformation E_{rr} along direction $\mathbf{r}$ and circumferential deformation E_{cc} along direction $\mathbf{c}$ can be obtained by:

$$E_{rr} = \mathbf{r}^T \mathbf{E} \mathbf{r}, \quad E_{cc} = \mathbf{c}^T \mathbf{E} \mathbf{c}. \tag{4.34}$$

Furthermore, given a point x_0, y_0, the Lagrangian material point trajectory at time t of this point $T(x_0, y_0, t)$ is:

$$T(x_0, y_0, t) = [x_0 + u_L(x_0, y_0, t), y_0 + v_L(x_0, y_0, t)]. \tag{4.35}$$

The myocardial strain and local region tracking can provide a visual information of the motion field. Several simulation and clinical results are presented in the next chapter.

4.7 Conclusion

We have proposed in this chapter a motion estimation method for tagged MRI sequences based on the 2D single quadrant AS phases and optical flow method. In the proposed method, the local bilinear model and a global refining method are employed on the optical flow motion field, improving the accuracy of displacement estimation in tagged MRI myocardium sequences. Hence, the displacement between two successive images is obtained. By applying the proposed method on a sequence, we presented the accumulated Lagrangian displacement computation, with post-processing of the Lagrangian displacement. In order to better understand the performance of this method, several evaluations are realized on both synthetic data and clinical data.

Chapter 5

Simulation and clinical results of phase-based myocardium motion estimation method

The proposed estimation algorithm in the previous chapter is evaluated on both synthetic and clinical data. Both the Eulerian and Lagrangian displacement cases [Ricco and Tomasi (2012)] are discussed in the evaluation, which correspond, respectively, to two successive frame displacement and accumulated displacements (the points trajectory over time). The endpoint error [Fleet and Jepson (1990)] is used for Eulerian displacement evaluation. Additionally, from the Lagrangian motion field, we present the myocardium deformation and local region tracking results. The Green-Lagrange strain tensor [Belytschko *et al.* (2013)] is used to calculate the radial and circumferential deformation [Petitjean *et al.* (2005)]. Then, for two clinical cases with cardiac pathologies, the myocardium deformation and local region tracking results are presented and discussed.

5.1 Algorithm implementation

The pseudo-code of the proposed motion estimation method between two consecutive images is given in Algorithm 1.

Algorithm 1 Phase-based Bilinear block and Compensation Optical Flow

Input: two subsequent frames: $i_t(x,y), i_{t+1}(x,y)$.
parameter: G, L, kMax.
G: Grid distance for bilinear model in pixels on horizontal and vertical direction.
L: Block size for bilinear model in pixels on horizontal and vertical direction.
kMax: Maximum iteration number.
Output: Displacement $[d_x(x,y), d_y(x,y)]$ between $i_t(x,y)$ and $i_{t+1}(x,y)$.

Step 1:
for (x,y) = grid points coordinate on frame i_t **do**
  for each of the four neighbour block of the current grid point **do**
    $[s_{1B}(t), s_{2B}(t), \phi_{1B}(t), \phi_{2B}(t)]$ = BlockAS($B(t)$).
    $[s_{1B}(t+1), s_{2B}(t+1), \phi_{1B}(t+1), \phi_{2B}(t+1)]$ = BlockAS($B(t+1)$).
    {Eqs. (4.7),(4.8).}
    $[d_x(C), d_y(C)]$ = PhaseOpticalFlow$(s_{1B}, s_{2B}, \phi_{1B}, \phi_{2B})$.
    {Eq. (4.19).}
  end for
  $[d_x(N), d_y(N)]$=BilinearModel($[d_x(\mathbf{C}), d_y(\mathbf{C})]$). {Compute the displacement of the current grid point N.}
end for
$\left[d_x^0(x,y), d_y^0(x,y)\right]$=DenseMotion($[d_x(N), d_y(N)]$). {Interpolation on all the grid point N to obtain dense motion field}
Step 2:
$d_x^{k-1}(x,y) = d_x^0(x,y), d_y^{k-1}(x,y) = d_y^0(x,y)$
{initialize for refining interation k.}
for k=1:$kMax$ **do**
  {$kMax$ is the maximum iteration number}
  $\hat{i}_{t+1}^k$=ObjectFrameGeneration$(d_x^{k-1}, d_y^{k-1}, i_t)$. {Eq. (4.25).}
  $[d_{xc}^k, d_{yc}^k]$=CompensatedDisplacement$(\hat{i}_{t+1}^k, i_{t+1})$.
  {Repeat **Step 1** by Eq. (4.26).}
  $d_x^k = d_x^{k-1} + d_{xc}^k, d_y^k = d_y^{k-1} + d_{yc}^k$ {Eq. (4.27).}
end for
$d_x(x,y) = d_x^{kMax}(x,y), d_y(x,y) = d_y^{kMax}(x,y)$

5.2 Simulated data

The proposed method was tested on different realistic tagged MRI sequences corresponding to a cardiac cycle, simulated with ASSESS software [Clarysse *et al.* (2011)]. With this simulator, a combination of thickening and rotations simulates the contraction over time within a short-axis MRI slice. It is also possible to introduce a local motion anomaly by reducing the myocardium contraction magnitude within a myocardial sector [Clarysse *et al.* (2000)]. Therefore, the ground truth motion data were used as a reference to evaluate the proposed method. Several simulations were generated by acting on the simulator parameters. Each simulation term in Table 5.1 can be interpreted as follows: "256" or "160" for the resolution of each square frame in pixels, "D20" for contraction/expansion of 20%, "R20" for 20-degree rotation, "F20" or "F34" for frame number of 20 or 34, and "P0" for healthy or "P3" for pathological state with the highest

degree of the myocardial motion abnormality.

5.3 Robustness of phase

In order to evaluate the robustness of our method, we also generated a sequence imposing a non respect of the pixel intensity conservation over time, named "160D30R20P3F34Lum" in table 5.1. In each image of the sequence, we changed its intensity to a random percentage value between 40% and 100% of the original intensity. In order to modify the intensity of each image of the sequence, we multiplied the original image by a 2D weighting image $(a + (1 - a)G(x, y))$, with $G(x, y)$ the Gaussian function. The range of the 2D weighting image is $(a, 1]$, where a is a random real value limited in $[0.4, 1]$. As the consequence, we obtain a sequence with the pixel intensity between 40% and 100% of the original image intensity. Here we chose the minimum value $a = 0.4$ for the purpose of retaining at least 40% intensity of the original images.

The sequence intensity changes locally in each frame due to the Gaussian function and also changes along the time axis due to the random value a. Given an original image i_1, the output image i_2 obtained by the 2D weighting image $(a + (1 - a)G(x, y))$ is:

$$i_2(x, y) = (a + (1 - a)G(x, y))i_1(x, y), \tag{5.1}$$

where $G(x, y) = exp\left(-\frac{(x-x_0)^2+(y-y_0)^2}{2\sigma^2}\right)$, with (x_0, y_0) and σ the center peak position and the standard deviation of $G(x, y)$, respectively. We vary the center peak position (x_0, y_0) linearly along the time axis, which changes the brightest region on each frame in the sequence. Figure 5.1 shows an example: each pixel value of the image in Fig. 5.1(b) is obtained from the corresponding pixel value of image in Fig. 5.1(a) multiplied by the corresponding value of 2D weighting image in Fig. 5.1(e). Figures 5.1(c) and (d) are one of the phases of Fig. 5.1(a) and (b), respectively. We note that both phase images hold the structural information and are less influenced by their varied intensity images.

5.4 Existing methods used for comparison

Taking into account the fact that the proposed method is based on the analytic signal and optical flow principles (more precisely on the phase flow), the evaluation results of an analytic signal estimator and optical flow estimator are presented for comparison purposes.

The first one is the Alessandrini monogenic signal method for the analysis of heart motion from medical images [Alessandrini *et al.* (2013)]. It outperforms the SinMod method [Arts *et al.* (2010)] and was shown to be more accurate with less computation than another algorithm based on the monogenic signal [Zang *et al.* (2007)].

The second method used for comparison is called Sun classic NL in [Sun *et al.* (2010)]. It was declared the best optical flow algorithm in 2010 in the Middlebury evaluation ranking [Baker *et al.* (2007), Baker *et al.* (2011)] (used for the evaluation of optical

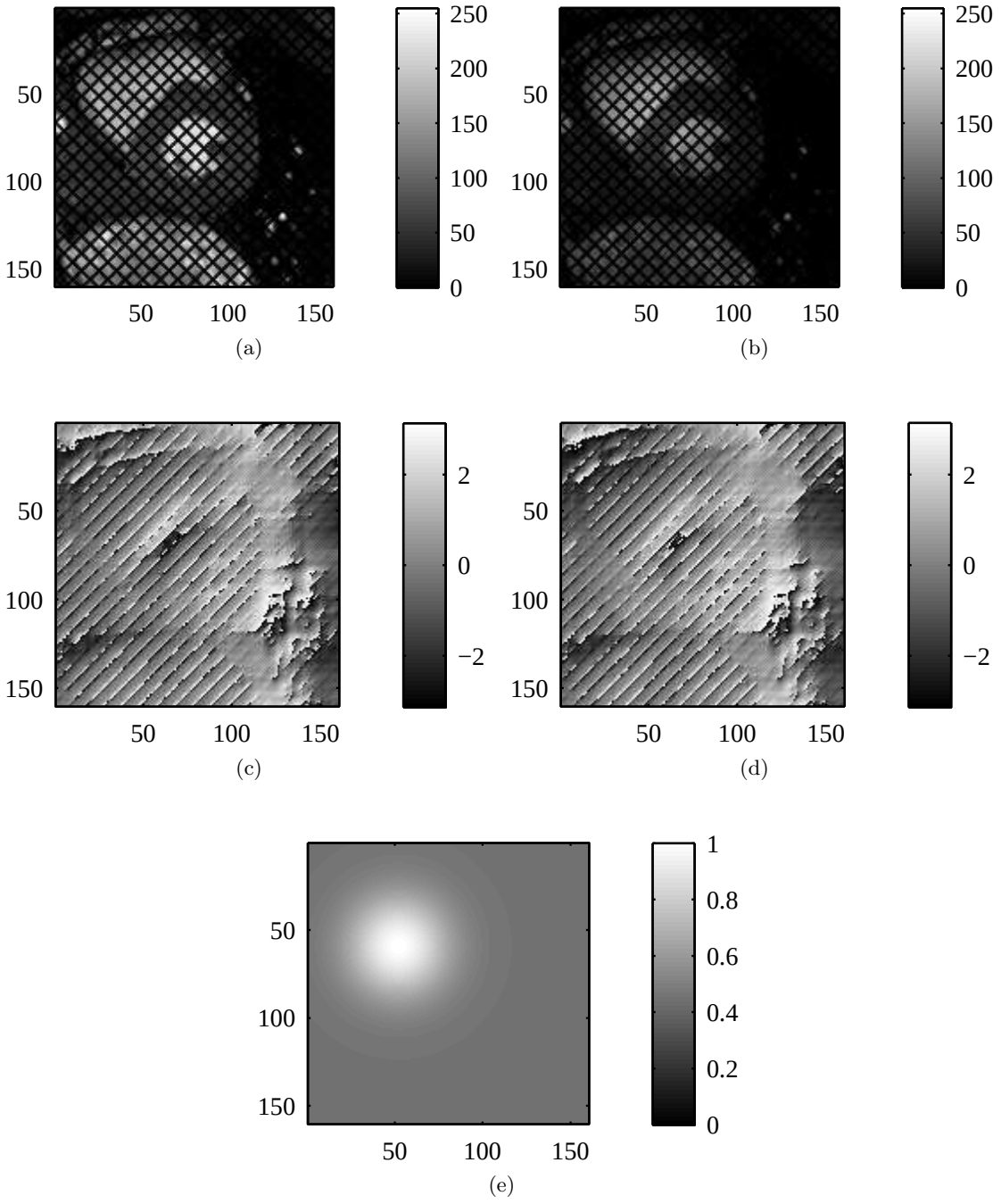

Figure 5.1: (a) A tagged MR image. (b) Modified intensity image of (a) by weighting image (e). (c) The phase of (a). (d) The phase of (b). (e) 2D weighting image from the Gaussian function($\sigma = 20$, $(x_0, y_0) = (59, 52)$, $a = 0.45$). The phase images (c) and (d) contain almost the same structural information as the different intensity image (a) and (b).

flow algorithms), and in an expanded literature review in 2014 [Sun *et al.* (2014)]. This method was also reported to provide good results in the new optical evaluation datasets in 2012 such as KITTI [Geiger *et al.* (2012)] (autonomous driving platform to develop

new benchmarks for the tasks of stereo, optical flow, and 3D object detection) and MPI Sintel [Butler *et al.* (2012)] (new optical flow data set derived from the open source 3D animated short film Sintel). Hence, these two algorithms could be considered as suitable references.

5.5 Evaluation criteria

Angular error (AE) and endpoint error (EE) are common criteria used to evaluate the difference between the theoretical and estimated displacements [Otte and Nagel (1994)]. However, AE is less suitable for small displacements [Alessandrini *et al.* (2013)] and the EE is a more appropriate measure of displacement vector accuracy [Baker *et al.* (2011)]. Hence, we used EE to evaluate the estimation accuracy. The EE at one location is defined as:

$$EE(x,y) = \sqrt{(d_x(x,y) - d_{xr}(x,y))^2 + (d_y(x,y) - d_{yr}(x,y))^2}, \tag{5.2}$$

where $[d_{xr}(x,y), d_{yr}(x,y)]$ are the ground truth reference displacements along horizontal and vertical directions, respectively, and $[d_x(x,y), d_y(x,y)]$ are the estimated ones. The averages and standard deviations of EE for both Eulerian and Lagrangian displacements are computed to quantify the performance of the method. The EE values obtained for several simulation sequences results are presented and discussed in the following sections.

5.6 Method parameters

The parameters for all the methods are determined based on the sequences in table 5.1. With the proposed method, for the bilinear model, the grid distance is 4×4 pixels and the block size is 10×10 pixels. Two refinement iterations appear as a good trade-off between EE and computing time. We computed the motion field for all the seven simulated sequences, then obtained an average of these seven sequences' EE, which equals 0.055, 0.042, 0.039, 0.037 pixels, respectively, corresponding to iteration number 1, 2, 3, 4.

Moreover, the computing time to finish calculating all the seven sequences (80 images of 256×256 pixels and 102 images of 160×160 pixels) is 18.59, 27.87, 37.18, 46.54 minutes, respectively, corresponding to the iteration number 1, 2, 3, 4. With the Alessandrini method, the optimized parameters proposed in [Alessandrini *et al.* (2013)] are used, which are the initial wavelength $\lambda_0 = 4$ and the refinement step number $N_p = 5$. For the Sun classicNL method, we adopted the parameters recommended in [Sun *et al.* (2010)], which are the sobel edge detector with a mask of 5×5 pixels and a neighborhood of 15×15 pixels.

Sequence	Endpoint Error [pixels]		
	Proposed	Alessandrini	Sun ClassicNL
(1)256R20F20	**0.050±0.055**	0.087±0.064	0.089±0.082
(2)256D30F20	**0.015±0.013**	0.035±0.025	0.036±0.034
(3)256D30R20P0F20	**0.063±0.066**	0.094±0.069	0.092±0.090
(4)256D30R20P3F20	**0.062±0.065**	0.099±0.075	0.097±0.095
(5)160D30R20P0F34	**0.035±0.027**	0.045±0.025	0.048±0.038
(6)160D30R20P3F34	**0.034±0.025**	0.041±0.022	0.045±0.035
(7)160D30R20P3F34Lum	**0.037±0.026**	0.042±0.022	0.049±0.037

Table 5.1: Eulerian average endpoint error ($\mu \pm \sigma$) in pixels on seven simulated sequences

Sequence	Computing time [minutes]		
	Proposed	Alessandrini	Sun ClassicNL
(1)256R20F20	5.00	0.48	15.95
(2)256D30F20	5.00	0.52	13.43
(3)256D30R20P0F20	5.02	0.70	16.08
(4)256D30R20P3F20	5.02	0.68	16.03
(5)160D30R20P0F34	2.68	0.57	13.10
(6)160D30R20P3F34	2.58	0.58	13.52
(7)160D30R20P3F34Lum	2.57	0.58	14.73

Table 5.2: The computing time on seven simulated sequences

5.7 Eulerian motion estimation results

5.7.1 Global results for all simulation sequences

Table 5.1 shows the EE results for the seven simulated sequences. For each sequence, we calculate a spatial average EE value μ and the standard deviation σ.

All the methods were implemented in MATLAB (R2012b, The Math-Works, Natick, MA), on a laptop computer (CPU: Intel i7-4750HQ 2.0GHz, RAM: 16384MB). Table 5.1 and table 5.2 show our results compared with the Alessandrini and Sun classicNL methods. Based on the summation of EE results of the seven sequences, the errors of the proposed method are reduced by 33% and 35% compared with that of the Alessandrini's and Sun's methods, respectively. On the variable intensity sequence "160D30R20P3F34Lum" and the constant intensity sequence "160D30R20P3F34," the proposed method provides a robust estimation. Besides, the proposed method is about 28% faster that Sun's method while providing a better motion estimation result. Although the Alessandrini method is outperformed by the proposed method, it is less time-consuming than the two other approaches.

Figure 5.2 presents a frame-by-frame EE comparison through box and whiskers plots for three sequences. These sequences present different kinds of motions: pure rotation of sequence "256R20F20", pure contraction/expansion of sequence "256D30F20", and rotation+contraction/expansion+deformation of sequence "160D30R20P3F34". The sequences "256R20F20" and "256D30F20" contain 7 frames in the systolic and 13 frames in the diastolic phase of one cardiac cycle. The sequence "160D30R20P3F34" contains 14

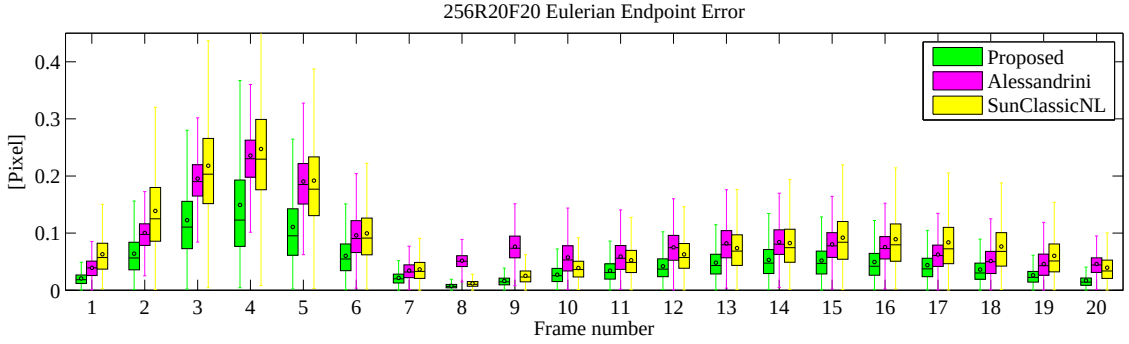

(a)

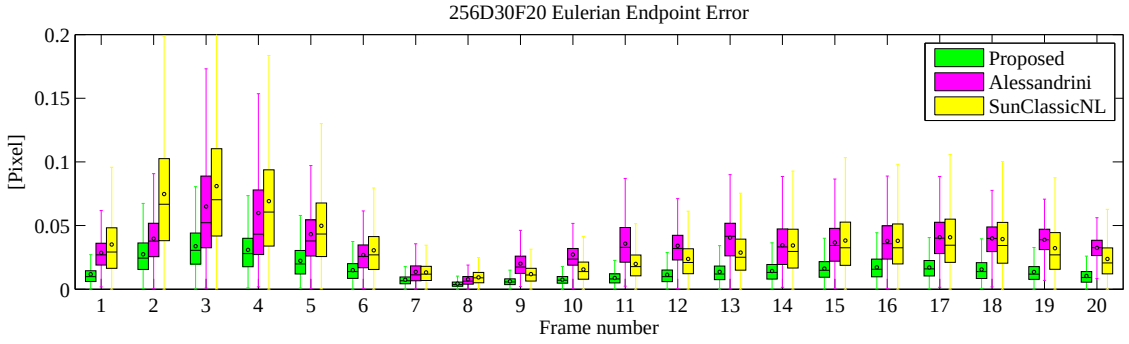

(b)

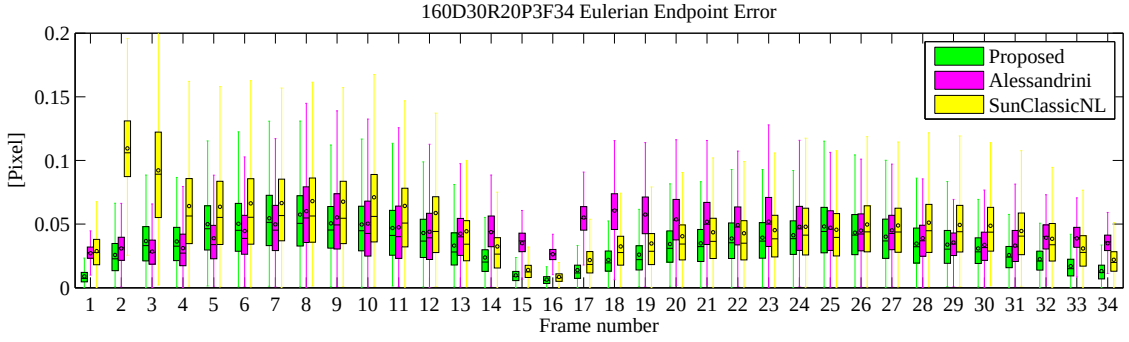

(c)

Figure 5.2: Box and whiskers plots of Eulerian endpoint errors for sequences (a) "256R20F20", (b) "256D30F20", (c) "160D30R20P3F34." Each box corresponds to the statistical distribution of all EE values on one frame. The center bar of each box represents the median value. The circle indicates the average value, and the box body extends from the 25th to the 75th percentile of one frame of EE values.

and 20 frames in the systolic and diastolic phase, respectively.

In Fig.5.2(a) and Fig.5.2(b), it is clear that during the systolic phase (frame 1 to 7), which corresponds to the larger displacements and also the diastole phase (frame 8 to 20), the estimation results of the proposed method are much better than the other two methods. We obtain the smallest end point error on each frame from the proposed method. In Fig.5.2(c), during the systolic phase (frame 1 to 14), we obtain better estimation results

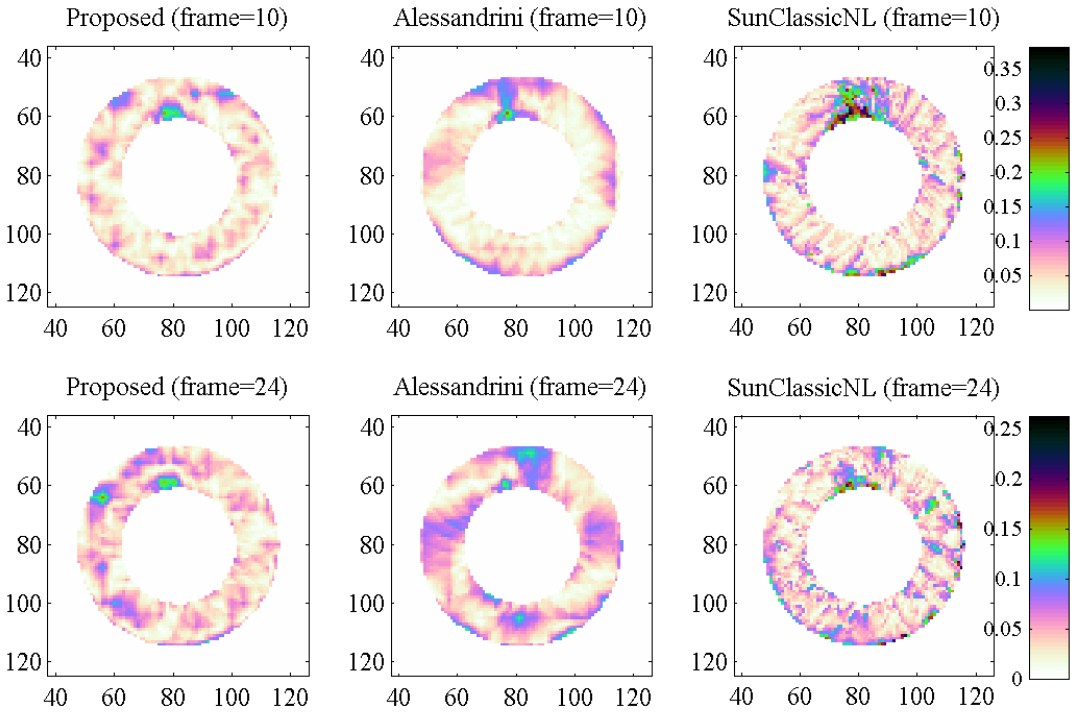

Figure 5.3: EE results of three methods (unit: pixels). First row: systolic frame 10. Second row: diastolic frame 24. First column: proposed method. Second column: Alessandrini method. Third column: Sun classicNL method.

with the proposed method than with the Sun classicNL method and almost equivalent estimation results as the Alessandrini method. At the beginning of the diastolic phase, the proposed method provides similar performance as the Sun classicNL method. In the diastole (frame 16 to 34), the proposed method is more accurate than the other two methods. Especially, in the frames where the displacement is relatively small, the proposed method outperforms the Alessandrini method at the frames 16 to 23, and it also outperforms the Sun classicNL method at frames 27 to 34.

5.7.2 Detailed EE results from one test case sequence

Performances of the three methods were studied in detail on sequence "160D30R20P3F34", which presents one cardiac cycle represented by 14 frames in the systolic and 20 frames in the diastolic phase. Figure 5.3 compares the EE results between the three methods on a systolic frame and a diastolic frame. In the systolic frame result (first row), the proposed method generates smaller error values. In the diastolic frame result (second row), there is no very clear observable difference between the three methods.

To better understand the performance of the methods, it is important to analyze vertical and horizontal displacement separately. Accordingly, Fig. 5.4 presents these results at frame 10, which has one of the largest displacements of two successive frames during the cardiac cycle. The ground truth motions are in the first row; the proposed method results, Alessandrini results, and Sun classicNL results are displayed in the second, third

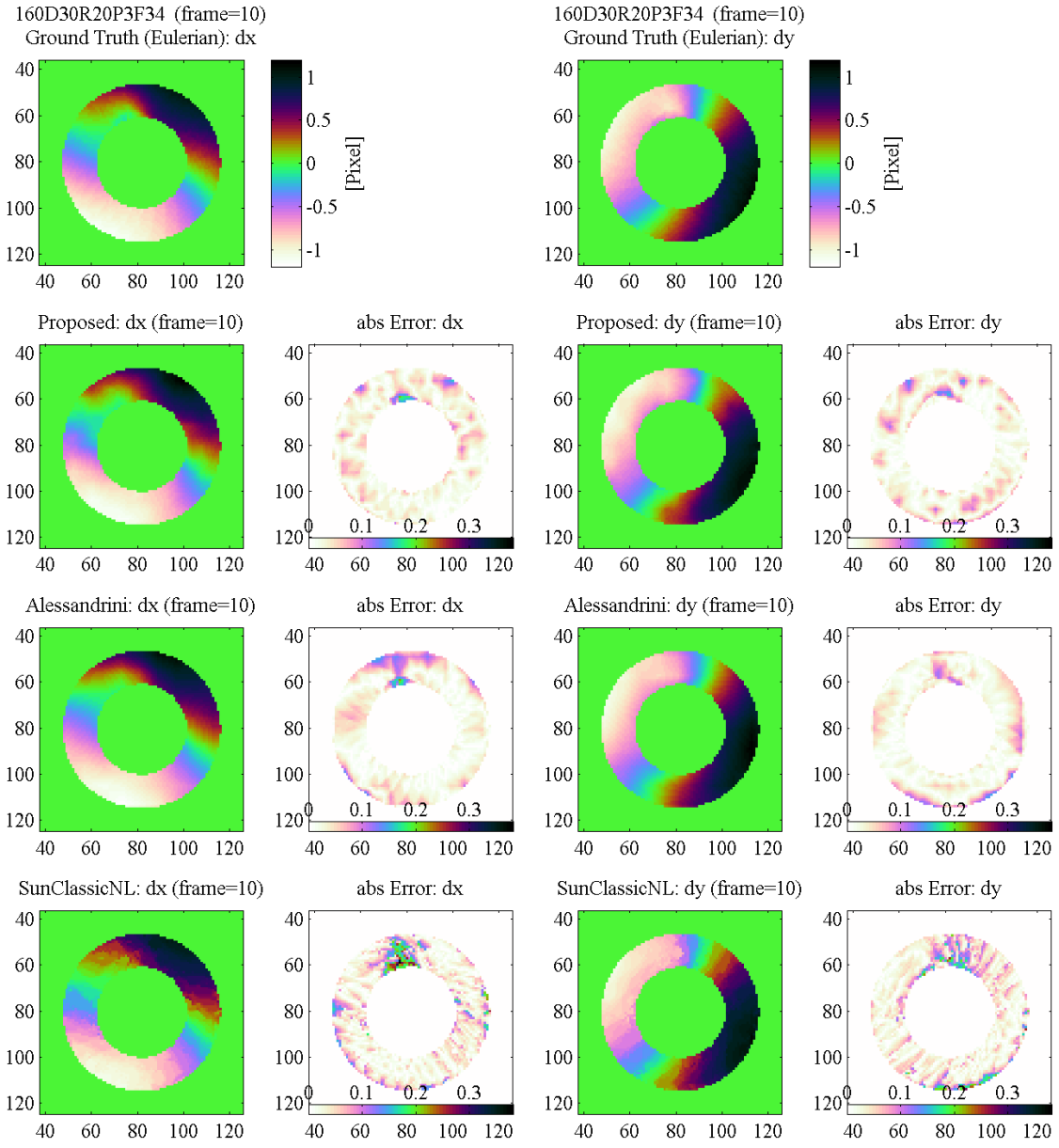

Figure 5.4: Displacement and absolute value error map in pixels of sequence "160D30R20P3F34" for three motion estimation methods. The horizontal displacement in pixels and its error are in the first column and second column, respectively. The vertical displacement in pixels and its absolute error are in the third and fourth columns, respectively. First row: the ground truth. Second row: the proposed method. Third row: Alessandrini method. Fourth row: Sun classicNL method.

and fourth rows, respectively. d_x indicates the horizontal displacement (first column) with its absolute error map beside (second column). d_y represents the vertical displacement (third column) with its absolute error map on the right (fourth column). The comparison of the absolute error in the second and third row highlights that the EE map is slightly smaller in magnitude for our method as compared to the Alessandrini method. Also, the proposed method error is much smoother than the Sun classicNL method error.

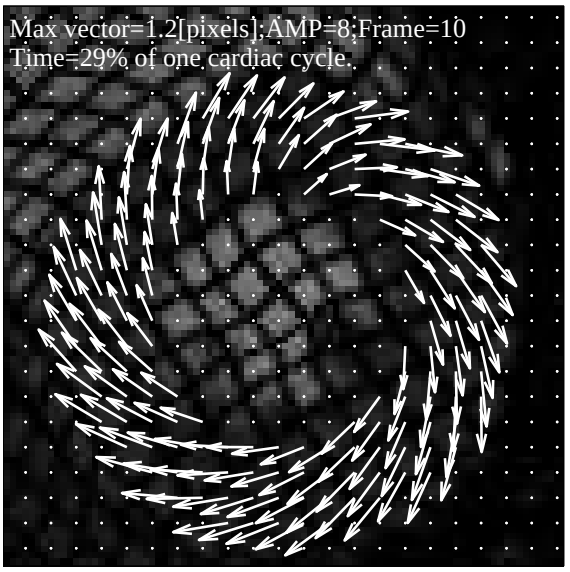

(a)

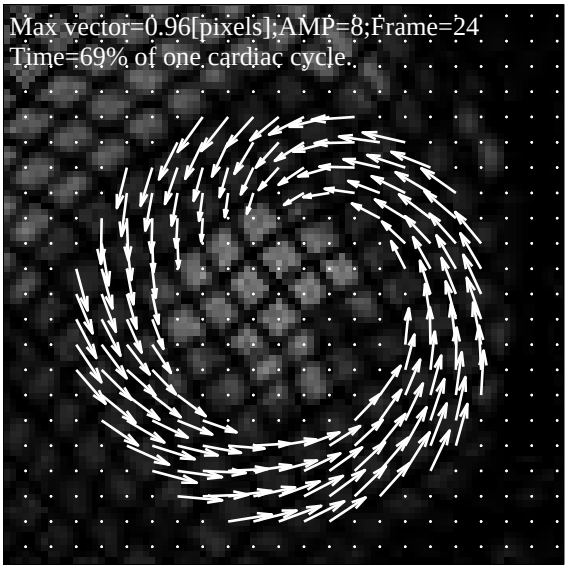

(b)

Figure 5.5: The Eulerian estimated motion vectors of sequence "160D30R20P3F34" from the proposed method. (a) Frames 10 from systole. (b) Frame 24 from diastole. Motion vectors are amplified by a factor of 8. The cardiac time of each frame is presented in terms of the percentage of a whole cardiac cycle.

Figure 5.5 presents frames 10 and 24 extracted from sequence "160D30R20P3F34" of one cardiac cycle with a superposition of the Eulerian motion vector estimated within the frames 10–11 and 24–25. The frames 10 and 24 belong, respectively, to systole and diastole phases, with a corresponding cardiac time in terms of the percentage value of one cardiac cycle period. These motion vectors vary for each frame, thus allowing for a local observation of the movement within the myocardium.

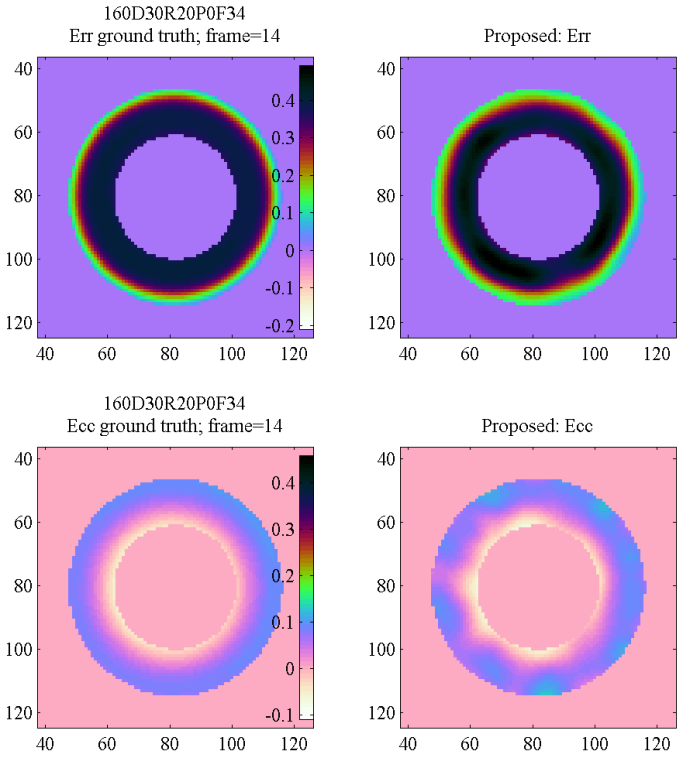

Figure 5.6: Estimated systolic myocardial strains in healthy case sequence. First row: radial deformation E_{rr}. Second row: circumferential deformation E_{cc}. First column: the ground truth. Second column: the proposed method results.

5.8 Lagrangian motion estimation results

As discussed in section 4.6, the Lagrangian motion field $[u_L(x, y, t), v_L(x, y, t)]$ at time t are obtained from the forward integration of the Euler motion field $[d_x, d_y]$. Then, let us recall the definition in Eq. (4.34), that the radial deformation E_{rr} along direction $\mathbf{r}$ and circumferential deformation E_{cc} along direction $\mathbf{c}$ are computed from spatial derivatives of the Lagrangian motion field $\mathbf{u} = [u_L(x, y, t), v_L(x, y, t)]$:

$$E_{rr} = \mathbf{r}^T \mathbf{E} \mathbf{r}, \tag{5.3}$$

$$E_{cc} = \mathbf{c}^T \mathbf{E} \mathbf{c}, \tag{5.4}$$

where $\mathbf{E}$ is the Green-Lagrange strain tensor defined in Eq. (4.33).

In the simulated sequences "160D30R20P0F34" and "160D30R20P3F34," the systolic (from frame 1 to end-systolic frame 14) radial and circumferential strains were computed. Figure 5.6 shows the myocardial deformation at frame 14 of sequence "160D30R20P0F34." The uniformity of deformation is observable in this healthy case from both the ground truth and proposed method results.

Figure 5.7 shows the radial and circumferential strains for the pathological case (sequence "160D30R20P0F34"). The four columns are in the order of the ground truth, the proposed method result, the Alessandrini result, and the Sun classicNL result. A simu-

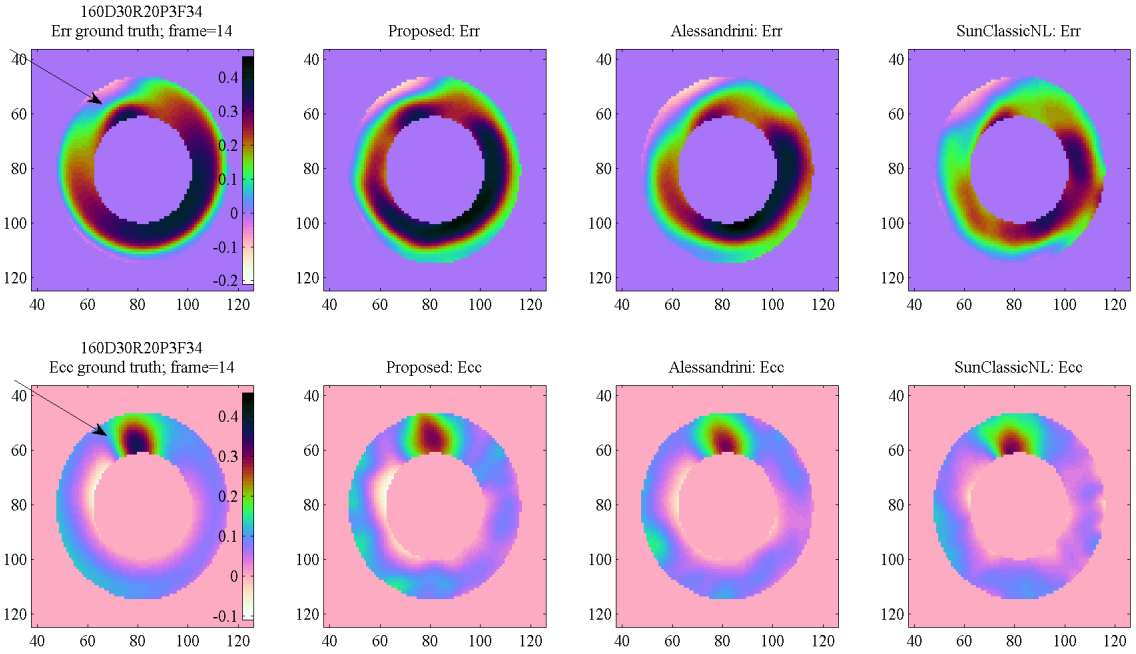

Figure 5.7: Estimated systolic myocardial strains for the pathological case sequence "160D30R20P3F34". First row: radial deformation E_{rr}. Second row: circumferential deformation E_{cc}. The four columns are in the order of the ground truth, the proposed method result, Alessandrini result, and Sun classicNL result, receptively.

lated pathology region is located in the upper left region of the myocardium (indicated by an arrow in the figure). From the radial deformation results E_{rr}, all three methods can recover the pathology, while from the circumferential deformation results, our proposed method obtains a more accurate pathology location than the other two methods.

5.9 Clinical results

In this section, we applied our method to in vivo clinical sequences of pathological cases from a female patient (43 years old) and a male patient (65 years old).

5.9.1 Pathological case #1

This 43 year-old female acute myocardial infarction (AMI) patient was hospitalized with a left anterior descending (LAD) occlusion, with a reperfusion performed H+2. MR imaging was performed 5 days after reperfusion. The standard cardiovascular magnetic resonance (CMR) examination contained MR tagging and post-Gadolinium injection (10 minutes) with a 3D inversion-recovery gradient echo sequence. MR tagging was performed on a Siemens Avento 1.5T in short-axis and long-axis views with the following parameters: gradient echo (GRE) sequence with 45° spatial modulation of magnetization (SPAMM) tagging pattern, TE=1.39 ms, TR=26.4 ms, flip angle=20°, tag spacing=6 mm, spatial resolution=1×1 mm, 21 frames, temporal resolution=30 ms.

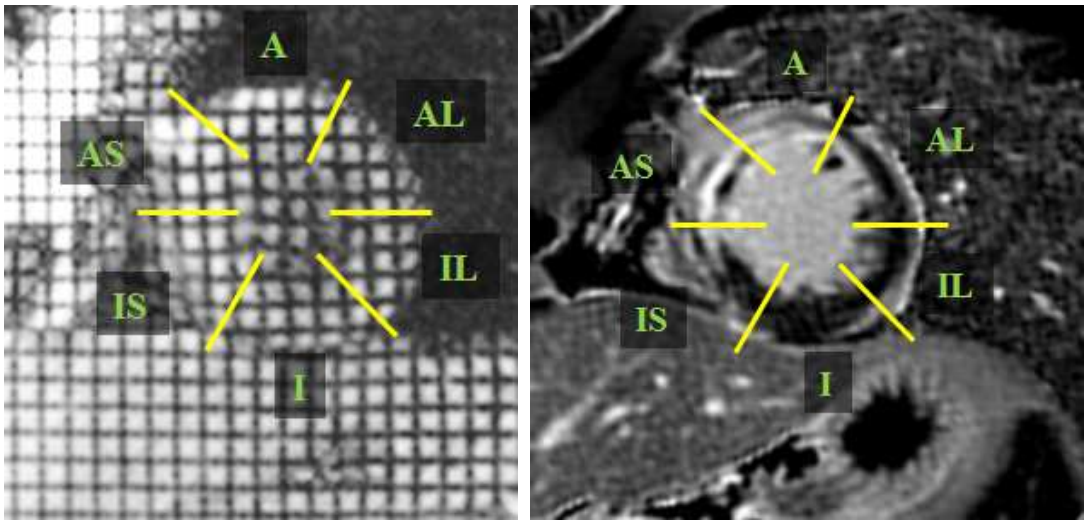

(a) (b)

Figure 5.8: Selected images of patient #1. (a) Short-axis tagged MR image. Frame 1 (end-diastolic phase) of this sequence that was used to estimate the motion field. (b) Image of LGE sequence with an area (edema in hypersignal) in the A, AS, and IS segments. A indicates anterior; AS, anteroseptal; IS, inferoseptal; I, inferior; IL, inferolateral; AL, anterolateral.

Figure 5.8(a) shows the first frame (end-diastolic phase) of a short-axis tagged slice located between the mid and apical level of the left ventricle. The myocardium is divided following the American Heart Association (AHA) segmentation [Cerqueira *et al.* (2002)]. Figure 5.8(b) shows the Late Gadolinium Enhancement (LGE) image at the same slice level. AMI appears as hyper-enhanced regions (AS, A, and IS segments) with dark regions in the sub-endocardial layers corresponding to no-reflow regions.

Applying the proposed method to this clinical tagged MRI sequence, the Lagrangian motion field is obtained by accumulating the Eulerian motion field. Figure 5.9 represents the Lagrangian motion field and the radial deformation (E_{rr}) at frame 13 (end-systole, corresponding to the maximum contraction). In Fig. 5.9(a), the amplitude of the movement in the A, AS, and IS segments are visibly smaller than in the AL, IL, and I segments, which is obviously in concordance with the location of the pathology. Due to the myocardial thickening during systole, radial strain is usually positive in normal myocardium. Figure 5.9(b) shows the reduced, and even negative, E_{rr} values in the pathological anterior region.

Lagrangian material point trajectories are displayed in Fig. 5.10. They provide a visual experience of the myocardium local motion trace. Several locations are chosen on the first image of the sequence as the desired tracking points. From the short-axis image in Fig. 5.10(a), we highlight clearly that during the cardiac cycle, the AS segment has decreased motion than other segments in adjacent or remote myocardium. In addition, in long-axis view shown in Fig. 5.10(b), we also illustrate a decrease of motion in the

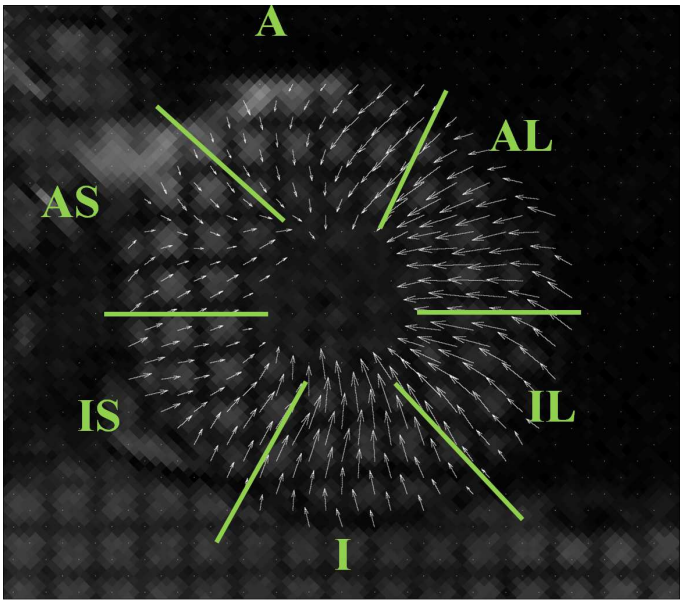

(a)

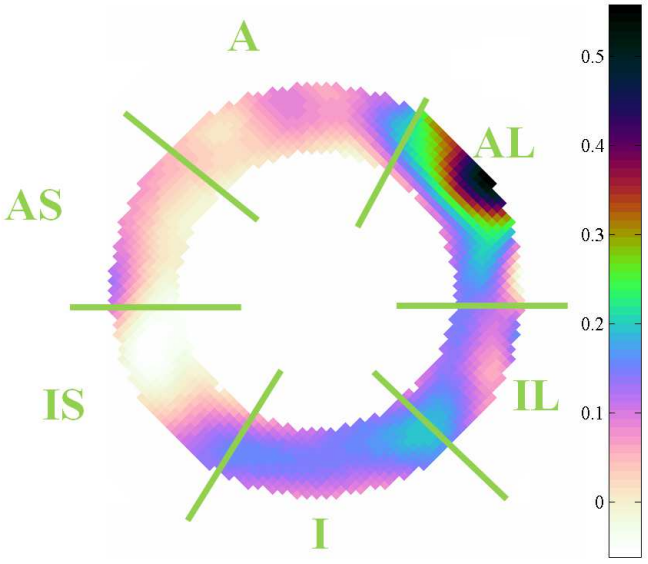

(b)

Figure 5.9: (a) Lagrangian motion field at end-systole frame 13 (with 1.5 magnification factor). (b) Radial strain E_{rr} at end-systole. The white regions (with reduced and negative values) in the A, AS and IS segments are matching the location of infarcted segments.

anteroapical, apical and infer-apical segments (in the white dashed circle). The white line shows the cross-location of the short axis view in Fig. 5.10(a). Hence, these tracking results are able to give an alternative illustration of the pathologies.

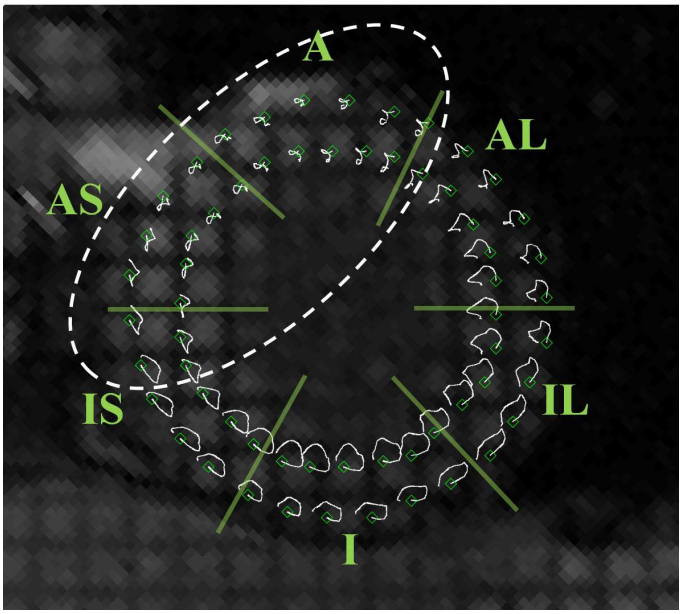

(a)

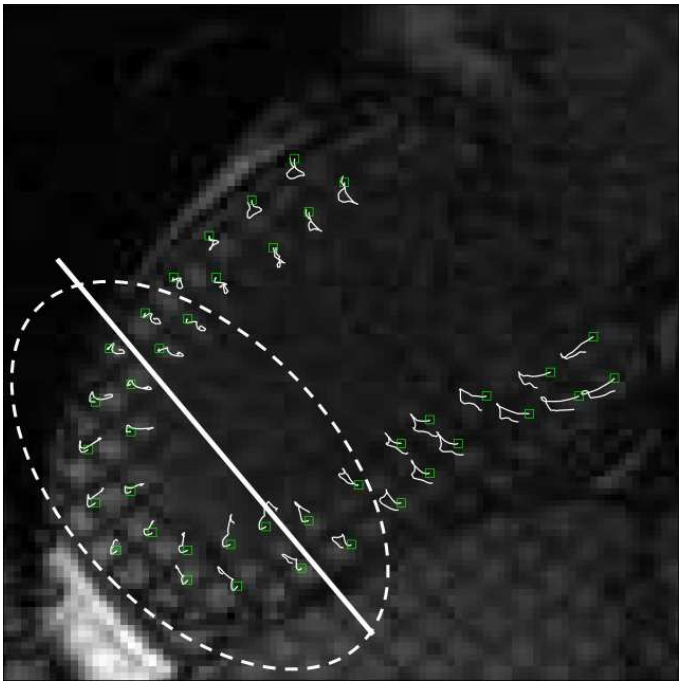

(b)

Figure 5.10: MR tagging-based material point trajectories for patient #1. (a) Short-axis view, note the reduced magnitude of motion in infarcted regions in the white dashed circle as compared to adjacent and remote regions. (b) Long-axis view, a white line indicates the position of the short axis plane in (a). The white dashed circle delineates the regions with decreased motion in this antero-septo-apical infarction.

5.9.2 Pathological case #2

This second clinical case illustrates an inferior AMI in a 65 year-old male (right coronary occlusion - reperfusion H+5). Imaging was performed before discharge of the patient at day 5. A short-axis tagged MRI was performed on a Siemens Avento 1.5T with the following parameters: GRE sequence with 45° SPAMM tagging pattern, TE=1.53 ms, TR=36.4 ms, flip angle=20°, tag spacing=6 mm, spatial resolution=1×1 mm, 21 frames, temporal resolution=36.4 ms.

Figure 5.11(a) shows the end-diastolic frame of the short-axis tagged MR sequence at the mid level of the left ventricle. Figure 5.11(b) shows the LGE image at the same slice level as the tagged image in Fig. 5.11(a). Abnormal segments corresponding to myocardial necrosis are including the IS, I, and IL segments, with again, presence of no-reflow (sub-endocardial hyposignal) in the I and IL segments.

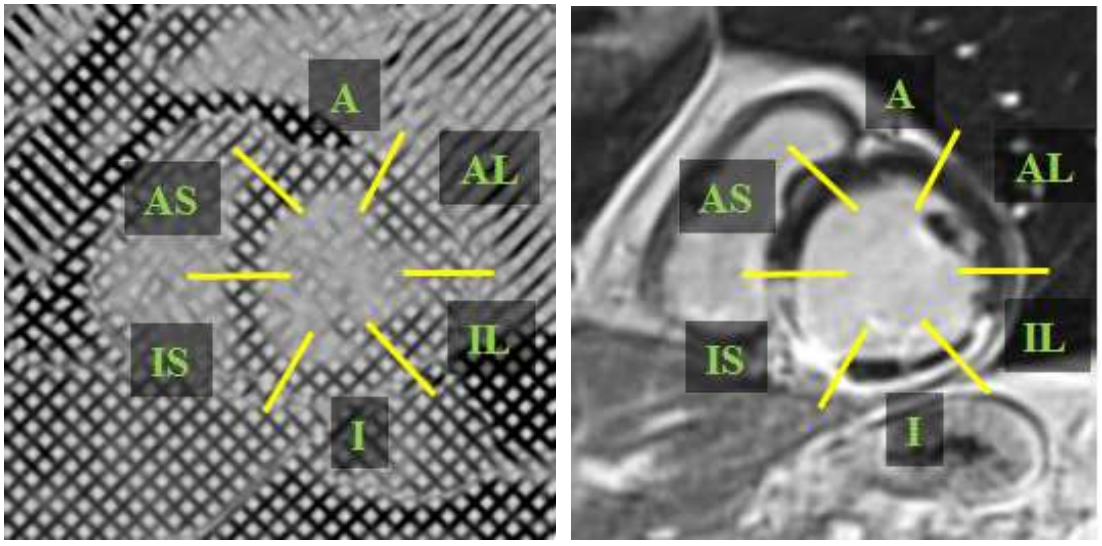

(a) (b)

Figure 5.11: Selected images of patient #2. (a) Short-axis tagged MR image. Frame 1 (end-diastolic phase) of this sequence that was used to estimate the motion field. (b) Corresponding slice of the LGE sequence showing an inferior infarction (hyper-enhanced regions) with no-reflow segments.

The estimated end-systolic motion field in Fig. 5.12(a) shows that the myocardium is almost divided in two parts: the upper one (anterior) with a centripetal movement of normal amplitude, and the inferior wall with a major decrease of amplitude. The radial strain map in Fig. 5.12(b) illustrates also the contrast between anterior and inferior parts of the circumference of the myocardium. In the IS, I, and IL segments, most of the negative deformation values and small positive values can be found in the lower part of the myocardium.

The Lagrangian material point trajectories in Fig. 5.13(a) give a global view of the whole sequence along time. In the remote anterior regions A and AL segments (mostly),

traces are smooth and large in amplitude. In the abnormal segments delineated with the dashed circle, traces are twisted and short, which demonstrate the lack of contractile capabilities in this acutely infarcted regions. In order to better highlight the difference between the healthy and pathological myocardial region tracking results, Fig. 5.13(b) presents the tracking results of a healthy myocardium from a male volunteer. We can see from this healthy case that all the tracked points have uniform contraction and dilation motions, which are different from the motion behavior of the pathological cases.

5.10 Conclusion

The performance of the proposed motion estimation method in chapter 4 is evaluated in several types of simulated sequences. Compared with two other effective methods (Alessandrini and Sun classicNL), the proposed method leads to a notable reduction of estimation errors. Moreover, the proposed method is less sensitive to both the pixel intensity variation over time and weak contrast sequences. These two phenomena typically occur in real clinical situations.

Furthermore, by applying the proposed method to two clinical cases with pathologies, we presented the radial deformation on end-systole frames as well as the local region tracking results of the myocardium. Our results discriminate between the different motion behaviors of the myocardium local regions. We also highlight that the local tracking results are potentially a useful indicator for the abnormalities of cardiac motion. In future work, an extension to 3D data application based on hyper-complex analytical signals and their phases will be studied.

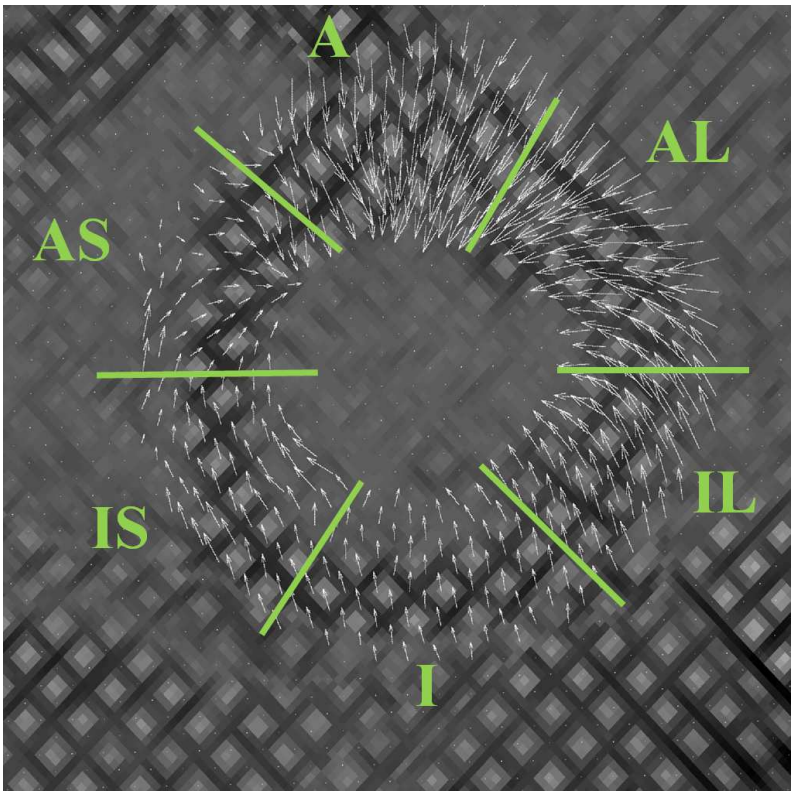

(a)

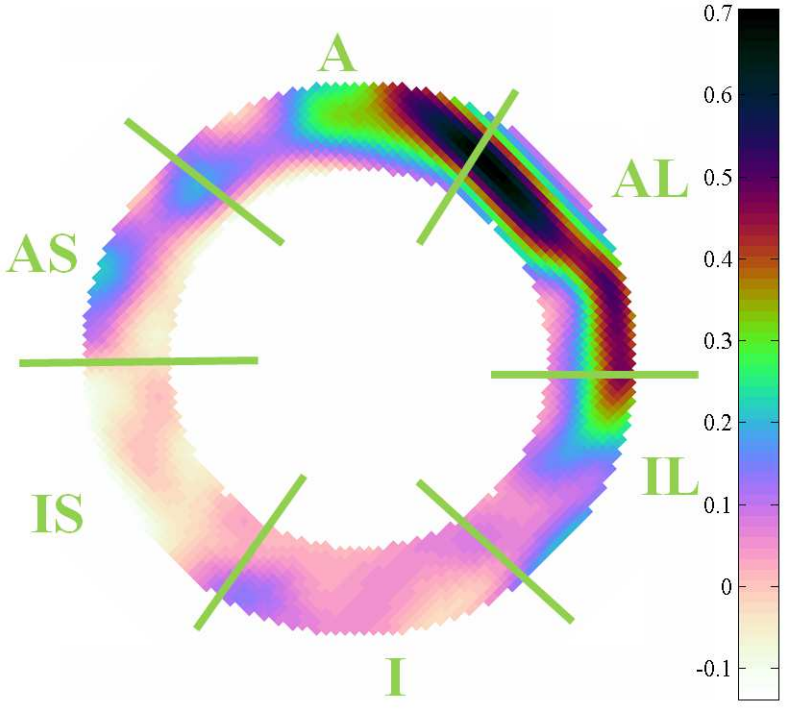

(b)

Figure 5.12: (a) Lagrangian motion field at end-systole frame. (b) Radial deformation E_{rr} of (a).

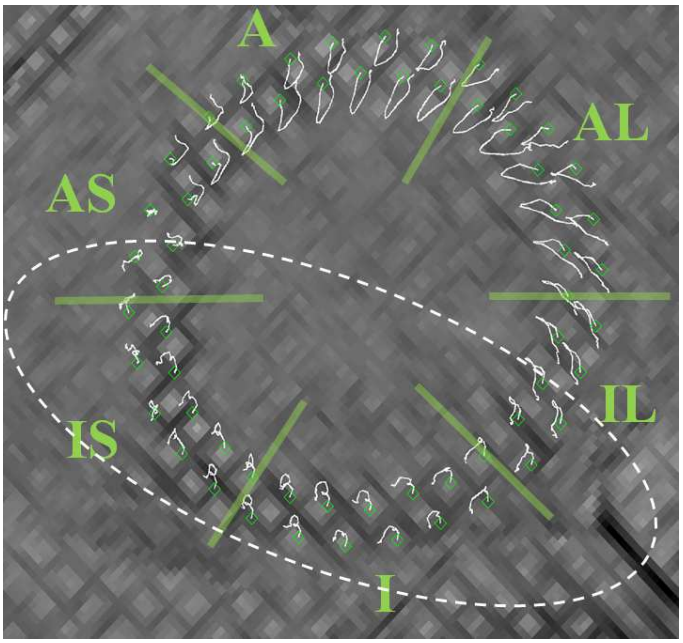

(a)

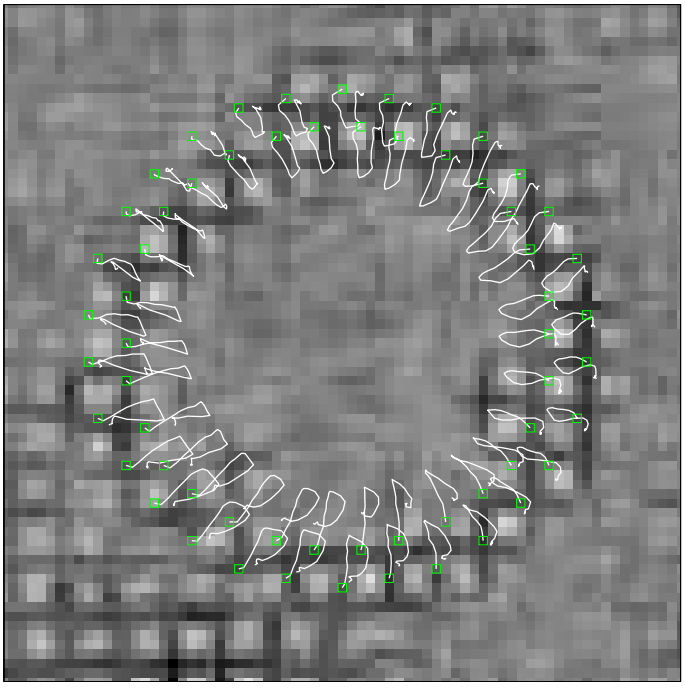

(b)

Figure 5.13: Trace of the myocardium local points on short-axis image sequence. (a) The region in the white dashed circle of the myocardium has shorter and non-smooth traces than the normal region at the myocardium segments A and AL, which indicates the possible myocardium pathologies. (b) A healthy case from a volunteer. All the tracing points represent the same tendency of contraction/dilation.

Conclusion and perspectives

Conclusion

This thesis has proposed an accurate motion estimation method for the cardiac tagged MRI sequence based on the phase information of a 2D analytic signal. The multidimensional extension from a 2D analytic signal has also been studied, orienting to higher-dimension data processing. The work was achieved in two parts.

First, we proposed an extension method of 2D hypercomplex QS in the framework of Clifford algebra and defined a 3D Clifford hypercomplex analytic signal. In the 2D case, Hahn's single-quadrant AS and the QS are discussed. Both of them provide their own local amplitude and local phase information and can be chosen for different application objectives. We reviewed the relation between the Hahn AS and QS and then presented the QS in Clifford algebra (with two generators) by the local amplitudes and phases of Hahn AS. Extending this idea from 2D to 3D, we proposed the 3D CAS in Clifford algebra with three generators. From the total/partial Hilbert transformation of a 3D input real signal, we set up a direct relation between 3D CAS and 3D Hahn AS amplitudes and phases. Hence, with the aid of the 3D classic Fourier transform (to calculate the 3D Hahn AS), the hypercomplex 3D CAS can be obtained. It also provides an easy way for the numerical implementation of 3D CAS. Then the amplitude of 3D CAS is defined, which is employed in an application of 3D envelope detection of RF ultrasound data. In an experiment, we acquired an RF volume from an ultrasound phantom with a biopsy needle inserted and calculated its envelope. In the comparison with 1D and 2D methods, the 3D CAS envelope provides an optimized contrast image of the biopsy needle. For further applications such as image segmentation, detection, and registration, the 3D CAS envelope shows potential quality improvement.

Secondly, a motion estimation method for tagged MRI sequences is proposed with the phase information integrated into an optical flow method. The two phases of the 2D Hahn AS are chosen in this method to split the tagging line information in the tagged MRI image and adapt to the requirement of the optical flow equation. In the proposed method, the local bilinear model and a global refining method are employed on the phase-based optical flow motion field, which improves the accuracy of displacement estimation. The performance of this method is evaluated in several types of simulated sequences. Compared with two other effective methods, the proposed method gives fewer estimation

errors. At the same time, this method is less sensitive to both pixel intensity variation over time and weak contrast sequences. These two phenomena typically occur in real clinical situations. After that, the proposed method was applied to two clinical cases with pathologies, and the radial deformation was applied to end-systole frames as well as local region tracking results of the myocardium. From these results, the different motion behaviors of the myocardium local regions can be clearly distinguished. Therefore, the local tracking results are potentially a useful indicator for the abnormalities of cardiac motion.

Based on the 2D complex Hahn AS, this study demonstrates an accurate and reliable myocardial motion estimation method for the 2D tagged MRI image. It shows that the phase information is a useful mathematical tool to represent the image's features. To determine the possible extension of this motion estimation method in a higher dimension, a theoretical study on the complex/hypercomplex analytical signal was conducted, showing the relation between them for both 2D and 3D and providing a possible tool to process 2D and extend to 3D image processing on myocardial motion estimation and ultrasound envelope detection.

Perspectives

For the 3D CAS, it should be pointed out that the polar form can be defined differently. In Clifford algebra, one of the possible polar forms of 3D CAS could be a scalar part, a pseudo-scalar part, and six phases. Based on the present work, additional research can focus on how to present the polar form of 3D CAS by the phases and amplitudes of 3D Hahn AS. In addition, since we found there are partial phases/amplitudes in the QS [Bayro-Corrochano (2006)], the partial phases/amplitudes for the 3D CAS can also be defined. Their properties need to be studied to adapt to various applications. The phase-based method for the myocardial motion estimation can be further extended in the 3D case using the 3D Hahn AS phases. Hence, it is possible to process the 3D MRI myocardial data, such as volume data on the 3D space coordinate of x, y, z. Furthermore, the choice of phase is an important step for the 3D motion estimation when using the 3D Hahn AS phases: four phases are available to find three unknown displacements on x, y, z, respectively. However, it is possible to define three partial phases to process the 3D problem. Hence, the definition of multidimensional analytical phases and its application remains an open question.

Appendix

Appendix A

Appendix 1

2D two-sided QFT and classical convolutions

For the 2D real signal $f(x, y)$, its two-sided QFT $F_{TS}(u, v)$ is defined by:

$$F_{TS}(u, v) = \int e^{-2\pi iux} f(x, y) e^{-2\pi jvy} dxdy,$$

and the inverse QFT is defined by:

$$f(x, y) = \int e^{2\pi iux} F_{TS}(u, v) e^{2\pi jvy} dudv.$$

Then, the 2D two-sided QS ψ_{qTS} is:

$$\psi_{qTS} = F^{-1} \left[(1 + sign(u)) (1 + sign(v)) F_{TS}(u, v) \right].$$

Known that:

$$\int e^{2\pi iux} \left[sign(u) \right] du = \frac{i}{\pi x}, \qquad \int e^{2\pi jvy} \left[sign(v) \right] dv = \frac{j}{\pi y},$$

we obtain,

(1) Case $sign(u)F_{TS}(u,v)$:

$$\begin{aligned}
F^{-1}\left[sign(u)F_{TS}(u,v)\right] &= \int e^{2\pi iux} sign(u) F_{TS}(u,v) e^{2\pi jvy} dudv \\
&= \int e^{2\pi iux} sign(u) \left[e^{-2\pi iux'} f(x',y') e^{-2\pi jvy'} dx'dy'\right] e^{2\pi jvy} dudv \\
&= \int f(x',y') e^{2\pi iux} sign(u) e^{-2\pi iux'} e^{-2\pi jvy'} e^{2\pi jvy} dx'dy'dudv \\
&= \int f(x',y') sign(u) e^{2\pi i(ux-ux')} \delta\left(y-y'\right) dx'dy'du \\
&= \int f(x',y') \frac{i}{\pi\left(x-x'\right)} \delta\left(y-y'\right) dx'dy' \\
&= if(x,y) \star\star \frac{\delta\left(y\right)}{\pi x}
\end{aligned}$$

(2) Case $sign(v)F_{TS}(u,v)$:

$$\begin{aligned}
F^{-1}\left[sign(v)F_{TS}(u,v)\right] &= \int e^{2\pi iux} sign(v) F_{TS}(u,v) e^{2\pi jvy} dudv \\
&= \int e^{2\pi iux} sign(v) \left[e^{-2\pi iux'} f(x',y') e^{-2\pi jvy'} dx'dy'\right] e^{2\pi jvy} dudv \\
&= \int f(x',y') e^{2\pi iux} sign(v) e^{-2\pi iux'} e^{-2\pi jvy'} e^{2\pi jvy} dx'dy'dudv \\
&= \int f(x',y') e^{2\pi i(ux-ux')} sign(v) e^{-2\pi jv(y'-y)} dvdx'dy'du \\
&= \int f(x',y') \delta\left(x-x'\right) \frac{j}{\pi(y-y')} dx'dy'du1 \\
&= jf(x,y) \star\star \frac{\delta\left(x\right)}{\pi y}
\end{aligned}$$

(3) Case $sign(u)sign(v)F_{TS}(u,v)$:

$$\begin{aligned}
F^{-1}\left[sign(v)F_{TS}(u,v)\right] &= \int e^{2\pi iux} sign(u)sign(v) F_{TS}(u,v) e^{2\pi jvy} dudv \\
&= \int e^{2\pi iux} sign(u)sign(v) \left[e^{-2\pi iux'} f(x',y') e^{-2\pi jvy'} dx'dy'\right] e^{2\pi jvy} dudv \\
&= \int f(x',y') e^{2\pi iux} sign(u)sign(v) e^{-2\pi iux'} e^{-2\pi jvy'} e^{2\pi jvy} dx'dy'dudv \\
&= \int f(x',y') \frac{i}{\pi\left(x-x'\right)} \frac{j}{\pi\left(y-y'\right)} dx'dy' \\
&= kf(x,y) \star\star \frac{1}{\pi^2 xy}
\end{aligned}$$

Finally, from the two-sided QFT, we have

$$\begin{aligned}
&\psi_{qTS}(x,y) \\
&= f(x,y) \star\star \left[\left(\delta\left(x\right) + \frac{i}{\pi x}\right)\left(\delta\left(y\right) + \frac{j}{\pi y}\right)\right] \\
&= f(x,y) \star\star (\delta(x)\delta(y)) + if(x,y) \star\star \left(\frac{\delta\left(y\right)}{\pi x}\right) + jf(x,y) \star\star \left(\frac{\delta\left(x\right)}{\pi y}\right) + kf(x,y) \star\star \left(\frac{1}{\pi^2 xy}\right)
\end{aligned}$$

2D right-sided QFT and classical convolutions

For the 2D real signal $f(x,y)$, its right-sided QFT $F_{RS}(u,v)$ is defined by:

$$F_{RS}(u,v) = \int f(x,y)e^{-2\pi iux}e^{-2\pi jvy}dxdy,$$

and the inverse QFT is defined by:

$$f(x,y) = \int F_{RS}(u,v)e^{2\pi jvy}e^{2\pi iux}dudv.$$

Then, the 2D right-sided QS ψ_{qRS} is:

$$\psi_{qRS} = F^{-1}\left[(1+sign(u))\,(1+sign(v))\,F_{RS}(u,v)\right].$$

Known that,

$$\int e^{2\pi iux}\left[sign(u)\right]du = \frac{i}{\pi x}, \qquad \int e^{2\pi jvy}\left[sign(v)\right]dv = \frac{j}{\pi y},$$

we obtain,

(1) Case $sign(u)F_{RS}(u,v)$

$$\begin{aligned}
F^{-1}\left[sign(u)F_{RS}(u,v)\right] &= \int sign(u)F_{RS}(u,v)e^{2\pi jvy}e^{2\pi iux}dudv \\
&= \int sign(u)\left[f(x',y')e^{-2\pi iux'}e^{-2\pi jvy'}dx'dy'\right]e^{2\pi jvy}e^{2\pi iux}dudv \\
&= \int f(x',y')e^{-2\pi iux'}sign(u)e^{2\pi jv(y-y')}e^{2\pi iux}dx'dy'dudv \\
&= \int f(x',y')sign(u)e^{-2\pi iux'}\delta\left(y-y'\right)e^{2\pi iux}dx'dy'du \\
&= \int f(x',y')\delta\left(y-y'\right)\frac{i}{\pi\left(x-x'\right)}dx'dy' \\
&= if(x,y)\star\star\frac{\delta\left(y\right)}{\pi x}
\end{aligned}$$

(2) Case $sign(v)F_{RS}(u,v)$

$$\begin{aligned}
F^{-1}\left[sign(v)F_{RS}(u,v)\right] &= \int sign(v)F_{RS}(u,v)e^{2\pi jvy}e^{2\pi iux}dudv \\
&= \int sign(v)\left[f(x',y')e^{-2\pi iux'}e^{-2\pi jvy'}dx'dy'\right]e^{2\pi jvy}e^{2\pi iux}dudv \\
&= \int f(x',y')e^{-2\pi iux'}sign(v)e^{2\pi jv(y-y')}e^{2\pi iux}dx'dy'dudv \\
&= \int f(x',y')e^{-2\pi iux'}\frac{j}{\pi\left(y-y'\right)}e^{2\pi iux}dx'dy'du \\
&= \int f(x',y')\frac{j}{\pi\left(y-y'\right)}e^{2\pi iux'}e^{2\pi iux}dx'dy'du \\
&= \int f(x',y')\frac{j}{\pi\left(y-y'\right)}\delta\left(x+x'\right)dx'dy' \\
&= jf(-x,y)\star\star\frac{\delta\left(x\right)}{\pi y}
\end{aligned}$$

(3) Case $sign(u)sign(v)F_{RS}(u,v)$

$$\begin{aligned}
F^{-1}\left[sign(u)sign(v)F_{RS}(u,v)\right] &= \int sign(u)sign(v)F_{RS}(u,v)e^{2\pi jvy}e^{2\pi iux}dudv \\
&= \int sign(u)sign(v)\left[f(x',y')e^{-2\pi iux'}e^{-2\pi jvy'}dx'dy'\right]e^{2\pi jvy}e^{2\pi iux}dudv \\
&= \int f(x',y')e^{-2\pi iux'}sign(u)sign(v)e^{2\pi jv(y-y')}e^{2\pi iux}dx'dy'dudv \\
&= \int f(x',y')e^{-2\pi iux'}sign(u)\frac{j}{\pi\left(y-y'\right)}e^{2\pi iux}dx'dy'du \\
&= \int f(x',y')\frac{j}{\pi\left(y-y'\right)}sign(u)e^{2\pi iux'}e^{2\pi iux}dx'dy'du \\
&= \int f(x',y')\frac{j}{\pi\left(y-y'\right)}\frac{i}{\pi\left(x+x'\right)}dx'dy' \\
&= -kf(-x,y)\star\star\left(\frac{1}{\pi^2xy}\right)
\end{aligned}$$

Finally, from the right-sided QFT, we have

$$\psi_{qRS}(x,y) = f(x,y)\star\star(\delta(x)\delta(y)) + if(x,y)\star\star\left(\frac{\delta(y)}{\pi x}\right) + jf(-x,y)\star\star\left(\frac{\delta(x)}{\pi y}\right) - kf(-x,y)\star\star\left(\frac{1}{\pi^2xy}\right)$$

The right-side QS can be represented by the classical convolutions in the framework of the quaternion Clifford algebra. Therefore, we can use the complex Fourier transform and the phases of Hahn to calculate the right-side QS. The similar procedure can be used for left-side QFT and also for the 3D cases.

3D right-sided Clifford Fourier transform and classical convolutions

For a 3D input real signal $f(x,y,z)$, its right-sided Clifford Fourier transform $F_{RS}(u,v,w)$ is defined by [Girard *et al.* (2013)]:

$$F_{RS}(u,v,w) = \int f(x,y,z)e^{-2\pi\epsilon iux}e^{-2\pi\epsilon jvy}e^{-2\pi\epsilon kwz}dxdydz,$$

and its inverse:

$$f(x,y,z) = \int F_{RS}(u,v,w)e^{2\pi\epsilon kwz}e^{2\pi\epsilon jvy}e^{2\pi\epsilon iux}dudvdw.$$

Then the analytic signal Ψ is:

$$\Psi = F^{-1}\left[\left(1+sign(u)\right)\left(1+sign(v)\right)\left(1+sign(w)\right)F_{RS}(u,v,w)\right].$$

Known that,

$$\int e^{2\pi iux}\left[sign(u)\right]du = \frac{i}{\pi x}, \quad \int e^{2\pi jvy}\left[sign(v)\right]dv = \frac{j}{\pi y}, \quad f(x)\star g(x) = \int f(y)g(x-y)dy,$$

$$\int f(x',y',z')\frac{1}{\pi\left(z-z'\right)}\frac{1}{\pi\left(y+y'\right)}\frac{1}{\pi\left(x-x'\right)}dx'dy'dz' = f(x,-y,z)\star\star\star\frac{1}{\pi y}\frac{1}{\pi x}\frac{1}{\pi z}$$

we obtain,

(1.a) Case $sign(u)F_{RS}(u,v,w)$

$$
\begin{aligned}
& F^{-1}\left[sign(u)F_{RS}(u,v,w)\right] \\
= & \int sign(u)F_{RS}(u,v,w)e^{2\pi\epsilon kwz}e^{2\pi\epsilon jvy}e^{2\pi\epsilon iux}dudvdw \\
= & \int sign(u)\left[f(x',y',z')e^{-2\pi\epsilon iux'}e^{-2\pi\epsilon jvy'}e^{-2\pi\epsilon kwz'}dx'dy'dz'\right]e^{2\pi\epsilon kwz}e^{2\pi\epsilon jvy}e^{2\pi\epsilon iux}dudvdw \\
= & \int f(x',y',z')e^{-2\pi\epsilon iux'}sign(u)e^{-2\pi\epsilon jvy'}e^{-2\pi\epsilon kwz'}e^{2\pi\epsilon kwz}e^{2\pi\epsilon jvy}e^{2\pi\epsilon iux}dx'dy'dz'dudvdw \\
= & \int f(x',y',z')sign(u)e^{-2\pi\epsilon iux'}\delta\left(y-y'\right)\delta\left(z-z'\right)e^{2\pi\epsilon iux}dx'dy'du \\
= & \int f(x',y',z')\delta\left(y-y'\right)\delta\left(z-z'\right)\frac{\epsilon i}{\pi\left(x-x'\right)}dx'dy'dz' \\
= & \epsilon i f(x,y,z)\star\star\star\frac{\delta\left(y\right)\delta\left(z\right)}{\pi x}
\end{aligned}
$$

(1.b) Case $sign(v)F_{RS}(u,v,w)$

$$
\begin{aligned}
& F^{-1}\left[sign(v)F_{RS}(u,v,w)\right] \\
= & \int sign(v)F_{RS}(u,v,w)e^{2\pi\epsilon kwz}e^{2\pi\epsilon jvy}e^{2\pi\epsilon iux}dudvdw \\
= & \int sign(v)\left[f(x',y',z')e^{-2\pi\epsilon iux'}e^{-2\pi\epsilon jvy'}e^{-2\pi\epsilon kwz'}dx'dy'dz'\right]e^{2\pi\epsilon kwz}e^{2\pi\epsilon jvy}e^{2\pi\epsilon iux}dudvdw \\
= & \int f(x',y',z')e^{-2\pi\epsilon iux'}sign(v)e^{-2\pi\epsilon jvy'}e^{-2\pi\epsilon kwz'}e^{2\pi\epsilon kwz}e^{2\pi\epsilon jvy}e^{2\pi\epsilon iux}dx'dy'dz'dudvdw \\
= & \int f(x',y',z')e^{-2\pi\epsilon iux'}\frac{\epsilon j}{\pi\left(y-y'\right)}\delta\left(z-z'\right)e^{2\pi iux}dx'dy'dz'du \\
= & \epsilon j\int f(x',y',z')\delta\left(x+x'\right)\delta\left(z-z'\right)\frac{1}{\pi\left(y-y'\right)}dx'dy'dz' \\
= & \epsilon j f(-x,y,z)\star\star\star\frac{\delta\left(x\right)\delta\left(z\right)}{\pi y}
\end{aligned}
$$

(1.c) Case $sign(w)F_{RS}(u,v,w)$

$$
\begin{aligned}
& F^{-1}\left[sign(w)F_{RS}(u,v,w)\right] \\
= & \int sign(w)F_{RS}(u,v,w)e^{2\pi\epsilon kwz}e^{2\pi\epsilon jvy}e^{2\pi\epsilon iux}dudvdw \\
= & \int sign(w)\left[f(x',y',z')e^{-2\pi\epsilon iux'}e^{-2\pi\epsilon jvy'}e^{-2\pi\epsilon kwz'}dx'dy'dz'\right]e^{2\pi\epsilon kwz}e^{2\pi\epsilon jvy}e^{2\pi\epsilon iux}dudvdw \\
= & \int f(x',y',z')e^{-2\pi\epsilon iux'}sign(w)e^{-2\pi\epsilon jvy'}e^{-2\pi\epsilon kwz'}e^{2\pi\epsilon kwz}e^{2\pi\epsilon jvy}e^{2\pi\epsilon iux}dx'dy'dz'dudvdw \\
= & \int f(x',y',z')\frac{\epsilon k}{\pi\left(z-z'\right)}\delta\left(y+y'\right)\delta\left(x+x'\right)dx'dy'dz' \\
= & \epsilon k\int f(x',y',z')\delta\left(x+x'\right)\delta\left(y+y'\right)\frac{1}{\pi\left(z-z'\right)}dx'dy'dz' \\
= & \epsilon k f(-x,-y,z)\star\star\star\frac{\delta\left(x\right)\delta\left(y\right)}{\pi z}
\end{aligned}
$$

(2.a) Case $sign(u)sign(v)F_{RS}(u,v,w)$

$$
\begin{aligned}
& F^{-1}\left[sign(u)sign(v)F_{RS}(u,v,w)\right] \\
= & \int sign(u)sign(v)F_{RS}(u,v,w)e^{2\pi\epsilon kwz}e^{2\pi\epsilon jvy}e^{2\pi\epsilon iux}dudvdw \\
= & \int sign(u)sign(v)\left[f(x',y',z')e^{-2\pi\epsilon iux'}e^{-2\pi\epsilon jvy'}e^{-2\pi\epsilon kwz'}dx'dy'dz'\right]e^{2\pi\epsilon kwz}e^{2\pi\epsilon jvy}e^{2\pi\epsilon iux}dudvdw \\
= & \int f(x',y',z')e^{-2\pi\epsilon iux'}sign(u)sign(v)e^{-2\pi\epsilon jvy'}e^{-2\pi\epsilon kwz'}e^{2\pi\epsilon kwz}e^{2\pi\epsilon jvy}e^{2\pi\epsilon iux}dx'dy'dz'dudvdw \\
= & \epsilon j\int f(x',y',z')\frac{\epsilon i}{\pi\left(x+x'\right)}\frac{1}{\pi\left(y-y'\right)}\delta\left(z-z'\right)dx'dy'dz' \\
= & -k\int f(x',y',z')\frac{1}{\pi\left(x+x'\right)}\frac{1}{\pi\left(y-y'\right)}\delta\left(z-z'\right)dx'dy'dz' \\
= & -kf(-x,y,z)\star\star\star\frac{1}{\pi y}\frac{1}{\pi x}\delta\left(z\right)
\end{aligned}
$$

(2.b) Case $sign(u)sign(w)F_{RS}(u,v,w)$

$$
\begin{aligned}
& F^{-1}\left[sign(u)sign(w)F_{RS}(u,v,w)\right] \\
= & \int sign(u)sign(w)F_{RS}(u,v,w)e^{2\pi\epsilon kwz}e^{2\pi\epsilon jvy}e^{2\pi\epsilon iux}dudvdw \\
= & \int sign(u)sign(w)\left[f(x',y',z')e^{-2\pi\epsilon iux'}e^{-2\pi\epsilon jvy'}e^{-2\pi\epsilon kwz'}dx'dy'dz'\right]e^{2\pi\epsilon kwz}e^{2\pi\epsilon jvy}e^{2\pi\epsilon iux}dudvdw \\
= & \int f(x',y',z')e^{-2\pi\epsilon iux'}sign(u)sign(w)e^{-2\pi\epsilon jvy'}e^{-2\pi\epsilon kwz'}e^{2\pi\epsilon kwz}e^{2\pi\epsilon jvy}e^{2\pi\epsilon iux}dx'dy'dz'dudvdw \\
= & \int f(x',y',z')\frac{\epsilon k}{\pi\left(z-z'\right)}\frac{\epsilon i}{\pi\left(x+x'\right)}\delta\left(y+y'\right)dx'dy'dz' \\
= & j\int f(x',y',z')\frac{1}{\pi\left(x+x'\right)}\frac{1}{\pi\left(z-z'\right)}\delta\left(y+y'\right)dx'dy'dz' \\
= & jf(-x,-y,z)\star\star\star\frac{1}{\pi x}\frac{1}{\pi z}\delta\left(y\right)
\end{aligned}
$$

(2.c) Case $sign(v)sign(w)F_{RS}(u,v,w)$

$$
\begin{aligned}
& F^{-1}\left[sign(v)sign(w)F_{RS}(u,v,w)\right] \\
= & \int sign(v)sign(w)F_{RS}(u,v,w)e^{2\pi\epsilon kwz}e^{2\pi\epsilon jvy}e^{2\pi\epsilon iux}dudvdw \\
= & \int sign(v)sign(w)\left[f(x',y',z')e^{-2\pi\epsilon iux'}e^{-2\pi\epsilon jvy'}e^{-2\pi\epsilon kwz'}dx'dy'dz'\right]e^{2\pi\epsilon kwz}e^{2\pi\epsilon jvy}e^{2\pi\epsilon iux}dudvdw \\
= & \int f(x',y',z')e^{-2\pi\epsilon iux'}sign(v)sign(w)e^{-2\pi\epsilon jvy'}e^{-2\pi\epsilon kwz'}e^{2\pi\epsilon kwz}e^{2\pi\epsilon jvy}e^{2\pi\epsilon iux}dx'dy'dz'dudvdw \\
= & \int f(x',y',z')\frac{\epsilon k}{\pi\left(z-z'\right)}\frac{\epsilon j}{\pi\left(y+y'\right)}\delta\left(x-x'\right)dx'dy'dz' \\
= & -i\int f(x',y',z')\frac{1}{\pi\left(y+y'\right)}\frac{1}{\pi\left(z-z'\right)}\delta\left(x-x'\right)dx'dy'dz' \\
= & -if(x,-y,z)\star\star\star\frac{1}{\pi y}\frac{1}{\pi z}\delta\left(x\right)
\end{aligned}
$$

(3) Case $sign(u)sign(v)sign(w)F_{RS}(u,v,w)$

$$
\begin{aligned}
& F^{-1}\left[sign(u)sign(v)sign(w)F_{RS}(u,v,w)\right] \\
= & \int sign(u)sign(v)sign(w)F_{RS}(u,v,w)e^{2\pi\epsilon kwz}e^{2\pi\epsilon jvy}e^{2\pi\epsilon iux}dudvdw \\
= & \int sign(u)sign(v)sign(w)\left[f(x',y',z')e^{-2\pi\epsilon iux'}e^{-2\pi\epsilon jvy'}e^{-2\pi\epsilon kwz'}dx'dy'dz'\right] \\
& e^{2\pi\epsilon kwz}e^{2\pi\epsilon jvy}e^{2\pi\epsilon iux}dudvdw \\
= & \int f(x',y',z')e^{-2\pi\epsilon iux'}sign(u)sign(v)sign(w)e^{-2\pi\epsilon jvy'}e^{-2\pi\epsilon kwz'}e^{2\pi\epsilon kwz}e^{2\pi\epsilon jvy}e^{2\pi\epsilon iux} \\
& dx'dy'dz'dudvdw \\
= & \int f(x',y',z')\frac{\epsilon k}{\pi\left(z-z'\right)}\frac{\epsilon j}{\pi\left(y+y'\right)}\frac{\epsilon i}{\pi\left(x-x'\right)}dx'dy'dz' \\
= & \epsilon\int f(x',y',z')\frac{1}{\pi\left(z-z'\right)}\frac{1}{\pi\left(y+y'\right)}\frac{1}{\pi\left(x-x'\right)}dx'dy'dz' \\
= & \epsilon f(x,-y,z)\star\star\star\frac{1}{\pi y}\frac{1}{\pi z}\frac{1}{\pi x}
\end{aligned}
$$

Finally, we have the 3D hypercomplex analytic signal $\Psi(x,y,z)$ from the right-sided Clifford Fourier transform

$$
\begin{aligned}
\Psi = & f(x,y,z)\star\star\star\delta\left(x,y,z\right)-if(x,-y,z)\star\star\star\frac{\delta(x)}{\pi^2yz} \\
& +jf(-x,-y,z)\star\star\star\frac{\delta(y)}{\pi^2xz}-kf(-x,y,z)\star\star\star\frac{\delta(z)}{\pi^2xy} \\
& +\epsilon f(x,-y,z)\star\star\star\frac{1}{\pi^3xyz}+\epsilon if(x,y,z)\star\star\star\frac{\delta(y)\delta(z)}{\pi x} \\
& +\epsilon jf(-x,y,z)\star\star\star\frac{\delta(x)\delta(z)}{\pi y}+\epsilon kf(-x,-y,z)\star\star\star\frac{\delta(x)\delta(y)}{\pi z}
\end{aligned}
$$

Therefore, this 3D hypercomplex analytic signal $\Psi(x,y,z)$ can be represented by the classical convolutions in the framework of hyperquaternion Clifford algebra. we can use the 3D complex Fourier transform and the 3D phases of Hahn to calculate the analytic signal $\Psi(x,y,z)$.

Publication list

International conference paper

[Wang et al. (2012)] **Wang, L.**, Girard, P., Bernard, A., Liu, Z., Clarysse, P., and Delachartre, P. 3-D biquaternionic analytic signal and application to envelope detection in 3-D ultrasound imaging. In *IEEE International Conference on 3D Imaging (IC3D)*, pages 1-8, Liège, Belgium, December, 2012.

[Wang et al. (2012)] **Wang, L.**, Girard, P., Clarysse, P., and Delachartre, P. Phase extraction of the analytic video signal in Clifford algebra. In *5th conference on Applied Geometric Algebras in Computer Science and Engineering*, La Rochelle, France, July, 2012.

[Wang et al. (2014)] **Wang, L.**, Liu, Z., Clarysse, P., Croisille, P., Girard, P., Liu, W., and Delachartre, P. Myocardial motion estimation using optical flow with multiple constraint equations. In *IEEE International Conference on Signal Processing (ICSP14)*, pages 1066-1071, HangZhou, October, 2014.

[Farouj et al. (2014)] Farouj, Y., **Wang, L.**, Clarysse, P., Navarro, L., Clausel, M., and Delachartre, P. Cardiac motion analysis using wavelet projections from tagged MR sequences. In *IEEE International Conference on Image Processing (ICIP'14)*, Paris, October, 2014.

[Girard et al. (2014)] Girard, P., Clarysse, P., Pujol, R., **Wang, L.**, and Delachartre, P. Biquaternion Clifford algebra and Grassmann differential geometry. In *8th International Conference, Curves and Surfaces*, Paris, France, June, 2014.

National communication

[Wang et al. (2012)] **Wang, L.**, Liu, Z., Girard, P., Clarysse, P., and Delachartre, P. Extension of analytic signal conception on dynamic image sequences. In *9ème Manifestation des Jeunes Chercheurs en Sciences et Technologies de l'Information et de la Communication*, Lille, France, October, 2012.

Bibliography

[Alessandrini *et al.* (2013)] Alessandrini, M., Basarab, A., Liebgott, H., and Bernard, O. (2013). Myocardial motion estimation from medical images using the monogenic signal. *IEEE Transactions on Image Processing*, 22(3):1084–1095.

[Alfsmann *et al.* (2007)] Alfsmann, D., Göckler, H. G., Sangwine, S. J., Ell, T. A., and universität Bochum, R. (2007). Hypercomplex algebras in digital signal processing: Benefits and drawbacks. In *15th European Signal Processing Conference (EUSIPCO)*, pages 1322–1326, Poznan, Poland. EURASIP.

[Argyriou and Vlachos (2006)] Argyriou, V. and Vlachos, T. (2006). A study of sub-pixel motion estimation using phase correlation. In *Proceedings of the British Machine Vision Conference*, pages 40.1–40.10. BMVA Press.

[Arif *et al.* (2014)] Arif, O., Sundaramoorthi, G., Hong, B.-W., and Yezzi, A. (2014). Tracking using motion estimation with physically motivated inter-region constraints. *IEEE Transactions on Medical Imaging*, 33(9):1875–1889.

[Arts *et al.* (2010)] Arts, T., Prinzen, F., Delhaas, T., Milles, J., Rossi, A., and Clarysse, P. (2010). Mapping displacement and deformation of the heart with local sine-wave modeling. *IEEE Transactions on Medical Imaging*, 29(5):1114–1123.

[Axel *et al.* (2005)] Axel, L., Montillo, A., and Kim, D. (2005). Tagged magnetic resonance imaging of the heart: a survey. *Medical Image Analysis*, 9(4):376 – 393.

[Axel and Dougherty (1989)] Axel, L. and Dougherty, L. (1989). MR imaging of motion with spatial modulation of magnetization. *Radiology*, 171(3):841–845.

[Baker *et al.* (2007)] Baker, S., Roth, S., Scharstein, D., Black, M., Lewis, J. P., and Szeliski, R. (2007). A database and evaluation methodology for optical flow. In *IEEE 11th International Conference on Computer Vision. ICCV 2007*, pages 1–8.

[Baker *et al.* (2011)] Baker, S., Scharstein, D., Lewis, J. P., Roth, S., Black, M. J., and Szeliski, R. (2011). A database and evaluation methodology for optical flow. *International Journal of Computer Vision*, 92(1):1–31.

[Barva (2007)] Barva, M. (2007). *Localization of Surgical Instruments in 3D Ultrasound Images*. PhD thesis, Czech Technical University.

[Basarab *et al.* (2008)] Basarab, A., Liebgott, H., Morestin, F., Lyshchik, A., Higashi, T., Asato, R., and Delachartre, P. (2008). A method for vector displacement estimation with ultrasound images and its application for thyroid nodular disease. *Medical Image Analysis*, 12(3):259–274.

[Basarab *et al.* (2009)] Basarab, A., Liebgott, H., and Delachartre, P. (2009). Analytic estimation of subsample spatial shift using the phases of multidimensional analytic signals. *IEEE Transactions on Image Processing*, 18(2):440–447.

[Bayro-Corrochano (2006)] Bayro-Corrochano, E. (2006). The theory and use of the quaternion wavelet transform. *Journal of Mathematical Imaging and Vision*, 24(1):19–35.

[Belytschko *et al.* (2013)] Belytschko, T., Liu, W. K., Moran, B., and Elkhodary, K. (2013). *Nonlinear finite elements for continua and structures*. John Wiley & Sons.

[Brotman *et al.* (2013)] Brotman, D., Zhang, Z., and Sampath, S. (2013). Effect of through-plane motion on left ventricular rotation: a study using slice-following harmonic phase imaging. *Magnetic Resonance in Medicine*, 69(5):1421–1429.

[Bruni *et al.* (2007)] Bruni, V., De Canditiis, D., and Vitulano, D. (2007). Phase-based motion estimation for noisy sequences. In *14th International Workshop on Systems, Signals and Image Processing, 2007 and 6th EURASIP Conference focused on Speech and Image Processing, Multimedia Communications and Services*, pages 381–384.

[Bruni *et al.* (2009)] Bruni, V., De Canditiis, D., and Vitulano, D. (2009). Phase information and space filling curves in noisy motion estimation. *IEEE Transactions on Image Processing*, 18(7):1660–1664.

[Bruno and Pellerin (2002)] Bruno, E. and Pellerin, D. (2002). Robust motion estimation using spatial gabor-like filters. *Signal Processing*, 82(2):297 – 309.

[Butler *et al.* (2012)] Butler, D. J., Wulff, J., Stanley, G. B., and Black, M. J. (2012). A naturalistic open source movie for optical flow evaluation. In *Proceedings of the 12th European Conference on Computer Vision*, Part IV, Lecture Notes in Computer Science 7577, pages 611–625, Berlin, Heidelberg. Springer-Verlag.

[Bülow (1999)] Bülow, T. (1999). *Hypercomplex spectral signal representations for the processing and analysis of images*. PhD thesis, Christian-Albrechts-Universität.

[Bülow and Sommer (1997)] Bülow, T. and Sommer, G. (1997). Multi-dimensional signal processing using an algebraically extended signal representation. In Sommer, G. and Koenderink, J., editors, *Algebraic Frames for the Perception-Action Cycle*, volume 1315 of *Lecture Notes in Computer Science*, pages 148–163. Springer Berlin Heidelberg.

[Bülow and Sommer (2001)] Bülow, T. and Sommer, G. (2001). Hypercomplex signals-a novel extension of the analytic signal to the multidimensional case. *IEEE Transactions on Signal Processing*, 49(11):2844–2852.

[Cerqueira *et al.* (2002)] Cerqueira, M. D., Weissman, N. J., Dilsizian, V., Jacobs, A. K., Kaul, S., Laskey, W. K., Pennell, D. J., Rumberger, J. A., Ryan, T., and Verani, M. S. (2002). Standardized myocardial segmentation and nomenclature for tomographic imaging of the heart a statement for healthcare professionals from the cardiac imaging committee of the council on clinical cardiology of the american heart association. *Circulation*, 105(4):539–542.

[Chien and Aoki (2004)] Chien, L. and Aoki, T. (2004). Robust motion estimation for video sequences based on phase-only correlation. In *Proceedings of the 6th IASTED International Conference on Signal and Image Processing*, pages 441–446.

[Clarysse *et al.* (2000)] Clarysse, P., Basset, C., Khouas, L., Croisille, P., Friboulet, D., Odet, C., and Magnin, I. E. (2000). 2D spatial and temporal displacement field fitting from cardiac MR tagging. *Medical Image Analysis*, pages 253–268.

[Clarysse *et al.* (2011)] Clarysse, P., Tafazzoli, J., Delachartre, P., and Croisille, P. (2011). Simulation based evaluation of cardiac motion estimation methods in tagged-MR Image sequences. *Journal of Cardiovascular Magnetic Resonance*, 13(Suppl 1):P360.

[Dallal *et al.* (2012)] Dallal, A., Khalifa, A., and Fahmy, A. (2012). Accurate analysis of cardiac tagged MRI using combined HARP and optical flow tracking. In *2012 Cairo International Biomedical Engineering Conference (CIBEC)*, pages 130–133.

[Delsuc (1988)] Delsuc, M. A. (1988). Spectral representation of 2D NMR spectra by hypercomplex numbers. *Journal of Magnetic Resonance (1969)*, 77(1):119 – 124.

[Demarcq *et al.* (2009)] Demarcq, G., Mascarilla, L., and Courtellemont, P. (2009). The color monogenic signal: A new framework for color image processing. application to color optical flow. In *2009 16th IEEE International Conference on Image Processing (ICIP)*, pages 481–484.

[Demarcq *et al.* (2011)] Demarcq, G., Mascarilla, L., Berthier, M., and Courtellemont, P. (2011). The color monogenic signal: Application to color edge detection and color optical flow. *Journal of Mathematical Imaging and Vision*, 40(3):269–284.

[Dietenbeck *et al.* (2014)] Dietenbeck, T., Barbosa, D., Alessandrini, M., Jasaityte, R., Robesyn, V., D'hooge, J., Friboulet, D., and Bernard, O. (2014). Whole myocardium tracking in 2D-echocardiography in multiple orientations using a motion constrained level-set. *Medical Image Analysis*, 18(3):500–514.

[Ell (1993)] Ell, T. (1993). Quaternion-fourier transforms for analysis of two-dimensional linear time-invariant partial differential systems. In *Proceedings of the 32nd IEEE Conference on Decision and Control*, pages 1830–1841 vol.2.

[Ernst *et al.* (1987)] Ernst, R., Bodenhausen, G., and Wokaun, A. (1987). *Principles of Nuclear MagneticResonance in One and Two Dimensions*. Oxford University Press, London.

[Felsberg (2002)] Felsberg, M. (2002). *Low level image processing with the structure multivector*. PhD thesis, Institut für Informatik und Praktische Mathematik.

[Felsberg and Sommer (2001)] Felsberg, M. and Sommer, G. (2001). The monogenic signal. *IEEE Transactions on Signal Processing*, 49(12):3136–3144.

[Fleet and Jepson (1990)] Fleet, D. and Jepson, A. (1990). Computation of component image velocity from local phase information. *International Journal of Computer Vision*, 5(1):77–104.

[Gabor (1946)] Gabor, D. (1946). Theory of communication. part 1: The analysis of information. *Journal of the Institution of Electrical Engineers - Part III: Radio and Communication Engineering*, 93(26):429–441.

[Geiger *et al.* (2012)] Geiger, A., Lenz, P., and Urtasun, R. (2012). Are we ready for autonomous driving? the kitti vision benchmark suite. In *2012 IEEE Conference on Computer Vision and Pattern Recognition (CVPR)*, pages 3354–3361.

[Georgiev *et al.* (2013)] Georgiev, S., Morais, J., Kou, K., and Sprößig, W. (2013). Bochner-Minlos theorem and quaternion fourier transform. In Hitzer, E. and Sangwine, S. J., editors, *Quaternion and Clifford Fourier Transforms and Wavelets*, Trends in Mathematics, pages 105–120. Springer Basel.

[Girard *et al.* (2013)] Girard, P., Pujol, R., Clarysse, P., Marion, A., Goutte, R., and Delachartre, P. (2013). Analytic video (2D + t) signals using Clifford-Fourier transforms in multiquaternion Grassmann Hamilton Clifford algebras. In Hitzer, E. and Sangwine, S. J., editors, *Quaternion and Clifford Fourier Transforms and Wavelets*, Trends in Mathematics, pages 197–219. Springer Basel.

[Go *et al.* (2014)] Go, A. S., Mozaffarian, D., Roger, V. L., Benjamin, E. J., Berry, J. D., Blaha, M. J., Dai, S., Ford, E. S., Fox, C. S., Franco, S., Fullerton, H. J., Gillespie, C., Hailpern, S. M., Heit, J. A., Howard, V. J., Huffman, M. D., Judd, S. E., Kissela, B. M., Kittner, S. J., Lackland, D. T., Lichtman, J. H., Lisabeth, L. D., Mackey, R. H., Magid, D. J., Marcus, G. M., Marelli, A., Matchar, D. B., McGuire, D. K., Mohler, E. R., Moy, C. S., Mussolino, M. E., Neumar, R. W., Nichol, G., Pandey, D. K., Paynter, N. P., Reeves, M. J., Sorlie, P. D., Stein, J., Towfighi, A., Turan, T. N., Virani, S. S., Wong, N. D., Woo, D., and Turner, M. B. (2014). Heart disease and stroke statistics-a report from the american heart association. *Circulation*, 129(3):e28–e292.

[Guttman *et al.* (1994)] Guttman, M., Prince, J., and McVeigh, E. (1994). Tag and contour detection in tagged MR images of the left ventricle. *IEEE Transactions on Medical Imaging*, 13(1):74–88.

[Hahn (1992)] Hahn, S. (1992). Multidimensional complex signals with single-orthant spectra. *Proceedings of the IEEE*, 80(8):1287–1300.

[Hahn (1996)] Hahn, S. (1996). *Hilbert transforms in signal processing*, volume 2. Artech House Boston.

[Hahn (2003)] Hahn, S. (2003). Complex signals with single-orthant spectra as boundary distributions of multidimensional analytic functions. *Bulletin of the Polish Academy of Sciences. Technical sciences*, 51(2):155–161.

[Hahn and Snopek (2004)] Hahn, S. and Snopek, K. (2004). Comparison of properties of analytic, quaternionic and monogenic 2-D signals. *WSEAS Transactions on Computers*, 3(3):602–611.

[Hahn and Snopek (2011)] Hahn, S. and Snopek, K. (2011). The unified theory of n-dimensional complex and hypercomplex analytic signals. *Bulletin of the Polish Academy of Sciences: Technical Sciences*, 59(2):167–181.

[Harput *et al.* (2011)] Harput, S., Evans, T., Bubb, N., and Freear, S. (2011). Diagnostic ultrasound tooth imaging using fractional Fourier transform. *IEEE Transactions on Ultrasonics, Ferroelectrics and Frequency Control*, 58(10):2096–2106.

[Hedrick *et al.* (2004)] Hedrick, W. R., Hykes, D. L., and Starchman, D. E. (2004). *Ultrasound Physics and Instrumentation*. Mosby, 4 edition.

[Ibrahim (2011)] Ibrahim, E.-S. (2011). Myocardial tagging by Cardiovascular Magnetic Resonance: evolution of techniques–pulse sequences, analysis algorithms, and applications. *Journal of Cardiovascular Magnetic Resonance*, 13(1):36.

[Kar *et al.* (2014)] Kar, J., Knutsen, A., Cupps, B., and Pasque, M. (2014). A validation of two-dimensional in vivo regional strain computed from displacement encoding with stimulated echoes (dense), in reference to tagged magnetic resonance imaging and studies in repeatability. *Annals of Biomedical Engineering*, 42(3):541–554.

[Krause and Sommer (2005)] Krause, M. and Sommer, G. (2005). A 3D isotropic quadrature filter for motion estimation problems. In *Proceedings of SPIE*, volume 5960, pages 59603T–59603T–12.

[Kumar *et al.* (2011)] Kumar, S., Azartash, H., Biswas, M., and Nguyen, T. (2011). Real-time affine global motion estimation using phase correlation and its application for digital image stabilization. *IEEE Transactions on Image Processing*, 20(12):3406–3418.

[Lee *et al.* (2011)] Lee, D., Nam, W. H., Lee, J. Y., and Ra, J. B. (2011). Non-rigid registration between 3D ultrasound and CT images of the liver based on intensity and gradient information. *Physics in Medicine and Biology*, 56(1):117–137.

[Lee and Park (2009)] Lee, J. K. and Park, E. J. (2009). A fast quaternion-based orientation optimizer via virtual rotation for human motion tracking. *IEEE Transactions on Biomedical Engineering*, 56(5):1574–1582.

[Luo *et al.* (2014)] Luo, X.-X., Fang, F., Lee, A. P.-W., Sun, J.-P., Li, S., Zhang, Z.-H., Sanderson, J. E., Kwong, J. S., Zhang, Q., Wang, J., and Yu, C.-M. (2014). What can three-dimensional speckle-tracking echocardiography contribute to evaluate global left ventricular systolic performance in patients with heart failure? *International Journal of Cardiology*, 172(1):132–137.

[Maltaverne *et al.* (2010)] Maltaverne, T., Delachartre, P., and Basarab, A. (2010). Motion estimation using the monogenic signal applied to ultrasound elastography. In *2010 Annual International Conference of the IEEE Engineering in Medicine and Biology Society (EMBC)*, pages 33–36.

[Moxey *et al.* (2003)] Moxey, C., Sangwine, S., and Ell, T. (2003). Hypercomplex correlation techniques for vector images. *IEEE Transactions on Signal Processing*, 51(7):1941–1953.

[O'Dell *et al.* (1995)] O'Dell, W. G., Moore, C. C., Hunter, W. C., Zerhouni, E. A., and McVeigh, E. R. (1995). Three-dimensional myocardial deformations: calculation with displacement field fitting to tagged MR images. *Radiology*, 195(3):829–835.

[Osman *et al.* (1999)] Osman, N. F., Kerwin, W. S., Mcveigh, E. R., and Prince, J. L. (1999). Cardiac motion tracking using CINE harmonic phase (HARP) magnetic resonance imaging. *Magnetic Resonance in Medicine*, 42:1048–1060.

[Otte and Nagel (1994)] Otte, M. and Nagel, H.-H. (1994). Optical flow estimation: Advances and comparisons. In *Proceedings of the Third European Conference on Computer Vision (Vol. 1)*, ECCV '94, pages 51–60, Secaucus, NJ, USA. Springer-Verlag New York, Inc.

[Oubel *et al.* (2012)] Oubel, E., De Craene, M., Hero, A. O., Pourmorteza, A., Huguet, M., Avegliano, G., Bijnens, B., and Frangi, A. F. (2012). Cardiac motion estimation by joint alignment of tagged MRI sequences. *Medical Image Analysis*, 16(1):339–350.

[Pei *et al.* (2001)] Pei, S.-C., Ding, J.-J., and Chang, J.-H. (2001). Efficient implementation of quaternion fourier transform, convolution, and correlation by 2-D complex FFT. *IEEE Transactions on Signal Processing*, 49(11):2783–2797.

[Petitjean *et al.* (2005)] Petitjean, C., Rougon, N., and Cluzel, P. (2005). Assessment of myocardial function: a review of quantification methods and results using tagged MRI. *Journal of Cardiovascular Magnetic Resonance*, 7(2):501–516.

[Prince and McVeigh (1992)] Prince, J. and McVeigh, E. (1992). Motion estimation from tagged MR image sequences. *IEEE Transactions on Medical Imaging*, 11(2):238–249.

[Qian *et al.* (2011)] Qian, Z., Liu, Q., Metaxas, D., and Axel, L. (2011). Identifying regional cardiac abnormalities from myocardial strains using nontracking-based strain estimation and spatio-temporal tensor analysis. *IEEE Transactions on Medical Imaging*, 30(12):2017–2029.

[Reddy and Talari (2011)] Reddy, V. and Talari, J. (2011). Color image registration and template matching using quaternion phase correlation. *Ubiquitous Computing and Communication*, 6(1):714–721.

[Ricco and Tomasi (2012)] Ricco, S. and Tomasi, C. (2012). Dense lagrangian motion estimation with occlusions. In *2012 IEEE Conference on Computer Vision and Pattern Recognition (CVPR)*, pages 1800–1807.

[Said *et al.* (2008)] Said, S., Le Bihan, N., and Sangwine, S. (2008). Fast complexified quaternion fourier transform. *IEEE Transactions on Signal Processing*, 56(4):1522–1531.

[Sangwine *et al.* (2001)] Sangwine, S., Eli, T., and Moxey, C. (2001). Vector phase correlation. *Electronics Letters*, 37(25):1513–1515.

[Sangwine and Ell (2000)] Sangwine, S. J. and Ell, T. A. (2000). Colour image filters based on hypercomplex convolution. *IEE Proceedings - Vision Image and Signal Processing*, 147(2):89–93.

[Sangwine and Le Bihan (2007)] Sangwine, S. J. and Le Bihan, N. (2007). Hypercomplex analytic signals: extension of the analytic signal concept to complex signals. In *Proceedings of the 15th European Signal Processing Conference*, pages 621–624, Poznan, Pologne.

[Schlaikjer *et al.* (2003)] Schlaikjer, M., Bagge, J., Sorensen, O., and Jensen, J. (2003). Trade off study on different envelope detectors for B-mode imaging. In *2003 IEEE Symposium on Symposium*, volume 2, pages 1938–1941.

[Sun *et al.* (2010)] Sun, D., Roth, S., and Black, M. J. (2010). Secrets of optical flow estimation and their principles. In *2010 IEEE Conference on Computer Vision and Pattern Recognition (CVPR)*, pages 2432–2439.

[Sun *et al.* (2011)] Sun, F.-r., Zhang, M.-q., Jia, X.-b., Wang, X.-j., Yao, G.-h., and Zhang, Y. (2011). Region of interest tracking in real-time myocardial contrast echocardiography. *Journal of Medical Systems*, 35(2):163–167.

[Sun *et al.* (2014)] Sun, D., Roth, S., and Black, M. (2014). A quantitative analysis of current practices in optical flow estimation and the principles behind them. *International Journal of Computer Vision*, 106(2):115–137.

[Sühling *et al.* (2005)] Sühling, M., Arigovindan, M., Jansen, C., Hunziker, P., and Unser, M. (2005). Myocardial motion analysis from B-mode echocardiograms. *IEEE Transactions on Image Processing*, 14(4):525–536.

[Traversoni (2006)] Traversoni, L. (2006). Movement detection and recognition with quaternion wavelets. In *International Conference on the Applications of Computer Science and Mathematics in Architecture and Civil Engineering*.

[Unser *et al.* (2009)] Unser, M., Sage, D., and Van De Ville, D. (2009). Multiresolution monogenic signal analysis using the Riesz-Laplace wavelet transform. *IEEE Transactions on Image Processing*, 18(11):2402–2418.

[Vince (2008)] Vince, J. A. (2008). *Geometric Algebra for Computer Graphics*. Springer-Verlag, Santa Clara, CA, USA, 1 edition.

[Wachinger *et al.* (2011)] Wachinger, C., Klein, T., and Navab, N. (2011). The 2D analytic signal on RF and B-mode ultrasound images. *Information processing in medical imaging: Lecture Notes in Computer Science*, 22:359–370.

[Wang *et al.* (2004)] Wang, W., Ishii, N., Miyamoto, Y., and Takeda, M. (2004). Pseudo-phase information of complex analytic signal of speckle fields and its applications: microdisplacement measurement based on phase-only correlation in signal domain. *Proceedings of SPIE*, 5457:44–49.

[Wang *et al.* (2012)a] Wang, L., Girard, P., Clarysse, P., and Delachartre, P. (2012a). Phase extraction of the analytic video signal in Clifford algebra. In *5th conference on Applied Geometric Algebras in Computer Science and Engineering*, La Rochelle, France.

[Wang *et al.* (2012)b] Wang, L., Girard, P. R., Bernard, A., Liu, Z., Clarysse, P., and Delachartre, P. (2012b). 3-D biquaternionic analytic signal and application to envelope detection in 3-D ultrasound imaging. In *IEEE International Conference on 3D Imaging (IC3D)*, pages 1–8, Liège, Belgium.

[Wang *et al.* (2012)c] Wang, L., Liu, Z., Girard, P., Clarysse, P., and Delachartre, P. (2012c). Extension of analytic signal conception on dynamic image sequences. In *9ème Manifestation des Jeunes Chercheurs en Sciences et Technologies de l'Information et de la Communication*, Lille, France.

[Witten and Shragge (2006)] Witten, B. and Shragge, J. (2006). Quaternion-based signal processing. In *Society of Exploration Geophysicists Annual Meeting*, New Orleans, Louisiana.

[Woo *et al.* (2009)] Woo, J., Hong, B., Hu, C., Shung, K. K., Kuo, C. J., and Slomka, P. J. (2009). Non-rigid ultrasound image registration based on intensity and local phase information. *Journal of Signal Processing Systems*, 54(1-3):33–43.

[Xavier *et al.* (2012)] Xavier, M., Lalande, A., Walker, P., Brunotte, F., and Legrand, L. (2012). An adapted optical flow algorithm for robust quantification of cardiac wall motion from standard Cine-MR examinations. *IEEE Transactions on Information Technology in Biomedicine*, 16(5):859–868.

[Zang *et al.* (2007)] Zang, D., Wietzke, L., Schmaltz, C., and Sommer, G. (2007). Dense optical flow estimation from the monogenic curvature tensor. In Sgallari, F., Murli, A., and Paragios, N., editors, *Scale Space and Variational Methods in Computer Vision*,

volume 4485 of *Lecture Notes in Computer Science*, pages 239–250. Springer Berlin Heidelberg.

[Zhang *et al.* (2006)] Zhang, W., Noble, J., and Brady, J. (2006). Real time 3-D ultrasound to MR cardiovascular image registration using a phase-based approach. In *3rd IEEE International Symposium on Biomedical Imaging: Nano to Macro, 2006.*, pages 666–669.

INSA INSTITUT NATIONAL DES SCIENCES APPLIQUÉES LYON

FOLIO ADMINISTRATIF

THÈSE SOUTENUE DEVANT L'INSTITUT NATIONAL DES SCIENCES APPLIQUÉES DE LYON

NOM : WANG DATE de SOUTENANCE : 19 Décembre 2014

Prénom : Liang

TITRE : Myocardial motion estimation from 2D analytical phases and preliminary study on the hypercomplex signal

NATURE : Doctorat Numéro d'ordre : 2014ISAL0140

Ecole doctorale : ÉLECTRONIQUE, ÉLECTROTECHNIQUE, AUTOMATIQUE (E.E.A)

Spécialité : Traitement du Signal et de l'Image

RESUME :

There are requirements for the processing of 2D/3D medical data for several applications such as motion estimation on 2D cardiac image sequence and 2D/3D envelope detection for ultrasound radio-frequency signal. Meanwhile, different mathematical tools, such as multidimensional analytic signals, provide possibilities to calculate multidimensional phases and modules. However, little work can be found on multidimensional analytic signals that perform appropriate extensibility for the applications on both of the 2D and 3D medical data processing. In this thesis, based on the Hahn 1D complex analytic, we aim to proposed a multidimensional extension approach from the 2D to a new 3D hypercomplex analytic signal in the framework of Clifford algebra. With the complex/hypercomplex analytic signals, we propose new 2D/3D medical image processing methods for the application of ultrasound envelope detection and cardiac motion estimation.

Firstly, a general representation of 2D quaternion signal is proposed in the framework of Clifford algebra and this idea is extended to generate 3D hypercomplex analytic signal. This 3D hypercomplex analytic signal is called 3D Clifford analytic signal. The proposed method describes that the complex/hypercomplex 2D analytic signals, together with 3D hypercomplex analytic signal, are equal to different combinations of the original signal and its partial and total Hilbert transforms, which means that the hypercomplex Clifford analytic signal can be calculated by the classical Fourier transform. Therefore, this method offers the numerical implementation with a low computational complexity. Based on the proposed 3D Clifford analytic signal, an application of 3D ultrasound envelope detection is presented. The results show a contrast optimization of about 7% comparing with 1D and 2D envelope detection methods.

Secondly, this thesis proposes an approach based on two spatial phases of the 2D analytic signal applied to cardiac sequences. By combining the information of these phases issued from analytic signals of two successive frames, we propose an analytical estimator for 2D local displacements. To improve the accuracy of the motion estimation, a local bilinear deformation model is used within an iterative estimation scheme. This phase-based method allows the displacement to be estimated with subpixel accuracy and is robust to image intensity variation in time. Results from seven realistic simulated tagged magnetic resonance imaging (MRI) sequences show that our method is more accurate compared with the state-of-the-art method using the phase of monogenic signal or the classical method using the optical flow equation. The motion estimation errors (end point error) of the proposed method are reduced by about 33% compared with that of the tested methods. In addition, the frame-to-frame displacements are further accumulated in time, to allow for the calculation of myocardial point trajectories. Indeed, from the estimated trajectories in time on two patients with infarcts, the shape of the trajectories of myocardial points belonging to pathological regions are clearly reduced in magnitude compared with the ones from normal regions. Myocardial point trajectories, estimated from our phase-based analytic signal approach, are therefore a good indicator of the local cardiac dynamics. Moreover, they are shown to be coherent with the estimated deformation of the myocardium.

MOTS-CLÉS :
Phase image, Complex/hypercomplex analytic signal, 3D Clifford analytic signal, Myocardial motion estimation, 3D ultrasound envelope detection

Laboratoire (s) de recherche : Centre de Recherche en Acquisition et Traitement de l'Image pour la Santé (CREATIS)

Directeur de thèse: Philippe DELACHARTRE

Président de jury : Philippe CARRÉ

Composition du jury : Philippe DELACHARTRE (Directeur de thèse), Patrick R. GIRARD (Co-encadrant de thèse), Patrick CLARYSSE (Co-encadrant de thèse), Stephen J. SANGWINE (Rapporteur), Laurent SARRY (Rapporteur), Philippe CARRÉ (Examinateur), Mireille GARREAU (Examinateur)